High Mobility Organic Semiconductors For Microelectronic Applications

Ioulianna Panidi

A thesis submitted in partial fulfilment of the degree of Doctor of Philosophy

Imperial College London

Department of Physics

September 2019

Declaration

This thesis outlines the work as carried out between October 2016 and September 2019 in the Experimental Solid State (EXSS) Physics group at Imperial College London, under the supervision of Prof. Thomas D. Anthopoulos This work was funded by the Centre for Doctoral Training in Plastic Electronics and Merck Chemical Ltd. (EP/L016702/1). The materials presented in this thesis is my own work, unless it is stated otherwise. The work outlined in this thesis has not been submitted prior to this for any other degree at any other University.

The copyright of this thesis rests with the author and is made available under a Creative Commons Attribution Non-Commercial No Derivatives licence. Researchers are free to copy, distribute or transmit the thesis on the condition that they attribute it, that they do not use it for commercial purposes and that they do not alter, transform or build upon it. For any reuse or redistribution, researchers must make clear to others the licence terms of this work.

Supervisors:

Prof. Thomas D. Anthopoulos, Department of Physics, Imperial College London, U.K. & Division of Physical Sciences and Engineering KAUST, Saudi Arabia.

Prof. Martin Heeney, Department of Chemistry, Imperial College London, U.K.

Dr. David Sparrowe, Merck KGaA, Southampton, U.K.

Internal Examiner:

Dr. David J. Payne, Department of Materials, Imperial College London, U.K.

External Examiner:

Prof. Peter Skabara, School of Chemistry, University of Glasgow, U.K.

Julianna Panidi

September 2019

Abstract

The potential of organic electronic devices, over the past few years, has been proven tremendous. Flexible and transparent electronic devices will soon enter the market, but there are still some challenging aspects requiring further improvements. A generic approach to enhance the charge transport properties of the organic semiconductors is by introducing molecular additives. In particular for thin film transistors, doping the semiconductor layer leads to higher charge carrier mobility, as well as improving several parameters of the device. The work in this thesis focuses on identifying suitable molecular additives that can dope organic semiconductors for thin film transistors.

Chapter 5 presents the application of tris(pentafluorophenyl)borane $B(C_6F_5)_3$ as an effective p-type dopant. $B(C_6F_5)_3$ was applied in several small molecule:polymer blends and the improvement in the charge transport properties, as measured from organic thin film transistors (OTFTs), was remarkable. In particular the blend diF-TESADT:PTAA and the C_8-BTBT:C_{16}-IDT-BT showed hole mobility of 8 and 11 cm^2/Vs, respectively. OTFT parameters, such as the threshold voltage and the contact resistance were significantly reduced with the addition of molecular additives. The impact of the dopant addition in the blends was studied by AFM and XRD, which revealed that long-range crystallinity was induced in certain systems.

Chapter 6 presents the DMBI-BDZC as a new n-type dopant. For transistors integration into circuits balanced charge transport is required and thus extensive optimisation is still required for n-type materials. DMBI-BDZC was used to dope a small molecule (NDI3HU-DTYM2) and a polymeric (N2200) semiconductor. In both systems free electron

generation was observed at an optimum dopant concentration, as measured by electron paramagnetic resonance (EPR). OTFTs with enhanced charge carrier mobility and reduced contact resistance was achieved with the dopant addition. By further analysis of the device characteristics, reduction in both activation energy and density of traps states was observed in the doped devices. The morphology studies of the organic semiconducting thin films revealed that the dopant addition is not disrupting the structure. Furthermore, the reduction in activation energy at low voltages is in accordance with the trap density calculations as performed from the OTFTs.

In chapter 7 a single organic layer light emitting transistor (OLET) is demonstrated. The key behind this device structure was the identification of the polymer PDITTT. This polymer combines high charge transport properties (1 cm^2/Vs) as well as having green light emission. The properties of the polymer allowed the fabrication of a single layer organic semiconducting OLET. Blending the polymer with the small molecule C_8-BTBT resulted in enhanced charge transport OTFTs. OTFTs and OLETs were fabricated from both the PDITTT and C_8-BTBT:PDITTT.

Acknowledgements

Above all I would like thank my supervisor Professor Thomas Anthopoulos for giving me the opportunity to join his research group. I am grateful for his guidance and support all these years. I would also like to thank my second supervisor, Professor Martin Heeney for his advice and giving me the opportunity to test new materials. Lastly, I want to thank Merck Ltd for sponsoring my PhD and especially Dr. David Sparrowe.

I also very great grateful to all the AMD group members for their help all these years. In particular, I would like to thank Dr. Alexandra Paterson for introducing me into the organic semiconductor blends world and for continuing our collaboration. Special thanks to Dr. Hendrik Faber and Dr. Yen-Hung Lin for his assistance with all the lab equipments and data analysis.

I would like to thank also Dr. Satyajit Das, Dr. Wentao Huang and Dr. Flurin Eisner for being always there when I needed them. Also my best friend Dr. Dimitra Georgiadou for answering all my scientific and non-scientific questions.

It has been a wonderful journey and without the support from Carolyn, Juraci, Steve and Professor Jenny Nelson it wouldn't have been possible. I am very grateful also to Dr. Daniel Balint for his support and understanding the difficulty of being a subwarden while working towards your PhD.

Contents

Abstract **2**

Acknowledgements **4**

List of Figures **13**

List of Tables **14**

List of Publications **15**

1 Introduction **17**
1.1 Background 18
1.2 Motivation 20
1.3 Thesis Outline 21

2 Charge transport in OSCs **23**
2.1 Electronic properties of organic semiconductors 24
2.1.1 Molecular Orbitals 24
2.2 Charge transport models 25
2.2.1 Variable range hopping 25
2.2.2 Multiple trapping and release Meyer-Nelson model 26
2.3 Organic semiconducting materials 27
2.3.1 Polymeric semiconductors 28
2.3.2 Small molecule semiconductors 29
2.3.3 Organic semiconducting blends 30
2.4 Thin film transistor (TFT) model 31
2.4.1 TFT architectures 31
2.4.2 Operation principles 32
2.4.3 Parameter extraction 34
2.4.4 Semiconductor - Dielectric interface 36
2.4.5 Metal - Semiconductor interface 37
2.5 Organic light emitting transistors (OLETs) 39
2.6 Summary 40

3 Molecular Doping **42**
3.1 Introduction 43
3.2 Doping mechanism 43
3.2.1 Ground state integer charge transfer 43
3.2.2 Hybrid charge transfer complex 44
3.3 Doped organic semiconductors 45
3.3.1 Doping methods 45
3.3.2 Charge carrier mobility 46
3.3.3 Threshold voltage and contact resistance 47
3.4 Summary 48

4 Experimental Methods **49**

4.1 Device fabrication . . . 50
4.1.1 Substrate preparation . . . 50
4.1.2 Contacts deposition . . . 50
4.1.3 Contact workfunction modification . . . 50
4.1.4 Solution processing: p-type doping of OSCs . . . 51
4.1.5 Solution processing: n-type doping of OSCs . . . 52
4.1.6 Solution processing: OLETs . . . 53
4.1.7 Organic thin film deposition . . . 53
4.2 Electrical Characterisation . . . 54
4.2.1 Current - voltage measurements . . . 54
4.2.2 Low - temperature measurements . . . 55
4.2.3 Brightness measurements . . . 55
4.2.4 External Quantum Efficiency . . . 56
4.3 Thin film characterisation . . . 57
4.3.1 Polarised optical microscopy . . . 57
4.3.2 Atomic Force Microscopy . . . 58
4.3.3 X-Ray Diffraction . . . 59
4.3.4 Kelvin Probe & Air Photoemission Spectroscopy . . . 60
4.3.5 Electron Paramagnetic Resonance . . . 61
4.4 Optical properties of thin films and devices . . . 61
4.4.1 Ultraviolet-visible-near infrared absorption spectroscopy (UV-Vis-NIR) . . . 61
4.4.2 Electroluminescence and Photoluminescence . . . 61
4.4.3 Steady state and time-resolved PL & solid-state photoluminescence quantum efficiency (PLQE) . . . 62
4.5 Summary . . . 62

5 P-type Doping OTFTs **63**
5.1 Introduction . . . 64
5.2 Organic Semiconducting Blends . . . 64
5.3 Doping Mechanism . . . 65
5.4 p-Type Thin Film Transistors . . . 66
5.4.1 Organic Semiconductor Blends . . . 66
5.4.2 Single component TFTs . . . 71
5.5 Thin film morphology . . . 73
5.5.1 POM and AFM imaging . . . 73
5.5.2 XRD Analysis . . . 77
5.5.3 Energy levels . . . 79
5.6 Summary . . . 80

6 N-type Doping OTFTs **82**
6.1 Introduction . . . 83
6.2 Organic semiconducting materials . . . 83
6.3 Electron Paramagnetic Resonance Measurements . . . 84
6.4 Electrical Characterisation . . . 86
6.4.1 N-type OTFTs . . . 86
6.4.2 Low temperature measurements . . . 89
6.4.3 Trap density . . . 92
6.5 Morphology Characterisation . . . 93
6.5.1 AFM Characterisation . . . 94
6.5.2 X-Ray Diffraction Characterisation . . . 95
6.6 Summary . . . 97

7 Organic Light Emitting Transistors **98**
7.1 Introduction 99
7.2 Organic semiconducting materials 100
7.2.1 Optical properties 100
7.2.2 Thin film morphology 103
7.3 Organic semiconducting devices 105
7.3.1 OTFTs 105
7.3.2 OLETs 106
7.3.3 Device Characterisation 108
7.4 Summary 110

8 Conclusion & Future Work **111**
Bibliography 128

9 Appendix **129**

List of Figures

1.1 Organic electronic devices: (a) a flexible OLED TV from LG, (b) flexible displays for the automotive industry from Flexenable and (c) wearable sensor based on organic electronics from Berkeley. [20-22] 19

1.2 Number of IoT connected devices worldwide from 2015 to 2025. [23] . . 19

2.1 a) Formation of sp^2 hybridisation of carbon and b) schematic of atomic orbitals after the hybridisation. 24

2.2 Density of states (DOS) of an organic semiconductor as suggested by the multiple traps and release model. 26

2.3 Charge carrier mobility in saturation regime for p and n-type organic semiconductor over 30 years. [34] 28

2.4 Molecular structures of a few conjugated polymers often used for organic electronics applications. 29

2.5 Molecular structures of a few small molecules used for OTFT applications. 29

2.6 Schematic representation of the vertical phase separation mechanism that is observed in the small molecule:polymer blends. Initially both the polymer and the small molecule are distributed in the solution; after spin coating or thermal annealing the solvent evaporates and a final thin film is produced, where the small molecule is on the top and the polymer underneath. 31

2.7 Thin film transistor architectures for (a) bottom-gate bottom-contact (BG-BC), (b) top-gate bottom-contact (TG-BC), (c) bottom-gate top-contact (BG-TC) and (d) top-gate top-contact (TG-TC). 32

2.8 Thin film transistor architecture in bottom gate (G) bottom contact (S,D) configuration. (a) A uniform channel is formed when a small V_D is applied (linear regime). (b) By increasing the V_D, the channel starts to pinch-off and the resistance is increased. (c) At higher V_D application the channel is pinched-off close to the drain. 33

2.9 Transfer characteristic of a thin film transistor in both linear and saturation regime. The square root of the drain current in the saturation regime is also plotted (right axis). By a linear fitting of the $I^{0.5}$ the threshold voltage and the slope can be extracted. 35

2.10 Metal – organic semiconductor interface band structure for electron injection from the LUMO (a) at the Mott Schottky barrier limit and (b) at the presence of an interface dipole. 38
2.11 OLET device architecture when using (a) an ambipolar OSC, (b) a bilayer of OSCs, (c) a bulk heterojunction and (d) a unipolar device. . . 39

3.1 Integer charge transfer mechanism for (a) a p-type OSC system, where electrons are transferred from the HOMO of the OSC to the LUMO of the dopant and (b) for a n-type OSC system, where electrons are transferred from the HOMO of the dopant to the LUMO of the OSC. . 44
3.2 Charge transfer complex formation for a p-type OSC and a dopant system. 44
3.3 OTFTs in a BG-TC configuration showing the different doping methods for (a) contact doping, (b) doping layer and (c) bulk doping. 46
3.4 Energy level diagram showing the shift of the Fermi energy (E_F) level towards the HOMO level of a p-type organic semiconductor upon doping, where E_T is the transport energy level, E_A is the activation energy and E_v is the an effective valence band energy. 47

4.1 Steps of the spin coating technique: (a) Solution (blue) is dropped onto the substrate. (b) Spin of the substrate spreads the solution and excess is spun off due to centrifugal forces while solvent is evaporating. (c) The thin film is produced. 54
4.2 Experimental set-up of the low temperature system used to measure TFTs with a cryogenic probe station. 55
4.3 Experimental set up of the spectrometer used to determine the evolution of the brightness of the OLETs. The photomultiplier tube converts the light detected by the photodetector. 56
4.4 Schematic configuration of a polarised light microscope. 58
4.5 Cartoon schematic of the AFM system. A laser beam is irradiating the tip and the photodiode detects the signal which then via the feedback loop and the piezoelectric tube (PZT) converts the signal to image. The sample in this figure is an n-type organic small molecule in 3D which it was used in this work. 59
4.6 Schematic representation of Bragg's law. 60

5.1 (a) Chemical structures of diF-TESADT, PTAA and $B(C_6F_5)_3$. (b) LUMO and HOMO energies for $B(C_6F_5)_3$ calculated via the DFT method. The HOMO is predicted to be localised on phenyl groups whilst the LUMO is delocalised over the whole molecule. (c) HOMO and LUMO energies of diF-TESADT, PTAA and $B(C_6F_5)_3$. 65

5.2 Bottom-contact top-gate (BC-TG) thin film transistor a) device architecture and b) array of fabricated OTFTs on a glass substrate. 66
5.3 Transfer characteristics as measured for top-gate, bottom-contact diF-TESADT:PTAA transistors with different $B(C_6F_5)_3$ concentrations in the range of 0-3.6 mol%. 67
5.4 Output characteristics (I_D vs V_D) for the organic semiconducting blend (a) diF-TESADT:PTAA and (b) diF-TESADT:PTAA:$B(C_6F_5)_3$ (2.4 mol%) 67
5.5 (a) Evolution of hole mobility (μ_h) as a function of $B(C_6F_5)_3$ concentration for the diF-TESADT:PTAA: $B(C_6F_5)_3$ blend. (b) & (c) display the evolution of threshold voltage (V_{Th}) and current on-off ratio, respectively, as a function of $B(C_6F_5)_3$ concentration and (d) evolution of contact resistance (R_C) versus V_G calculated for the pristine and $B(C_6F_5)_3$ (2.4 mol%)-doped diF-TESADT:PTAA OTFTs. 68
5.6 (a, b) Chemical structures of the additional organic semiconducting materials used for blends and (c) their HOMO energy level, as measured by APS. 69
5.7 Transfer characteristics measured for top-gate, bottom-contact (a) C_8-BTBT:C_{16}IDT-BT and (b) TIPS-pen:PTAA blends. 70
5.8 Histograms of saturation mobility for (a) pristine C_8-BTBT:C_{16}IDT-BT:$B(C_6F_5)_3$ (0 mol%) and doped C_8-BTBT:C_{16}IDT-BT:$B(C_6F_5)_3$ (0.05 mol%) and (b) pristine TIPS-pen:PTAA: $B(C_6F_5)_3$(0 mol%) and doped TIPS-pen:PTAA: $B(C_6F_5)_3$ (2.4 mol%). 70
5.9 Transfer characteristics for the small molecule OTFTs with (a) diF-TESADT:$B(C_6F_5)_3$ 0 mol% & 2.4 mol%, (b) TIPS-pen:$B(C_6F_5)_3$ 0 mol% & 0.5 mol% and (c) C_8-BTBT:$B(C_6F_5)_3$ 0 mol% & 0.1 mol%. 71
5.10 Transfer characteristics for the polymer OTFTs with (a) PTAA: $B(C_6F_5)_3$ 0 mol% & 0.1 mol% and (b) C_{16}IDT-BT: $B(C_6F_5)_3$0 mol% & 0.1 mol%. 72
5.11 Polarised optical microscopy images of diF-TESADT:PTAA (a) a pristine (0 mol%) and (b) $B(C_6F_5)_3$-doped (2.4 mol%) blend layer. Topographical AFM images of diF-TESADT:PTAA (a) a pristine (0 mol%) and (b) $B(C_6F_5)_3$-doped (2.4 mol%) blend layer and (e) their corresponding height histograms. (f) Cartoons representing schematics of the layer cross-section of the pristine and $B(C_6F_5)_3$-doped diF-TESADT:PTAA layers. 74
5.12 (a) AFM topography image for diF-TESADT:PTAA:$B(C_6F_5)_3$- doped layer and (b) high resolution AFM image of region A (box) highlighted in (a). (c) Line scans 1 and 2 obtained from the AFM image in (b). . . 75

5.13 POM images for (a) C_8-BTBT:C_{16}IDT-BT & (b) C_8-BTBT:C_{16}IDT-BT:$B(C_6F_5)_3$ (0.05 mol%). Topographical images for (c) pristine C_8-BTBT:C_{16}IDT-BT, (d) doped C_8-BTBT:C_{16}IDT-BT: $B(C_6F_5)_3$ (0.05 mol%) and (e) their corresponding height distribution histograms. . . . 75

5.14 POM images for (a) TIPS-pen:PTAA & (b) TIPS-pen:PTAA:$B(C_6F_5)_3$ (2.4 mol%). Topographical images for (c) pristine TIPS-pen:PTAA, (d) doped TIPS-pen:PTAA:$B(C_6F_5)_3$ (2.4 mol%) and (e) their corresponding height distribution histograms. 76

5.15 XRD diffractograms for diF-TESADT, diF-TESADT:PTAA and diF-TESADT:PTAA:$B(C_6F_5)_3$ (2.4 mol%) thin films. 77

5.16 X-ray diffractograms around the (001) peak and the corresponding Voigt fits for the diF-TESADT, diF-TESADT:$B(C_6F_5)_3$, diF-TESADT:PTAA, and the diF-TESADT: PTAA:$B(C_6F_5)_3$ (2.4 mol%) films. 79

5.17 Workfunction (ϕ) and HOMO energy levels for the (a) diF-TESADT:PTAA, (b) C_8-BTBT:C_{16}IDT-BT and (c) TIPS-pen:PTAA blends by varying the $B(C_6F_5)_3$ concentration. 80

6.1 Molecular structures of n-type organic semiconductors and their energy levels as predicted by DFT calculations (a) for the molecular dopant DMBI-BDZC, (b) the polymer N2200 and (c) the small molecule NDI3HU-DTYM2. 84

6.2 Energy levels as predicted by DFT calculations (a) for the molecular dopant DMBI-BDZC, (b) the polymer N2200 and (c) the small molecule NDI3HU-DTYM2. 84

6.3 EPR measurements (a&c) and doping mechanism (b&d) for the n-type doped layers with DMBI-BDZC for the (a&b) N2200 and (c&d) NDI3HU-DTYM2. 85

6.4 Transfer characteristics (a&c) of the (a) N2200:DMBI-BDZC TFTs and (b) NDI3HU-DTYM2:DMBI-BDZC with their corresponding square root of the I_D vs V_G plots (b&d). The output curves (e&f) for the N2200:DMBI-BDZC (e) (0-1 mol%) and NDI3HU-DTYM2:DMBI-BDZC (f) (0-2 mol%). 87

6.5 Electron charge carrier mobility, threshold voltage and on/off current ratio evolution for (a) N2200:DMBI-BDZC (0-1 mol%) and (b) NDI3HU-DTYM2 (0-2 mol%) OTFTs. (c) Contact resistance for pristine (0 mol%) and DMBI-BDZC doped OTFTs as calculated via the TLM method. 88

6.6 Temperature dependent charge transport measurements performed in the range 78-310 K. Transfer characteristics of (a) pristine & (b) 0.2 mol% DMBI-BDZC-doped N2200 OTFTs, with channel width 1000 μm and length 40 μm. Transfer characteristics of (c) pristine & (d) 0.5 mol% DMBI-BDZC-doped NDI3HU-DTYM2 OTFTs, with channel width and length of 1000 and 30 μm, respectively. 90

6.7 Arrhenius plots of N2200:DMBI-BDZC OTFTs with channel width 1000 μm and length 40 μm for (a) 0 mol% & (b) 0.2 mol% and NDI3HU-DTYM2:DMBI-BDZC with channel width 1000 μm and length 30 μm for (c) 0 mol% and (d) 0.5 mol%, as extracted from OTFTs when measured by applying V_D= 10 V. Activation energy E_A as function of V_G, as extracted from (a-d) for (e) N2200:DMBI-BDZC and (f) NDI3HU-DTYM2:DMBI-BDZC OTFTs. 91

6.8 Relative trap density (ΔN_{tr}) and trap concentration (ΔD_{tr}) for the (a) N200:DMBI-BDZC and (b) NDI3HU-DTYM2:DMBI-BDZC OTFTs as calculated from the transfer curves. 92

6.9 POM images of NDI3HU-DTYM2:DMBI-BDZC 0-2 mol% thin films. . 93

6.10 AFM morphology analysis for N2200:DMBI-BDZC (0-1 mol%) (a) Topography AFM scans of thin films, (b) their corresponding height histogram and (c) the surface roughness (RMS) as a function of DMBI-BDZC mol%, as extracted from the topography scans. 94

6.11 AFM morphology analysis for NDI3HU-DTYM2:DMBI-BDZC (0-2 mol%). (a) Topography AFM scans of thin films and (b) their corresponding height histogram. 95

6.12 X-Ray diffraction patterns for pristine and DMBI-BDZC doped (a) N2200 and (b) NDI3HU-DTYM2 thin films. 96

7.1 Chemical structures of (a) PDITTTT & (b) C_8-BTBT and (c) their HOMO energy level. 100

7.2 Normalised absorption spectra and photoluminescence (PL) for (a) PDITTTT polymer and (b) C_8-BTBT: PDITTTT blend films. The solid lines (left ordinate) are absorption and the dashed lines (right ordinate) PL, with black for as spin-coated and blue for post-annealing. 101

7.3 PLQE and absorption of the thin films by varying the concentration of the polymer PDITTTT in the small molecule:polymer blend. 102

7.4 Normalised time-resolved PL (537 nm, pumped at 405 nm) for PDITTTT polymer (a) as-spun and (b) annealed and for the C_8-BTBT: PDITTTT blend films (c) as-spun and (d) annealed. 102

7.5 AFM topography images for (a) PDITTTT and (b) C_8-BTBT: PDITTTT. (c) Their height distribution as extracted from (a) & (b). 103
7.6 X-Ray diffraction pattern for C_8-BTBT, PDITTTT and the C_8-BTBT: PDITTTT blend. Peak position of C_8-BTBT according to previously reported values. [151] 104
7.7 Device structure for bottom-contact top-gate (BC-TG) OTFTs for the (a) polymer PDITTTT and (b) C_8-BTBT:PDITTTT blend devices. . . 105
7.8 Transfer (a&c) and output (b&d) curves for (a&b) PDITTTT and (c&d) C_8-BTBT:PDITTTT BC-TG OTFTs. 106
7.9 Device structure for bottom-contact top-gate (BC-TG) OLETs for the (a) polymer PDITTTT and (b) C_8-BTBT:PDITTTT blend devices. . . 106
7.10 Transfer (a&c) and output (b&d) curves for (a&b) PDITTTT and (c&d) C_8-BTBT:PDITTTT BC-TG OLETs. 107
7.11 Luminance and EQE voltage dependence for the PDITTTT (polymer) and C_8-BTBT:PDITTTT (blend) OLET devices. Both top (black) and bottom (red) emission is showed. 108
7.12 Photoluminescence and electroluminescence spectra for (a) PDITTTT and (b) C_8-BTBT:PDITTTT thin films, along with the microscope images of their emission zone (scale bar: 250 μm) 109
7.13 OLET (a) structure and (b) charge transfer mechanism. 110

List of Tables

4.1 Solution preparation for single compound p-type organic semiconductor solutions for TFTs which shows the concentration, the solvent (cb: chlorobenzene, tol: toluene), the solution heating temperature, the dopant concentration and the thin film annealing temperature in bracket. . . . 52

4.2 Solution preparation for blend organic semiconductors, which shows the total concentration of the blend (the mixing ratio), the solvents (Cb is the chlorobenzene and Tet is the 1,2,3,4 tetrahydronapthalene), the solution heating temperature, the dopant concentration and the thin film annealing temperature in bracket. 52

4.3 Solution preparation for n-type doping of organic semiconductors, which shows the concentration of the solution, the solvent, the solution heating temperature, the dopant concentration and the thin film annealing temperature. 53

4.4 Preparation for single compound p-type organic semiconductor solutions for TFTs, showing the concentration, the solvent (cb: chlorobenzene, tol: toluene), the solution heating temperature, the dopant concentration and the thin film annealing temperature in brackets. 53

5.1 Hole charge carrier mobility of pristine organic semiconducting blend systems as measured in this project. 64

5.2 The Bragg angles (θ) of the three stronger peaks of the films and the corresponding d001 values. 78

5.3 The vertical grain size (G_z) and the microstrain (ϵs) as determined from the three stronger peaks of the films. G_z is an indicator of the vertical crystallinity, whereas ϵs is an indicator of the lateral crystallinity. . . . 79

7.1 Decay time as extracted by fitting the experimental data of the time-resolved PL for the PDITTTT and C_8-BTBT: PDITTTT films before and after annealing (120°C). 103

List of Publications

1. A. F. Paterson, R. Li, A. Markina, L. Tsetseris, S. MacPhee, H. Faber, A. Hamid Emwas, **J. Panidi**, H. Bristow, D. Andriyenko, M. Heeney, I. McCulloch, T. D. Anthopoulos, *N-type doping of the organic non-fullerene acceptor O-IDTBR leads to transistors with electron mobility in excess of 1 $cm^2V^{-1}s^{-1}$, submitted.*

2. M. U. Chaudhry, **J. Panidi**, A. Smith, J. Lim, K. Tezner, P. A. Patsalas, G. Vourlias, W. Y. Sit, Y. Firdaus, M. H. Heeney, D.D. C. Bradley, T. D. Anthopoulos, *Polymer light-emitting transistors with charge carrier mobility exceeding $1cm^2/Vs$*, **Adv. Electron. Mater. 2019, 1901132**.

3. Y.-H. Lin, W. Huang, P. Pattanasattayavong, R. Li, N. Sakai, J. Lim, M. J. Hong, **J. Panidi**, M. Heeney, J. G. Labram, T. D. Anthopoulos, H. J. Snaith, *Deciphering photocarrier dynamics for tuneable, high-performance perovskite heterojunction phototransistors*, **Nat. Commun. 2019, 10, 4475**.

4. S. Raya, **J. Panidi**, T. Mukhopadhyaya, U. Salznerd, T. D. Anthopoulos, S. Patila, *Electrochemical stability and ambipolar charge transport in diketopyrrolopyrrole -based organic materials*, **ACS Appl. Electron. Mater. 10, 2037-2046, 2019**.

5. H. Bristow, K. J. Thorley, A. J. P. White, A. Wadsworth, M. Babics, Z. Hamid, W. Zhang, A. F. Paterson, J. Kosco, **J. Panidi**, T. D. Anthopoulos, I. McCulloch, *Impact of non-fullerene acceptor side chain variation on transistor mobility*, **Adv. Electron. Mater. 2019, 1900344**

6. J. C Costa, A. Pouryazdan, **J Panidi**, F. Spina, T. D. Anthopoulos, M. O. Liedke, C. Schneider, A. Wagner, N. Münzenrieder, *Flexible IGZO TFTs and their suitability for space applications*, **IEEE J. Elect. Dev. Soc. 2019, 2931614**.

7. **J. Panidi**, J. Kainth, A. F. Paterson, S.Wang, L. Tsetseris, M.A. McLachlan, M.Heeney, T.D. Anthopoulos, *Introducing a nonvolatile n-type dopant drastically improves electron transport in polymer and small-molecule organic transistors* **Adv. Funct. Mater. 2019, 29, 1902784**.

8. H. H. Choi, A. F. Paterson, M. Fusella, **J. Panidi**, K. Cho, O. Solomeshch, N. Tessler, M.Heeney, T. D. Anthopoulos, B. Rand, and V. Podzorov, *Hall effect in polycrystalline organic semiconductors: the effect of grain boundaries*, **Adv. Funct. Mater. 2019, 1903617**.

9. Q. He, M. Shahid, **J. Panidi**, A. V. Marsh, W. Huang, Z. Fei, T. D. Anthopoulos, M. Heeney, *A versatile star-shaped organic semiconductor based on benzodithiophene and diketopyrrolopyrrole*, **J. Mater. Chem. C, 2019, 7, 6622**.

10. A.F. Paterson, L.Tsetseris, R. Li, A.l-H. Emwas, H. Faber, **J. Panidi**, Z. Fei, M. Heeney, T. D. Anthopoulos, *Addition of the Lewis Acid $Zn(C_6F_5)_2$ Enables Organic Transistors with a Maximum Hole Mobility in Excess of 20 cm^2 V^{-1} s^{-1}* **Adv. Mater. 2019, 31, 1900871**.

11. J. C. Costa, A. Pouryazdan, **J. Panidi**, T. Anthopoulos, M. O. Liedke, C. Schneider, A. Wagner, N. Munzenrieder, *Low temperature and radiation stability of flexible IGZO TFTs and their suitability for space applications*, **IEEE ESSDERC 2018, 98-101**.

12. Creamer, C.r S. Wood, P. D. Howes, A. Casey, S. Cong, A. V. Marsh, R. Godin, **J. Panidi**, Thomas D. Anthopoulos, C.H. Burgess, T. Wu, Z. Fei, Iain Hamilton, Martyn A. McLachlan, Molly M. Stevens, Martin Henney, *Post-polymerisation functionalisation of conjugated polymer backbones and its application in multifunctional emissive nanoparticles*, **Nat. Commun. 2018, 9, 3237**.

13. H. H. Choi, Y. I. Rodionov, A. F. Paterson, **J. Panidi**, D. Saranin, N. Kharlamov, S. I. Didenko, T. D. Anthopoulos, K. Cho, V. Podzorov, *Accurate Extraction of Charge Carrier Mobility in 4-Probe Field-Effect Transistors* **Adv. Funct. Mater. 2018, 1707105**.

14. **J. Panidi**, A. F. Paterson, D. Khim, Z. Fei, Y. Han, L. Tsetseris, G. Vourlias, P. A. Patsalas, M. Heeney, T. D. Anthopoulos, *Remarkable enhancement of the hole mobility in several organic small-molecules, polymers, and small-molecule:polymer blend transistors by simple admixing of the lewis acid p-dopant $B(C_6F_5)_3$*, **Adv. Sci. 2018, 5, 1700290**.

Chapter 1

Introduction



A brief overview of thin film transistors' history, since their discovery to the commercialy available electronic devices with organic semiconductors is given in this section. (Left panel: Iphone XS with an OLED display and an Apple A12 Bionic system on chip.) [1]

1.1 Background

It has been over 80 years since the first patent was filed, describing the concept of a transistor device, by Julius Lilienfeld. [2–4] A few years later in 1947, the first transistor from germanium was reported by John Bardeen, Walter Brattain and William Shockley at Bell Laboratories. [5, 6] For this ground breaking research they were awarded with the Nobel Prize in Physics in 1956. [7] It was only a few years later, in 1954, when germanium was replaced by silicon, fabricated from silicon single crystals, as it was reported from Bell Laboratories. Silicon transistors were easier to fabricate than the germanium, and that was the beginning of the Silicon Age. Rapid development then followed, which lead to the first transistor based computer in 1953, which was built at the University of Manchester. [8]

The first thin film transistor (TFT) was reported in 1962, by K. Weimer, of which active layers were deposited by thermal evaporation. [9] Several structures for thin film transistors were then discovered, and at around 1973 the first active-matrix liquid-crystal display (LCD) by incorporating cadmium selenide TFTs was reported. [10] A milestone for this field arose from the development of amorphous silicon (a-Si) transistors. [11] A few years later, in 1980, the first full-colour LCD based on a-Si TFTs was produced by Hotta et. al. [12]

Since then several semiconducting materials, including inorganics and organics, and various TFT device architectures were reported in the literature. [13, 14] The first organic TFT was reported by Koezuka et al. from thiophene molecules with charge carrier mobility of 2 x 10^{-5} cm^2/Vs. [15] This finding lead to an increased interest by the academic community and industry, where chemists are still developing organic semiconductors with enhanced charge transport properties. Other material categories have been incorporated in TFTs, including fullerene, graphene and metal oxides. [13, 16, 17]

The miniaturisation of transistor devices, along with their increased performance, led to electronics devices with smaller dimensions, as we use them today in our everyday life. Transistors are the building block of computers and it was predicted by Gordon Moore in 1965, that the number of transistors in an integrated circuit double every year; this is known as the Moore's law. [17, 18] The end of Moore's law is approaching, as for instance Apple in October 2018 announced the new iPhone generation, iPhone X, which has the Apple A12 Bionic system on a chip. [19] This chip has 6.9 billion transistors, an increase of 60% over the A11 technology, which was only realised a year ago.

Over the past few years significant interest from industry and academia has been focused on the development of new organic materials. The progress of organic semiconductors is incredible with applications including flexible screens, automotive displays

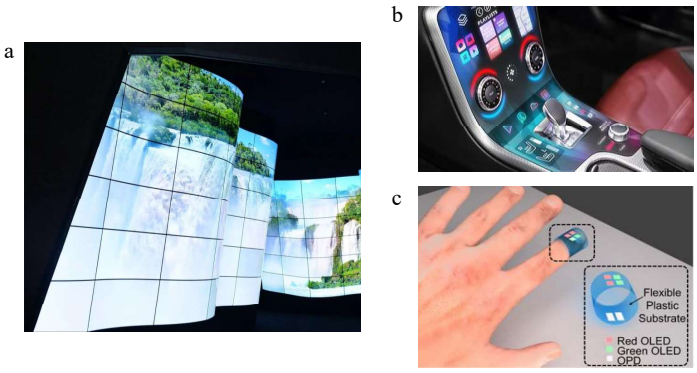


Figure 1.1: Organic electronic devices: (a) a flexible OLED TV from LG, (b) flexible displays for the automotive industry from Flexenable and (c) wearable sensor based on organic electronics from Berkeley. [20-22]

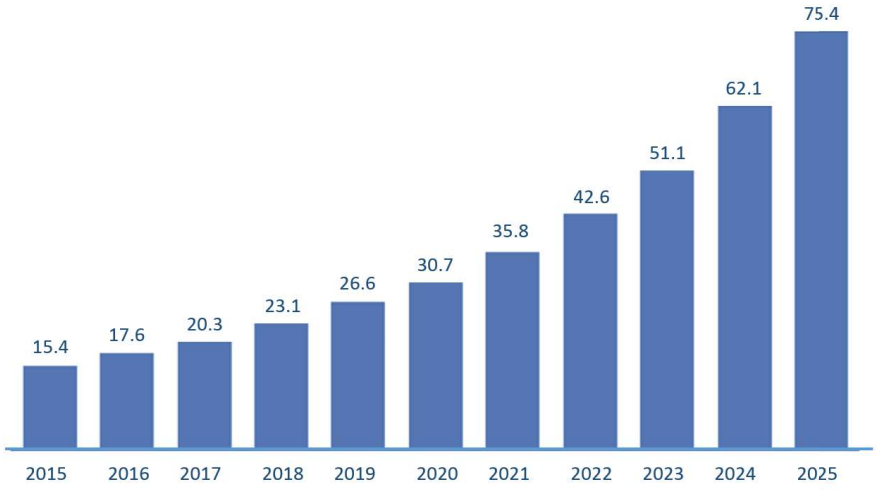


Figure 1.2: Number of IoT connected devices worldwide from 2015 to 2025. [23]

and devices for medical applications using organic light emitting diodes (OLEDs). (Figure 1.1, [20–22])

The incorporation of device electronics in our daily life has increased over the last years and it is expected that it will grow rapidly. With the fast pace development of the electronic devices and their integration into the internet of things (IoT), the number of connected devices is projected to be 75.44 billion worldwide by 2025, as predicted by Information Handling Services (IHS). (Figure 1.2, [23])

1.2 Motivation

Its has been only a few years since organic electronics have been demonstrated in consumer applications, but there are still several challenges that must be resolved. The stability of the electronic device, the charge carrier mobility and the overall OTFT parameters require further improvements. In the past few years, new organic semiconducting materials were able to achieve charge carrier mobility of 5 cm^2/Vs, which is the minimum requirement for instance to drive an LED. Parameters, such as threshold voltage and contact resistance of the OTFTs should be eliminated in order to operate them with minimum voltage application. There are several ways to tackle these issues, with the main one being the molecular doping. This concept was adapted from the inorganic semiconductors field. Doping is a simple method where small amounts of a molecular dopant are added in the organic semiconducting solution. Doping leads to organic semiconductors with enchanced charge transport properties, as well eliminates issues OTFT's performance.

For integrated circuits it is required to have balanced transport between electrons and holes, thus studying the doping of both p and n-type organic semiconductors is essential. Hole transporting semiconductors have higher mobility than the n-type semiconductors. Thus doping of n-type organic semiconductors (OSCs) is of great importance. There are several limitations on identifying potential n-type dopants, with the main one being that the majority of them are not air stable, due to the position of their energy levels. Molecular doping of n-type OSCs has been proven rather challenging and thus the synthesis or identification of new materials that can effectively dope the n-type OSCs is crucial. In summary, molecular doping of organic semiconductors for thin film transistors appears to provide a generic approach not only to increase the charge carrier transport properties, but also improve the overall performance of the device, which are required for commercial applications.

Depending on the properties of the organic semiconductors, they have application in several devices. Thus, identifying the properties of new materials can lead to new device applications.

1.3 Thesis Outline

The focus of this thesis is the development of high performing organic thin film transistors (OTFTs) from both p and n-type organic semiconductors (OSCs). This was achieved by the addition of a molecular dopant in the OSC formulations. An increase in the charge transport properties and reduction in the parasitic resistance was observed for the p and n-type systems studied. An organic polymer:small molecule blend is also demonstrated for its application in organic light emitting transistors (OLETs).

Chapter 2 gives an overview of organic semiconductors including their electronic properties and various models used to describe their charge transport properties. A literature review of the OSCs used for OTFTs then follows for both small molecules and polymeric materials. Furthermore, a brief description of the operation mechanisms of the TFTs is given along with the crucial interfaces of the device, which affect the charge carriers. Finally, a brief overview of the light emitting transistors (OLETs) structures and organic materials used so far is given.

Chapter 3 highlights the importance of molecular doping for OTFTs and discuss the doping mechanisms. The different doping approaches, along with their effect in the OTFTs then follows.

Chapter 4 describes in detail the experimental methods used to fabricate OTFTs and OLETs. An overview of the basic principles of the experimental techniques used to study the device's properties and the thin films is also given.

Chapter 5 is based on the research performed on p-type OSCs. The use of $B(C_6F_5)_3$ as an effective p-type dopant is demonstrated in several small molecules, polymers and their blends. The molecular dopant showed it has a dual function in the OSC layer to increase the performance of the OTFT and to induce long range crystallinity.
This research is published in: J. Panidi, A. F. Paterson, D. Khim, Z. Fei, Y. Han, L. Tsetseris, G. Vourlias, P. A. Patsalas, M. Heeney, T. D. Anthopoulos, 'Remarkable enhancement of the hole mobility in several organic small-molecules, polymers, and small-molecule:polymer blend transistors by simple admixing of the Lewis acid p-dopant $B(C_6F_5)_3$' Advanced Science 2018, 5, 1700290.

Chapter 6 demonstrates the use of a new n-type OSC as a molecular dopant in a small molecule and a polymeric semiconductor. Doping was verified by both theoretical and experimental techniques.
This research is published in: J. Panidi, J. Kainth, A. F. Paterson, S.Wang, L. Tsetseris, M.A. McLachlan, M.Heeney, T.D. Anthopoulos, 'Introducing a nonvolatile n-type dopant drastically improves electron transport in polymer and small molecule organic transistors', Advanced Functional Materials 2019, 29, 1902784.

Chapter 7 demonstrates the first light emitting transistor fabricated from a single organic semiconductor layer, with the use of a light emitting polymer, which also has

high charge transport properties.

This research is published in: M. U. Chaudhry, J. Panidi, A. Smith, J. Lim, K. Tezner, P. A. Patsalas, G. Vourlias, W. Y.Sit, Y. Firdaus, M. H. Heeney, D.D. C. Bradley, T. D. Anthopoulos, 'Polymer light-emitting transistors with charge carrier mobility exceeding $1cm^2/Vs$', Adv. Electron. Mater. 2019, 1901132.

Chapter 8 summarises the key findings of the work as performed for this thesis, as well as proposes the next steps for future work.

Chapter 2

Charge transport in OSCs

This chapter gives a brief review of the electronic properties of organic semiconductors (OSCs) and devices. In the first section, the theory of charge transport carriers is analysed, including the variable range hopping and multiple trapping and release method. The next section is then focused on suitable OSC materials for organic thin film transistor applications. In the last section, the thin film transistors' principles are described along with their ability to be used as light emitting devices.

2.1 Electronic properties of organic semiconductors

Macroscopically, inorganic and organic semiconductors behave in a similar manner; however they possess significant differences, one of them being their charge transport mechanisms. In inorganic semiconductors, charges are considered to move within a delocalised electronic structure in the crystalline lattice and they undergo phonon scattering. Controversy, in organic semiconductors charge transport is a phonon-assisted process with charges hopping from one localised state to another. This chapter describes the electronic properties of organic semiconductors, explaining the various charge transport models that have been reported. [24, 25]

2.1.1 Molecular Orbitals

Organic semiconductors are materials mostly containing carbon and hydrogen atoms, with possibly some heteroatoms such as nitrogen and sulfur. Understanding the electronic structure at the molecular level is required in order to a get an insight in to their charge transport behaviour.

The organic semiconducting properties arise from the conjugated carbon framework, whose electronic structure is presented in Figure 2.1. Carbon has six electrons in its ground state with the electronic structure in the configuration of $1s^2 2s^2 2p^2$ and thus few combinations (hybridisation) of s and p-orbitals can be formed. For charge transport in the organic semiconductor, sp^2 hybridisation is the most crucial. Electrons from the 2s orbital are promoted to the 2p molecular orbital and they are distributed into three sp^2 and one in $2p_z$ orbitals (Figure 2.1.1a). In the hybridised state, each orbital contains unpaired electrons and each sp^2 forms σ-bonds, while the $2p_z$ forms a π-bond. When other atoms, such as carbon or hydrogen approach, the energy difference between the 2s and 2p compensates and new hybrid orbitals are formed. The bonds that are formed between the molecules depends on the number of hybrid orbitals and the remaining p-orbitals.

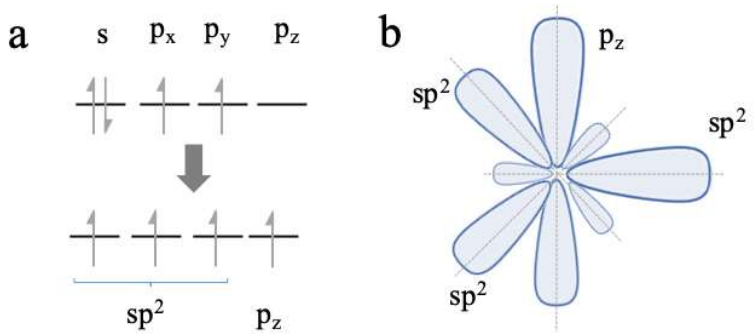


Figure 2.1: a) Formation of sp^2 hybridisation of carbon and b) schematic of atomic orbitals after the hybridisation.

The energy levels of the OSCs can be identified from the p-orbitals. Hückel theory is applied, since their structure can be approximated by the linear combination of atomic orbitals (LCAO). This theory only considers the neighbouring interactions and by following Pauli's principle, electrons are filling the states with anti-parallel spin until the highest occupied molecular orbital (HOMO). The next energy level is termed the lowest unoccupied molecular orbital (LUMO). Considering the two $2p_z$ orbitals, their overall wavefunction will be a linear superposition of these atomic orbitals leading to two molecular orbitals; bonding and antibonding. The energy levels will split into two bands in order to lower the overall energy of the system, where this phenomenon is called Peierls distortion and is responsible for the semiconducting properties of the conjugated materials. This gap that has been generated between the HOMO and the LUMO energy level is known as bang gap (E_g). [24, 26]

2.2 Charge transport models

In inorganic semiconductors and highly ordered organic crystals, electrons are loosely bound within a periodic potential well. Solutions to the Schrödinger equation results in periodic and continuous electronic bands/levels separated by energy gaps, in the reciprocal space. Electrons fill the valence band up to the Fermi energy (E_F), which is inside the band gap (E_g). According to Fermi-Dirac statistics, at finite temperature electrons can be found in the conduction band, therefore charge transport under an electric field is possible. The mobility of the carriers is inversely dependent on the temperature ($\mu = (m^*)^{-5/2}\ T^{-3/2}$), where m^* is the effective mass of the carrier and T is the absolute temperature. This inverse dependence on the charge carrier mobility with the temperature is a characteristic of the band-like charge transport in semiconductors.

2.2.1 Variable range hopping

In most organic semiconductors due to several factors the band-like model is not appropriate to describe charge transport. These factors include weak orbital overlap, high levels of disorder and the existence of defects. Thus, several models have been developed and they can be divided in two main categories, where the rate of charge transport depends mainly on the hopping rate of the carriers and to those where the rate depends on the trapping of charges. In the variable range hopping model (VRH), as developed by Mott, charges are able to hope between sites (localised states).[27] This model takes into account the distance that the charges are travelling, thus it allows hopping over a large distance with a low energy barrier and short distance with high energy barrier. The charge carrier mobility is given by Equation 2.1, where μ_o is the mobility prefactor and T_o is a function of the density of states (DOS), which

determines the number of available states in a system, at E_F and the orbital overlap of the wavefuctions. This model has been applied for amorphous and crystalline organic semiconductors, but it assumes a constant density of states thus large distance hopping is often overestimated. [28]

$$\mu = \mu_o \ \ exp(T_o/T)^{-1/4} \tag{2.1}$$

2.2.2 Multiple trapping and release Meyer-Nelson model

The statistical variation between the molecules in organic semiconductors will cause a broadening in the DOS leading to tail states inside the E_g. Moreover, organic semiconductors often have chemical impurities, breaks in the conjugation length and grain boundaries which may cause other localised states/traps. When charges are captured by the traps, they are not able to contribute to the charge transport and so the conductivity is dependent on the traps, as shown in Figure 2.2. Charge carriers with thermal energy may be activated and released up to the transport energy level (E_T). The time it takes for the carrier to become mobile again will be a function of the E_T and the temperature.

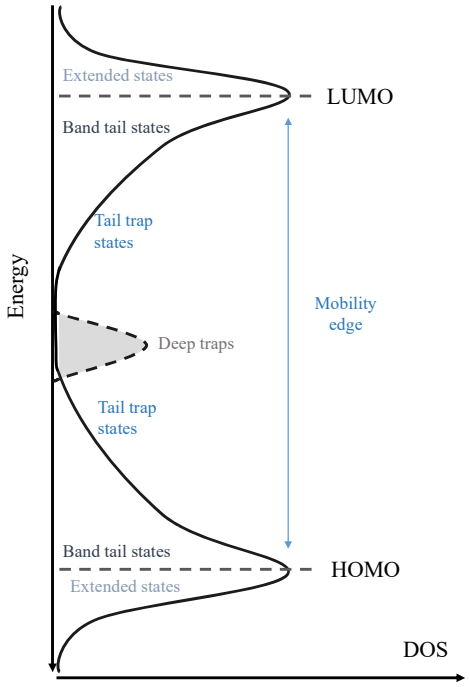


Figure 2.2: Density of states (DOS) of an organic semiconductor as suggested by the multiple traps and release model.

The most common model used for organic semiconductors is the Multiple Trap and Release model (MTR), in which the charge transport rate is dependent on the trapping and release rate of the carriers below E_T. MTR assumes that every single trap will

capture a charge carrier and it will be only be mobile again after thermal activation. Thus, the effective charge carrier mobility (μ_{eff}) will be temperature dependent as presented in Equation 2.2,

$$\mu_{\text{eff}} = \mu_{\text{o}} \frac{N_{\text{c}}}{N_{\text{tr}}} \ exp\left(-\frac{E_{\text{A}}}{kT}\right) \tag{2.2}$$

where N_c and N_{tr} is the density of traps and of the transport states level and E_A is the activation energy. More specifically, E_A is the energy level of the trap with respect to the E_T level (E_A=E_T- E_V). A Gaussian DOS is used for the hopping models, but in this model the tail states are considered too, which are in the band gap between HOMO-LUMO levels, as shown in Figure 2.2. Thus, an exponential distribution for the density of traps is more applicable, as it is presented in Equation 2.3,

$$N_{\text{tr}} = N_{\text{tr}}^{\text{o}} \ exp\left(-\frac{E_{\text{A}} - E}{kT_{\text{o}}}\right) \tag{2.3}$$

where kT_o is the width of the trap distribution. When bias is applied the E_F is shifted towards the $E_{T'}$ and the mobility becomes gate voltage (V_G) dependent, since the increase of the gate voltage results in trap filling. Charge carrier mobility increases with the application of V_G and it can be described from Equation 2.4.

$$\mu_{\text{eff}} = \mu_{\text{o}} \frac{N_{\text{c}}}{N_{\text{tr}}^{\text{o}}} \ exp\left(-\frac{E_{\text{A}}}{kT} + \frac{E_{\text{A}}}{kT_{\text{o}}}\right) \tag{2.4}$$

By simplifying Equation 2.4 with the Meyer-Neldel relationship the effective mobility becomes a function of the activation energy (Equation 2.5).

$$\mu_{\text{eff}} = \mu_{\text{o}} \ exp\left(-\frac{E_{\text{A}}}{kT}\right) \tag{2.5}$$

The activation energy can then be extracted from the Arrhenius plots of the effective mobility vs the inverse of temperature by varying the gate voltage. [29–32] Further analysis on the activation energy and the doping mechanism is given in a latter section in this thesis (Chapter 3.3.2).

2.3 Organic semiconducting materials

In this section organic semiconductors and their applications in thin film transistors will be reviewed. In the past few years significant progress has been made in the synthesis and/or improvement of the organic semiconductors leading to materials with enhanced charge transport properties. For instance, by careful selection of the side groups of the molecule, several parameters can be improved such as the solubility, the electrical properties as well as the packing. Enhanced π-π stacking can also be achieved by increasing the π-bond orbital overlap, which improves the electronic coupling between

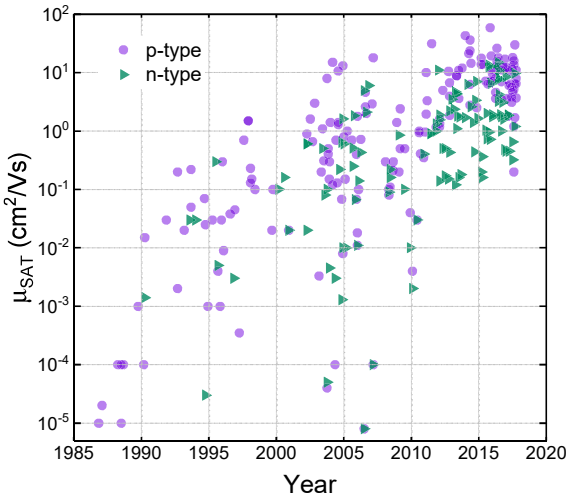


Figure 2.3: Charge carrier mobility in saturation regime for p and n-type organic semiconductor over 30 years. [34]

the molecules [33].

Charge carrier mobility of both p and n-type organic semiconductors developed over time is presented in Figure 2.3, as adapted from the literature. [34] Remarkable enhancement in the mobility values is observed around the 1990s. Over the past few years, the number of reports on high mobility materials has increased and it can be seen that p-type materials generally show higher charge transport properties than n-type materials, as described earlier.

2.3.1 Polymeric semiconductors

Various polymeric semiconductors with enhanced charge transport properties have been designed in the past few years. Examples of organic semiconductors with application in organic electronic devices are presented in Figure 2.4. Milestone materials in the organic electronics area are poly(3-hexylthiophene-2,5-diyl) (P3HT), poly[5,5-bis(3-alkyl-2-thienyl)-2,2-bithiophene] (PQT) with improved performance and poly(2,5-bis(3-hexadecylthiophen-2-yl)thieno[3,2-b]thiophene) (pBTTT), where it has been shown that the charge transport is occurring in the π-stacking direction. [35–38]

The synthesis of poly(indacenodithiophene-co-benzothiadiazole) C_{16}IDT-BT showed the important relationship between molecular rigidity and charge carrier mobility. The long conjugated chains help to bridge the poorly ordered and amorphous phases with in the polymer aggregates, where they act as electrical pathways for the charges, resulting in a hole mobility of 3.6 cm^2/Vs. [39] Moreover, a molecular weight of 100 kDa in poly[2,6-(4,4-bis-alkyl-4H-cyclopenta-[2,1-b;3,4-b0]-dithiophene)-alt-4,7-(2,1,3-

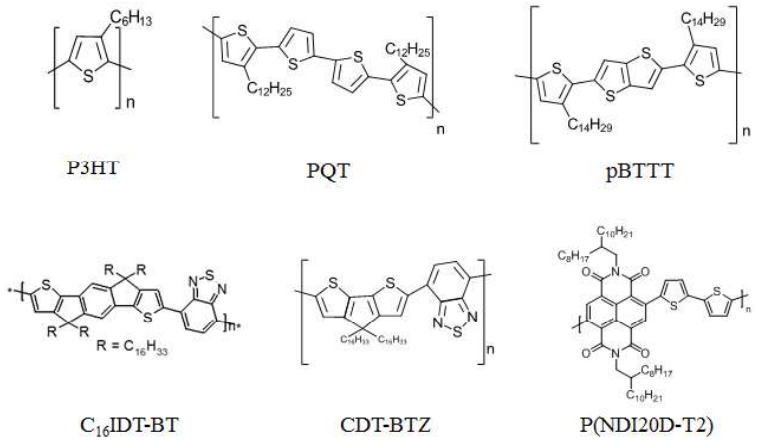


Figure 2.4: Molecular structures of a few conjugated polymers often used for organic electronics applications.

benzothiadiazole)] (CDT-BTZ) films with improved degree of crystallinity resulted in transistors with a mobility higher than 3 cm^2/Vs. [40]. Poly[N,N'-bis(2-octyldodecyl)-naphthalene-1,4,5,8- bis(dicarboximide)-2,6-diyl]-alt-5,5'-(2,2'-dithiophene) [P(NDI2OD-T2) was found to be an n-type material with high mobility (1 cm^2/Vs) and air stability. [41, 42]

2.3.2 Small molecule semiconductors

Organic small molecules are another category of semiconducting materials (Figure 2.5); they are highly crystalline and often they possess higher charge carrier transport properties than polymers.

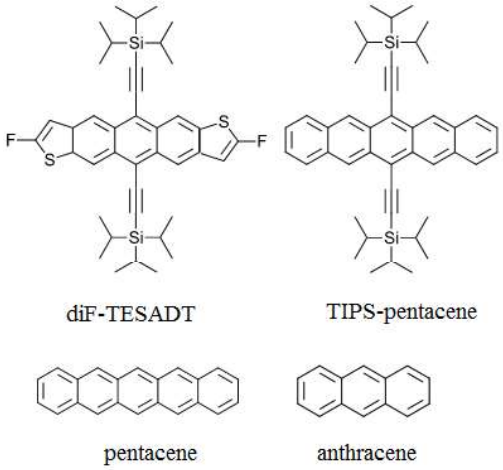


Figure 2.5: Molecular structures of a few small molecules used for OTFT applications.

A drawback of small molecules, on the other hand, is that it is challenging to process them from solutions and sometimes advanced processing techniques are required.

For example, pentacene molecules are not soluble, but when thin films are deposited by thermal evaporation, OTFTs result in a charge carrier mobility of 3 cm^2/Vs. [43] The addition of TIPS in the pentacene, as reported by J. Anthony, led to the development of a soluble derivative, 6,13-bis(triisopropylsilylethynyl) pentacene (TIPS-pentacene). [44, 45] Other acene molecules were reported including tetracene and rubrene, where the latter has the highest mobility (15 cm^2/Vs) when transistors are fabricated from single crystals. [46] By combining acene and thiophene units, several small molecules were synthesised including anthradithiophenes and benzothiophenes. [47, 48] Another material similar to TIPS-pentacene is 2,8-difluoro 5,11-bis(triethylsilylethynyl) anthradithiophene (diF-TES ADT), which is soluble and has a two dimensional π-stacked crystal structure, with a charge carrier mobility of 6 cm^2/Vs, when OTFTs were fabricated from single crystals. [49, 50] Several other categories of small molecules exist for organic optoelectronic applications. [51]

2.3.3 Organic semiconducting blends

Organic semiconductor blends, consisting of a polymer-polymer or a polymer-small molecule are commonly used for bulk heterojunction solar cell applications [52] and in organic light emitting diodes. [53] More recently, organic blends composed of a small molecule and a polymer have been used for thin film transistor applications. Small molecules offer high mobility, but often they tend to crystallise strongly when processed from solution. Also due to the formation of high anisotropic films, there is often device to device variation. Thus the key for high performing devices controlled crystallisation of the small molecule film is the key. [29, 54–56] On the contrary, polymeric semiconductors are either amorphous or crystalline over small lengthscales, which results in excellent film uniformity and thus parameter uniformity across the substrate. The disadvantage of the polymers are their lower charge carrier mobility. By blending these two categories of the OSC materials in a specific concentration there is a significant benefit; the OSC blend will have the mobility of the small molecule and the film forming properties of the polymer. [57–61]

An interesting mechanism that is occurring in the organic blend semiconductors is the vertical phase separation, as presented in Figure 2.6. The organic blend solution contains both the small molecule and the polymer. By solvent evaporation, for example during spin coating and thermal annealing, the small molecule migrates to the top of the film surface. In the resulting thin film, the first few nanometers consist only of the small molecule and the polymer layer is underneath. Several techniques have been used to verify this theory, including dynamic secondary ion mass spectrometry (D-SIMS), where it was observed that the first 20-30 nm of the film consist of the small molecule for the diF-TESADT:PTAA blend. [58] Moreover, to achieve this high mobility device

the small molecule, since it has higher mobility than the polymer, should be in the channel of the device, and thus OTFTs in bottom-contact top-gate are desirable.

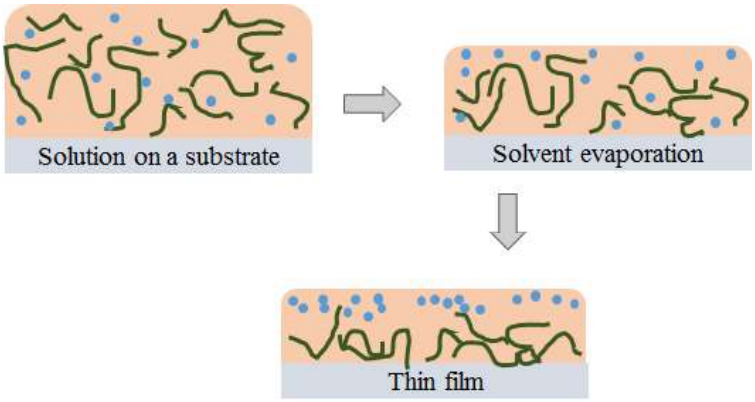


Figure 2.6: Schematic representation of the vertical phase separation mechanism that is observed in the small molecule:polymer blends. Initially both the polymer and the small molecule are distributed in the solution; after spin coating or thermal annealing the solvent evaporates and a final thin film is produced, where the small molecule is on the top and the polymer underneath.

Insulating polymers, such as poly(a-methylstyrene) (PaMS), polystyrene (PS) and poly(methyl methacrylate) (PMMA) have been blended with TIPS-pentacene and diF-TESADT, and their charge transport and morphological properties have been studied by several groups. [55, 56, 58, 61] Another example of a high performing OSC blend is the C_8-BTBT with PS, which showed high charge transport properties when deposited by off-center spin coating. [53] A well-studied blend, or otherwise the so-called first generation blend, the diF-TESADT:PTAA was first reported by Hamilton et al. with a hole mobility of 2.4 cm^2/Vs from solution processing. [55] This study showed that by careful optimisation of the small molecule to polymer ratio, the solvent selection and the thin film processing, higher mobility than the small molecule itself can be obtained. A few years later Smith et al. replaced PTAA with poly(dialkyl-fluorene-co-dimethyl-triarylamine) (PF-TAA) in diF-TESADT:PTAA blend resulting in hole charge carrier mobility of 5 cm^2/Vs. [61] More recently, Paterson et al. reported a new blend by using the small molecule 2,7-dioctyl[1]benzothieno[3,2-b][1]benzothiophene (C_8-BTBT) and the polymer indacenodithiophene-benzothiadiazole (C_{16}IDT-BT) with hole mobility to obtain a 4.7 cm^2/Vs. [57]

2.4 Thin film transistor (TFT) model

2.4.1 TFT architectures

Various device architectures are available to fabricate thin film transistors, which are presented in Figure 2.7. The key in these architectures is the position of the semicon-

ductor and dielectric layer, as their interface is significant for device operation. For instance, in a bottom-gate (Figure 2.7a,c) device architecture the dielectric surface plays a crucial role as it is deposited before the semiconductor layer, whereas in a top-gate (Figure 2.7b,d) device the surface of the semiconductor is more important. Further analysis on the importance of the semiconductor-dielectric interface and their role in the device is given in Chapter 2.4.4. Another parameter that needs consideration when device architecture is chosen, is if in the organic semiconductor layer, vertical phase separation is occurring as for instance in the OSC blends. Careful consideration is required for the solvent selection of the organic semiconductor and dielectric layer when both are prepared from solutions. Common issues, include the solvent of the second layer dissolving the layer underneath, or due to the difference in polarity of the solvents dewetting can occur. Furthermore, the contact's position and the metal selection influences the electric field distribution in the organic semiconducting layer. In the work that was performed for this thesis, bottom-contact top-gate devices were selected as a tool to evaluate the materials used and this will be discussed in the Results sections.

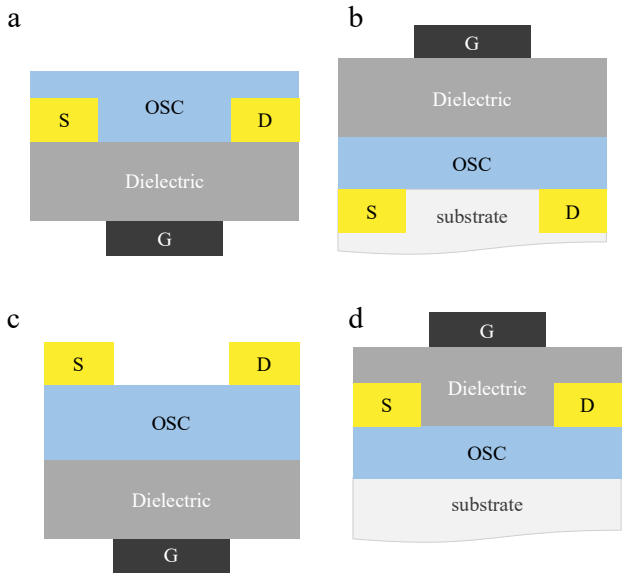


Figure 2.7: Thin film transistor architectures for (a) bottom-gate bottom-contact (BG-BC), (b) top-gate bottom-contact (TG-BC), (c) bottom-gate top-contact (BG-TC) and (d) top-gate top-contact (TG-TC).

2.4.2 Operation principles

The following section will explain the operating principles of the thin film transistors (TFTs) and how device parameters can be extracted, such as the charge carrier mobility of the semiconductor, threshold voltage and other TFT properties.

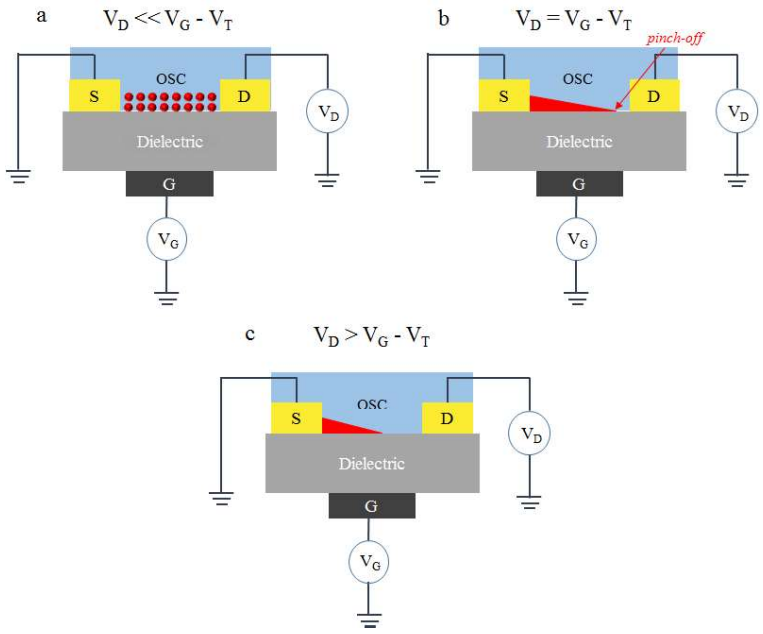


Figure 2.8: Thin film transistor architecture in bottom gate (G) bottom contact (S,D) configuration. (a) A uniform channel is formed when a small V_D is applied (linear regime). (b) By increasing the V_D, the channel starts to pinch-off and the resistance is increased. (c) At higher V_D application the channel is pinched-off close to the drain.

A thin film transistor is a three-terminal device, as presented in Figure 2.8, where the source (S) and drain (D) electrodes are used for injection and extraction of the carriers into the semiconducting material. The third terminal is the gate (G) electrode, which is separated from the semiconductor by a dielectric layer and modulates the current flow between the source-drain electrodes. The voltage application in the drain electrode (V_D) induces a drain current (I_D) between the source and drain, while the source remains grounded. The application of the gate voltage (V_G) causes the accumulation and depletion of charge carriers at the semiconductor/dielectric interface, and thus a conductive channel is formed, as shown in Figure 2.8a. The channel's resistance is controlled by the applied gate voltage (V_G). The device is in the linear regime, when it obeys the following condition; the applied $V_D \ll V_G - V_T$, where V_T is the threshold voltage. Threshold voltage is the minimum voltage required to accumulate enough charge carriers in the device channel to form a conductive pathway between source and drain. Thus the mobile charge is given by Equation 2.6

$$Q_A = C_i(V_G - V_T) \tag{2.6}$$

where C_i is the geometric capacitance. The required time of the charges to travel across the device channel will be related to the drain current as it is presented in Equation 2.7,

$$I_{\mathrm{D}} = \frac{Q_{\mathrm{m}} W L}{t} \tag{2.7}$$

where W is the width and L is the length of the device channel. By assuming that the velocity of the charge carriers is constant in the channel, the velocity will be given by multiplying the mobility (μ) with the electric field (E). Thus the velocity will be given by Equation 2.8.

$$\nu = \mu E = \mu \frac{V_{\mathrm{D}}}{L} \tag{2.8}$$

By combining Equations 2.7 & 2.8 the drain current in the linear ($V_D \ll V_G - V_T$) regime of the transistor can be obtained from Equation 2.9.

$$I_{\mathrm{D}} = \mu C_{\mathrm{i}} \frac{W}{L} (V_{\mathrm{G}} - V_{\mathrm{T}}) V_{\mathrm{D}} \tag{2.9}$$

By further increasing the application of the V_D, as such it becomes equal to V_G–V_T (Figure 2.8b) the channel diminishes its thickness towards the drain electrode (pinch-off). When V_D>V_G–V_T, then the device is in saturation regime and a depleted region is formed close to the drain electrode. This is a high resistance region and the current equation for the V_D>V_G–V_T (Figure 2.8c), region is described by Equation 2.10.

$$I_{\mathrm{D}} = \mu C_{\mathrm{i}} W (V_{\mathrm{G}} - V_{\mathrm{T}} - V_{\mathrm{C}}) \frac{dV_{\mathrm{C}}}{dx} \tag{2.10}$$

By integrating along the device channel:

$$\int_0^L I_{\mathrm{D}} = \mu C_{\mathrm{i}} W \int_0^{V_{\mathrm{D}}} V_{\mathrm{G}} - V_{\mathrm{T}} - V_{\mathrm{C}} \;\; dV_{\mathrm{C}} \tag{2.11}$$

Then the drain current in the saturation regime is (Equation 2.12).

$$I_{\mathrm{D}} = \mu C_{\mathrm{i}} W \frac{W}{L} \left((V_{\mathrm{G}} - V_{\mathrm{T}}) V_{\mathrm{D}} - \frac{V_D^2}{2} \right) \tag{2.12}$$

2.4.3 Parameter extraction

There are several pieces of information that can be extracted from the transfer characteristics (I_D vs V_G) of a transistor. These include parameters such as the charge carrier mobility of the semiconductor, the on/off current ratio and the subthreshold swing (S.S.) of the TFT.

The charge carrier mobility in the linear (Equation 2.13) and saturation regime can be calculated by the drain-current Equations 2.9 and 2.12. For the linear regime, where $V_D \ll V_G$–V_T the charge carrier mobility is:

$$\mu = \frac{1}{C_{\mathrm{i}} V_{\mathrm{D}}} \frac{L}{W} \frac{\partial I_{\mathrm{D}}}{\partial V_{\mathrm{G}}} \tag{2.13}$$

In a similar manner, the mobility can be extracted from the saturation regime (Equation 2.14), where $V_D > V_G - V_T$:

$$\mu = \frac{1}{C_i V_D} \frac{L}{W} \frac{\partial^2 I_D}{\partial V_G{}^2} \tag{2.14}$$

Otherwise, the second derivative of the drain current can be calculated from the first derivative of the square root and thus extract the slope of the I_D^2 vs V_G, as shown in Figure 2.9 and apply it to Equation 2.15.

$$\mu = \frac{1}{C_i V_D} \frac{2L}{W} \left(\frac{\partial \sqrt{I_D}}{\partial V_G} \right)^2 \tag{2.15}$$

An example of a transfer curve, as measured for a p-type thin film transistor in both linear (green curve) and saturation (blue curve) regime is presented in Figure 2.9. The on and off-states of the device are indicated by the purple line, where by diving these values the device's $I_{ON/OFF}$ ratio can be extracted. The onset voltage (V_{ON}) is when the I_D sharply increases after the off-state. From the linear fit of the square root of the I_D the threshold voltage (V_T) can be obtained. The grey highlighted box in Figure 2.9 shows the subthreshold swing (S.S,) region, which is the region between the V_T and V_{ON}, and it can be extracted from Equation 2.16.

$$S.S. = \frac{\partial V_G}{\partial (log I_D)} \tag{2.16}$$

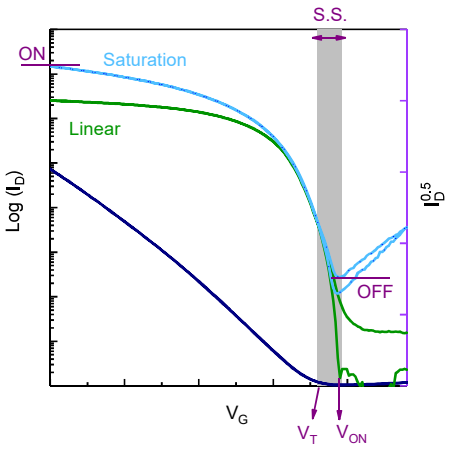


Figure 2.9: Transfer characteristic of a thin film transistor in both linear and saturation regime. The square root of the drain current in the saturation regime is also plotted (right axis). By a linear fitting of the $I^{0.5}$ the threshold voltage and the slope can be extracted.

The subthreshold swing is a useful parameter for the device, since it gives information about the trap density, as such a small value is required for transistor applications. Furthermore, the on/off current level depends on several factors of the devices. For

instance, the on-current strongly depends on the charge carrier mobility of the organic semiconductor, whereas the off-current depends on the dielectric and the traps states.

2.4.4 Semiconductor - Dielectric interface

2.4.4.1 Their role in the TFT

The semiconductor-dielectric interface is crucial for charge transport in the device. To begin with, the dielectric is required to have high resistivity in order to block carriers travelling from the semiconductor to the gate electrode. The selection of the dielectric material in the OTFTs determines several factors, including the required applied voltage to operate the transistor. For low power commercial applications, transistors are desirable to operate in voltages of the order of 5 V. [62] Its role in the transistor determines the amount of charges that can accumulate in the channel and its interface affects the charge transport, as traps can be formed. [63–65]

The relative dielectric permittivity (ϵ) of the dielectric material is used to calculate the geometric capacitance (C_i), as described by Equation 2.17,

$$C_{\mathrm{i}} = \frac{\epsilon \epsilon_{\mathrm{o}}}{d} \tag{2.17}$$

where d is the thickness of the dielectric layer. The value of the C_i is used to calculate the charge carrier mobility of the transistor, as explained in Chapter 2.4.3. There are mainly two categories of dielectric materials that are used for TFT fabrication, the low-k and the high-k, where k is the dielectric constant. Depending on the device application and device structure the dielectric material should have high dielectric strength, trap-free surface, low surface roughness and if it's used from solution the solvent choice has to be compatible with the semiconducting layer.

In a bottom gate (BG) transistor architecture crucial role plays the roughness and the traps in the dielectric layer. BG TFTs usually are fabricated on a heavily doped silicon wafer, which has a silicon oxide layer on top. In this case, the silicon's role is the gate electrode, whereas the silicon oxide is used as the dielectric. The silicon oxide layer has traps on its surface, due to the present of –OH groups, thus passivation with a self-assembled monolayer is required. Materials including hexamethyl disilazane (HMDS) and octadecyl trichlorosilane (OTS) are often used to passivate the SiOx surface. [66, 67]

For a top-gate (TG) transistor the dielectric constant and the polarity play an important role. Using polymeric materials as dielectrics, usually with lower ϵ than inorganics, leads to an increase in device performance. On the contrary, high-k materials have randomly oriented dipole moments which will lead to a broadened DOS due to the presence of more deep traps. [68, 69] For solution processed dielectrics, orthogonal

solvents should be used not to damage the organic semiconducting layer.

2.4.4.2 Trap density estimation

Electronic states below the energy transport level, which are called traps as described earlier, can arise from material impurities, disorder and defects in the semiconductor layer. From the transfer characteristics of a transistor, the trap concentration per unit area D_{tr} [energy]$^{-1}$ [length]$^{-2}$, the surface trap density N_{tr} [length]$^{-2}$ and the relative surface trap density ΔN_{tr} can be extracted.

The density of traps per unit area at the semiconductor – dielectric interface is given by Equation 2.18

$$D_{\mathrm{tr}} = \frac{C_{\mathrm{i}}}{e^2}\left(\frac{eS.S.}{kTln(10)} - 1\right) \tag{2.18}$$

where C_i is the geometric capacitance, e is the elementary charge, S.S. is the subthreshold swing, k is the Boltzmann constant and T is the temperature. The surface trap density and the relative surface trap density are given by Equations 2.19 and 2.20, respectively.

$$N_{\mathrm{tr}} = \frac{C_{\mathrm{i}}|V_{\mathrm{T}} - V_{\mathrm{ON}}|}{e} \tag{2.19}$$

$$\Delta N_{\mathrm{tr}} = \frac{C_{\mathrm{i}}|\Delta V_{\mathrm{T}}|}{e} \tag{2.20}$$

where V_T is the threshold voltage and V_{ON} is the onset voltage. These calculations assume that the majority of the injected charges, by the application of voltage in the transistor measurement, are trapped until $V_G = V_T$. [70, 71]

2.4.5 Metal - Semiconductor interface

The metal - organic semiconductor interface is important for transistor applications, as the ability to inject or extract charge carriers depends on the alignment of the energy levels of the metal and the semiconductor material. Fermi energy (E_F) alignment is occurring when a metal is brought next to a semiconductor and as a result of band bending a potential barrier is formed, called a Schottky barrier (ϕ_b) (Figure 2.10 a). For an n-type semiconductor, electrons will be injected into the LUMO of the semiconductor (for p-type, holes will be injected into the HOMO), thus the metal workfunction (ϕ_m) should be close to the LUMO level of the OSC. The interaction between the metal and the OSCthat will lead to the formation of interface dipoles and the vacuum level (E_{vac}) will shift (Figure 2.10b). In the case of a weak interaction, the E_{vac} is close to zero and the Mott-Schottky barrier limit will be obtained for the charge injection.

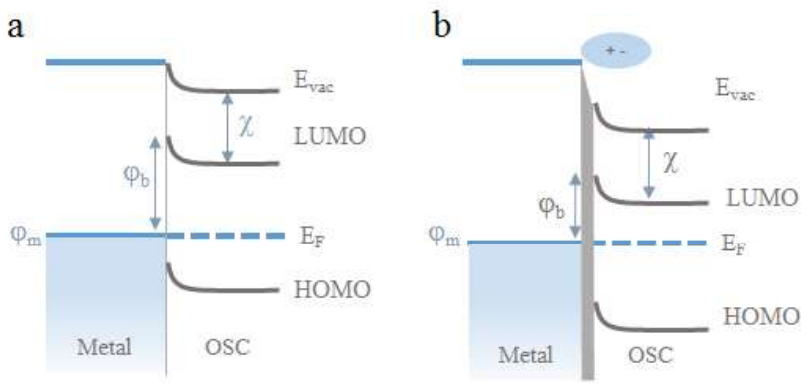


Figure 2.10: Metal – organic semiconductor interface band structure for electron injection from the LUMO (a) at the Mott Schottky barrier limit and (b) at the presence of an interface dipole.

An ohmic electrical contact can be achieved by careful material selection. More specifically, selecting a metal with a workfunction close to the energy level of the OSC of which the charge transfer is occurring, is important. A way to achieve this, is with the use of self-assembled monolayers (SAMs), as the workfunction of the metal can be tuned. SAMs covalently bond on the metallic surface thus modifying the workfunction, for instance, a fluorinated thiol (PFBT) is able to tune the workfunction of gold by 1 eV. [72]

For transistor applications, the injection barrier which is created between the metal – semiconductor interface leads to parasitic contact resistance (R_c). This parasitic resistance is responsible for the device function, for instance high threshold voltages, high turn-on voltage and non-linear output characteristics at low drain voltages. Furthermore, OTFTs which are suffering from R_c are not following the ideal transistor model, and thus a few extracted parameters, such as charge carrier mobility, can be overestimated.[73, 74]

There are several methods, one can calculate/measure the contact resistance in OTFTs, including the Y-function, the scaling law method, the 4-point probe method and the transfer line method (TLM). All of these methods can be used for OTFTs, but the TLM also takes into account the V_G dependence of the charge carrier mobility and the total resistance (Equation 2.21).

$$R_{\text{total}} = \frac{\partial V_{\text{D}}}{\partial I_{\text{D}}} \tag{2.21}$$

By plotting the R_{total} multiplied by the width of the transistor channel versus the channel length for different values of V_G, the contact resistance can be extracted from the resulting slope. This method to extract the contact resistance was applied in the

projects in this thesis. For device commercialisation the contact resistance should be as small as possible. [75, 76] There are several ways to eliminate contact resistance, with the main one being the use of molecular additives, which will be discussed in the next sections.

2.5 Organic light emitting transistors (OLETs)

Organic light emitting transistors (OLETs) are based on thin film transistors with their main difference being that light emission occurs when a voltage is applied in the device. OLETs have a broad spectra of applications in opto- and nanoelectronics, such as their incorporation in logic circuits, optical communication systems and displays. [77–81] As in the OTFTs, high mobility organic semiconductors, low contact resistance and high on/off ratio are required. Most importantly, the organic semiconductor should also emit light. The combination of the requirements of high mobility and light emitting properties of the organic semiconducting materials has proven to be challenging. The reason behind this is that by reducing the strength of the interchain interactions in the molecules in order to enhance light emission this often has a negative effects on the charge transport properties.[82]

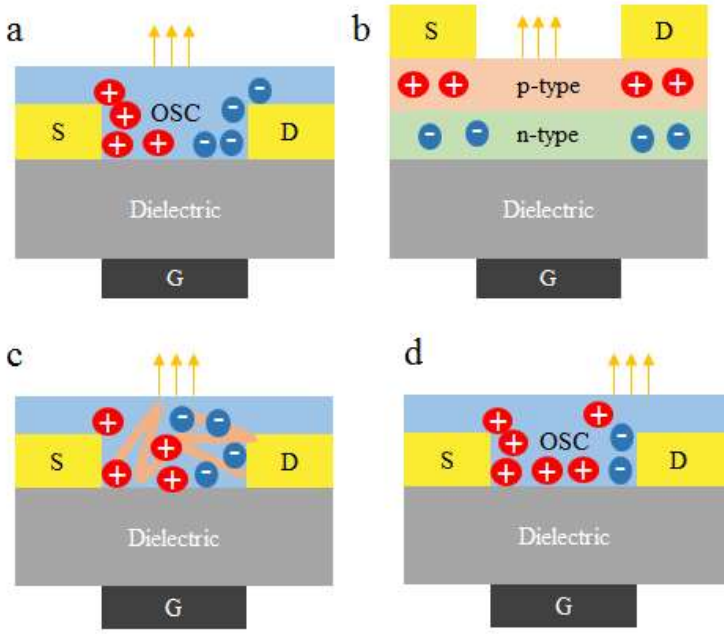


Figure 2.11: OLET device architecture when using (a) an ambipolar OSC, (b) a bilayer of OSCs, (c) a bulk heterojunction and (d) a unipolar device.

For light emitting devices the same structures, as described for thin film transistors (Chapter 2.4.1) can be applied. The light emitting layer can be a single layer, bilayer or in a bulk heterojunction structure. This depends on the properties of the organic

semiconductor used; for instance if the material is unipolar or ambipolar. Ambipolar organic semiconductors can generate both type of charge carriers, whereas a unipolar material only generates one. For highly efficient light emitting devices, both carriers are required.

The schematic illustration in Figure 2.11 shows the different types of light emitting materials that can be used. Figure 2.11a presents an ambipolar organic semiconductor, where the voltage application can accumulate both holes and electrons in the channel. Recombination of charge carriers occurs, when holes and electrons meet in the middle of the device channel. Red and green emissive OLETs were reported by Sirringhaus et al. using F8BT-based OLETs in a bottom-contact top-gate device architecture. [82] A bilayer structure using a,ω-dihexylquaterthiophene (DHT4) as a hole transporting layer and N,N' ditridecylperylene - 3,4,9,10 - tetracarboxylic diimide (PTCDI-$C_{13}H_{27}$) as electron transporting layer was demonstrated by Dinelli et al. with the emission zone being at the bilayer interface. [83] A bulk heterojunction OLET was reported by Rost et. al, where they used quinquethiophene (a-5T) as the hole transporting material and N,N'-ditridecylperylene-3,4,9,10-tetracarboxylic diimide (P13) as the electron injecting material. Hepp et. al. reported unipolar OLETs based on a tetracene thin film, where the charge recombination was occuring next to the drain electrode of the device.[84]

The device operating principle is the same as in the OTFT case (Section 2.4.2), where in OLETs both type of charge carriers will be generated in the device channel. Charges will then recombine and emit light. The position of the emission zone depends on the type of majority carriers in the channel. From the transfer curve's parameters, charge carrier mobility, threshold voltage, on/off current ratio by following procedures as described in Section 2.4.3, can be extracted.

2.6 Summary

In this chapter, the electronic properties of OSCs are described along with the main charge transporting mechanisms. The variable range hopping and the multiple trap and release model are explained. The main difference of these models is attributed to the crystallinity of the organic semiconductor. In particular the variable range hopping is applicable for amorphous OSCs, where charge transport is mainly due to hopping between the chains of the polymer. The multiple trap and release model takes into account the trap states in the organic semiconductor, which are formed from either impurities and/or grain boundaries. In crystalline semiconductors trap states exist and should be quantified, in order to understand the charge transport mechanism.

A brief review of polymer and small molecule OSCs then follows, as these have already been reported for thin film transistor applications. Furthermore, the basics of the transistors are then discussed, including the various device architectures, the

operation principles and methods for parameter extraction. For a thin film transistor not only the transporting layer plays a significant role, but the OSC-dielectric interface, as well as the metal-OSC injection barrier. The importance of these interfaces and the issues that can affect the overall device characteristic are discussed. Lastly, the operating principle of an organic light emitting transistor along with the current limitations in this field are described.

Chapter 3

Molecular Doping

In this chapter a brief overview of molecular doping of the organic semiconductors is discussed. Several models are used in order to explain the charge transport in the doped OSCs systems with the main ones being the ground state integer charge transfer and the hybrid charge transfer. Furthermore, emphasis is placed on the different doping methods for OTFTs and how it affects the device performance.

3.1 Introduction

Heeger et al., in 1977 first reported that exposing films of polyacetylene in chlorine, iodine or bromine vapour increases the conductivity by several orders of magnitude. [85] This breakthrough result led to an exciting research field with great technological applications. [86] Several reports since then have been published showing the range of applications of doped semiconductors and various models are used to explain the charge transport mechanisms. The molecular doping of organic semiconductors is a generic approach to enhance the charge transport of the materials and improve the device performance. Doping of organic semiconductors for organic photovoltaic devices (OPVs) [87, 88] and organic light emitting diodes (OLEDs) [89, 90] has proven a successful technique as it results in stable and high performing devices. In this section, both the materials and the mechanisms are discussed for thin film transistors applications.

3.2 Doping mechanism

3.2.1 Ground state integer charge transfer

Several models have been reported so far in order to examine the doping mechanism of OSCs, with the most studied one being the ground state integer charge transfer (ICT) mechanism. The key behind a successful charge transfer between the organic semiconductor (host) and the dopant is the position of their energy levels, according to the ICT mechanism. More specifically, for p-type organic semiconductors, the energy difference between the HOMO of the host and the LUMO of the dopant should be small (and vice versa for an n-type system). As shown in Figure 3.1 for a p-type OSC system, the HOMO of the OSC and the LUMO of the dopant should be energetically close in order for charge transfer to occur, whereas for an n-type system the energy difference between the HOMO of the dopant and the LUMO of the OSC plays a crucial role. [91]

Several examples of p-type doping have been reported so far based on this charge transfer mechanism. The polymer poly(3-hexylthiophene) (P3HT) was effectively doped by ICT when 2,3,5,6 - tetrafluoro7,7,8,8 - tetracyanoquinodimethane (F_4-TCNQ) was added. The doped system showed a 30-fold increase in the charge carrier mobility, as well as a shift in the threshold voltage of the transistors closer to zero voltage. [94] The small molecule [N,N,N,N-tetrakis(4 -methoxyphenyl)-benzidine] MeO-TPD it was found to be successfully doped by F_6-TCNQ, via the conventional ICT mechanism. The doping was verified by a shift in the Fermi level, as the dopant was filling the trap states. [92]

An organic semiconducting blend, consisting of the small-molecule 2,7-dioctyl[1] benzothieno[3,2 - b][1]benzothiophene (C_8 - BTBT) and the polymer indaceno-dithiophene-

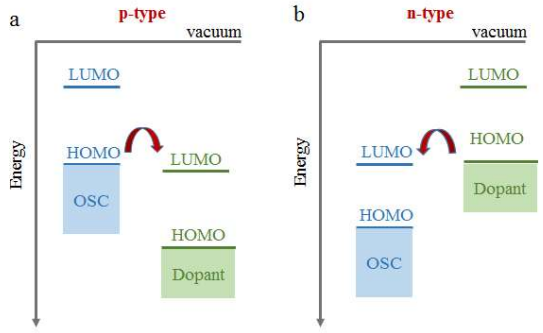


Figure 3.1: Integer charge transfer mechanism for (a) a p-type OSC system, where electrons are transferred from the HOMO of the OSC to the LUMO of the dopant and (b) for a n-type OSC system, where electrons are transferred from the HOMO of the dopant to the LUMO of the OSC.

benzothiadiazole (C_{16}IDT - BT), showed that it can be doped by $C_{60}F_{48}$ resulting in stable and high charge carrier hole mobility devices (13 cm^2/Vs). ICT was shown to have occurred, due to the position of the energetics of the organic blend semiconductor and the $C_{60}F_{48}$. [93, 94]

3.2.2 Hybrid charge transfer complex

For the ICT mechanism, a complete electron transfer from the host organic semiconductor to the dopant occurs, as described in Section 3.2.1. There are several cases where partial electron transfer has been observed with the formation of a supramolecular charge transfer complex (CTC). The energy levels of the complex are derived from the HOMO of the host, in its neutral case, and of the LUMO of the dopant. This charge transport mechanism results in a localised charge on the ionised dopant and a mobile hole, in the OSC. [91, 95] A schematic of the intermolecular hybridisation for a p-type OSC and a p-type dopant is presented in Figure 3.2.

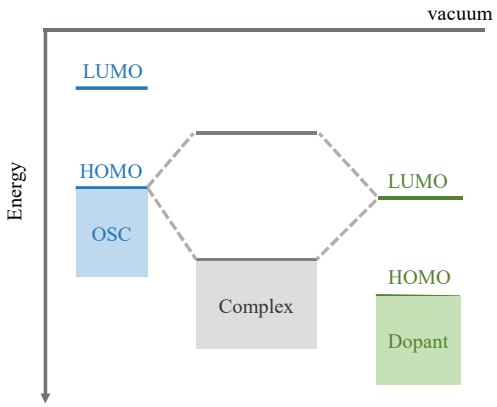


Figure 3.2: Charge transfer complex formation for a p-type OSC and a dopant system.

In several organic systems CTC has been observed, when F_4-TCNQ doped the small

molecule C_8-BTBT. [96] Intermolecular hybridisation was also observed in pentacene doped F_4-TCNQ, by ultraviolet photoelectron spectroscopy (UPS). [97] A charge transfer complex formation was also observed in the case of P3HT:F_4-TCNQ by using a combination of techniques including density functional theory (DFT) and X-ray absorption near edge structure measurements (XANES).[98] A complex was formed between the indenopyrazine polymer and a Lewis acid $B(C_6F_5)_3$, when a small amount of the acid was added in the polymer and a significant increase in the charge carrier mobility was obtained. [99] Negative radical formation in [6,6]- phenyl C_{61} butyric acid methyl ester (PCBM) was observed when (4-(1,3-dimethyl-2,3-dihydro-1H-benzoimidazol-2-yl)phenyl)dimethylamine (N- DMBI) was added, resulting in increased conductivity. [100]

3.3 Doped organic semiconductors

3.3.1 Doping methods

In this section various doping methods are discussed, including bulk and contact doping, as presented in Figure 3.3. A simple way is the bulk doping method, where a controlled amount of dopant molecules is added to the organic semiconductor solution prior deposition. An important requirement for this technique is that the dopant has to be soluble in the same solvent as the host, as they are both prepared in the same solution. Bulk doping has been a successful method to enhance the device performance for several OSC systems. For example, the addition of Lewis acid $B(C_6F_5)_3$ in p-type polymers (IP-T & IP-TT) showed enhanced hole charge carrier mobility by the Lewis acid-base complex formation. [99] When a fluorinated fullerene derivative $C_{60}F_{48}$ was added to a small molecule:polymer blend solution, it resulted in effective p-type doping and an improvement in the OTFT characteristics, including the charge carrier mobility. More recently, another Lewis acid was reported, the $Zn(C_6F_5)_2$, which resulted in OTFTs with a maximum hole mobility of 20 cm^2/Vs, whereas the pristine OSCs had hole mobility of 3 cm^2/Vs. [34] A disadvantage of bulk doping is that the dopant addition may disrupt the morphology of the OSC layer and thus affect the charge carrier transport pathways. Thus morphology studies are required for the doped films in order to examine the impact of the dopant in the morphology of the organic semiconducting layer.

Contact doping is another approach, which is often employed as an interlayer between the contacts and the organic semiconducting layer. Contact doping can be either performed via thermal deposition or from solution. Several studies show that this method improves the contact resistance of the device significantly, as the dopant layer adjusts the workfunction of the metal electrode and thus the energetic barrier be-

tween them is reduced. Materials that are often used for contact doping, include SAMs with thiol groups, i.e. PFBT [101–103] and injection layers, such as $FeCl_3$. [104–107] Transition metal oxides such as MoO_3, WO_3 and V_2O_5 have also been used as injecting layers to produce high performing organic transistor devices. [108, 109]

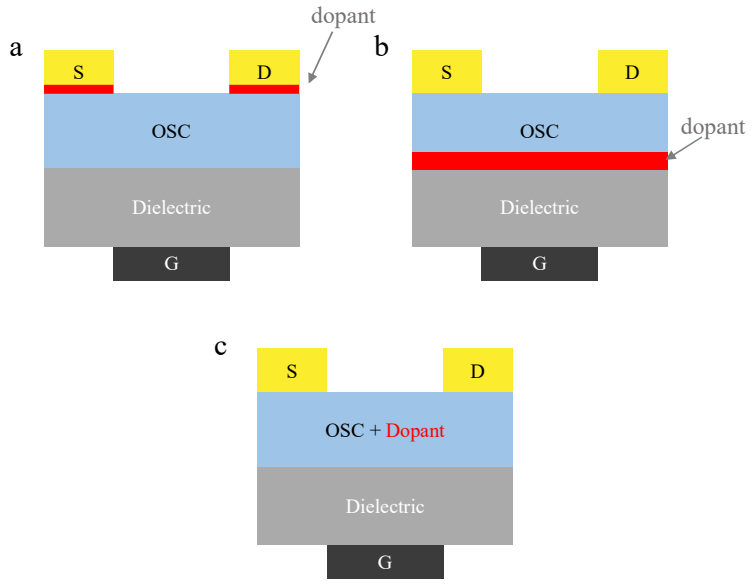


Figure 3.3: OTFTs in a BG-TC configuration showing the different doping methods for (a) contact doping, (b) doping layer and (c) bulk doping.

3.3.2 Charge carrier mobility

Molecular additives in the organic semiconducting layer of the transistor have several effects, with an important one being, the charge carrier mobility. The dopant can either be added in the organic semiconducting solution or by thermally evaporating a layer in contact with the semiconductor. As mentioned in Chapter 2.2.2 organic semiconductors have several trap states, which are detrimental for the charge transport properties of the OTFTs. Doping at low concentration fills the trap states in the organic semiconductor, resulting in pinning of the Fermi level. By increasing the doping concentration (N_A), higher than the trap density (N_T), charge carrier generation will start to occur. As such the Fermi level (E_F) shifts towards the HOMO level and at higher doping concentrations this shift will saturate. [110, 111] This mechanism is described in Figure 3.4, where it shows the shift in E_F of a p-type organic semiconductor upon doping.

Enhancement in both the linear and saturation mobility with an optimum amount of the dopant is expected. This phenomena is related to both an increase in the charge transport of the material, but also the improvement of the transistor characteristics, as a result of trap filling. Discussion the transistor's parameters follows in the next

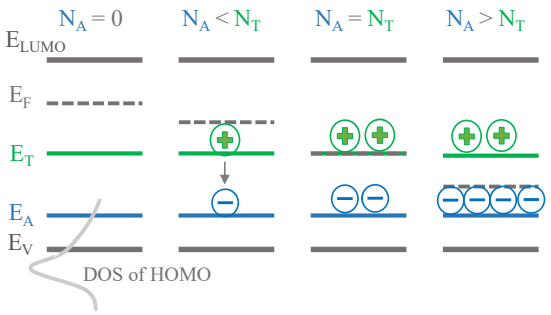


Figure 3.4: Energy level diagram showing the shift of the Fermi energy (E_F) level towards the HOMO level of a p-type organic semiconductor upon doping, where E_T is the transport energy level, E_A is the activation energy and E_v is the an effective valence band energy.

sections. Extracting the charge carrier mobility of a semiconductor from a transistor is a reliable method, but it is strongly affected by the device configuration, the metal-semiconductor interface and the semiconductor-dielectric interface and the trap states in the semiconductor.

It has also been observed that the charge carrier mobility follows a similar trend, of increasing with the dopant evolution, before it eventually saturates and then decreases. This point, where the mobility stops increasing, strongly depends on the semiconductor and the dopant and thus it varies with different systems. Several reasons behind this phenomenon include changes in the morphology of the doped film, changes in the carrier transport mechanisms at high amounts of the dopants, as well as the saturation of the shift of the Fermi level.

3.3.3 Threshold voltage and contact resistance

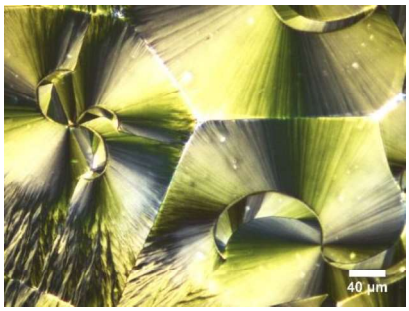
Threshold voltage (V_T) is another transistor parameter which is affected by the trap states. V_T is basically related to the voltage at which the field effect carriers will fill the trap states in the organic semiconductor. In an ideal transistor, where no traps exist, V_T should be zero. The application of V_G in a transistor should automatically switch on the device, but due to the existence of trap states, in the non-ideal case, the device turns on at higher voltages. [112] There are several ways to decrease the V_T, including device engineering and molecular doping. By filling the trap states with the dopant addition in the semiconductor, V_T shifts closer to zero. Contact resistance R_C can also be reduced with the dopant addition which, as described in Chapter 2.4.5, is affected by the energetic barrier between the metal and the semiconducting layer. For the commercialisation of OTFTs, R_C is as crucial as the charge carrier mobility of the device and thus it is important to find ways to reduce it.

3.4 Summary

In this chapter, the molecular doping of organic semiconductors is discussed, by describing the different charge transport mechanisms. Although doping is a rather old concept, it remains an interesting concept to study, since there are several parameters to consider in order to understand the charge transport behaviour. In particular, for OTFTs, doping has proven a successful technique to not only enhance the transport properties but also to improve important device parameters. The reduction in the contact resistance is one of them, where it can effectively reduce the operating voltage of the device. This is due to the fact that the molecular additive is filling the trap states in the organic semiconductor/dielectric interface.

Chapter 4

Experimental Methods



This chapter is mainly focused on the experimental procedures that were used for the work as presented in this thesis. In the first part of this chapter, a detailed description of the device fabrication is given, including the solution processing of the OSCs. The electrical characterisation is then discussed for both the OTFT and OLET devices. In the last section, a brief description of the thin film characterisation is given, in terms of the OSC morphology, energy levels and their optical properties. (Left panel: POM image of a diF-TESADT thin film)

4.1 Device fabrication

4.1.1 Substrate preparation

Glass substrates, as purchased from Instrument Glasses Ltd in dimensions 2x2 cm, were used for thin film transistor fabrication and material characterisation. Silicon substrate wafers were also used, as purchased from Active Business Company GmbH with different silicon oxide layers. Finally, quartz substrates were purchased from UQG Optics Ltd and used for optical measurements. Regardless of the type of the application, the cleaning of the substrates was the same. Substrates were sonicated for 10 minutes in the following solutions: in the beginning, substrates were sonicated in a detergent 'Decon 90' in a 20 wt% solution in deionised water, followed by sonication in deionised water to remove the detergent. Sequential sonication in isopropanol and acetone were then followed. All substrates were dried with a nitrogen blow gun. Thin film deposition and the device fabrication were performed in a glovebox (purchased from Jacomex) filled with nitrogen, of which oxygen and water levels were monitored daily.

4.1.2 Contacts deposition

For thin film transistors source-drain and gate electrodes were deposited by thermal evaporation after cleaning the glass substrates. Thermal evaporation was performed under high vacuum (10^{-6} mbar) using a Kurt J. Lesker evaporator embedded in a nitrogen filled glovebox. Metal evaporation was performed through shadow masks for source-drain and gate electrodes. The source-drain masks were designed to provide transistors with channel dimensions varying from 30 to 1000 μm. Different metals were used for source-drain (40 nm) depending on the organic semiconducting layer, including gold (as purchased from Testbourne Ltd. with 99.99% purity) and aluminium (purchased from Testbourne Ltd.). Aluminium (50 nm) was used for the gate electrode of the transistors.

For the light emitting transistors source-drain electrodes were deposited through separate masks, as different metals were used for source and drain. To achieve asymmetric electrodes for the charge injection, a 40 nm thick layer of gold was used for source, while for the drain electrode a bilayer of Cs_2CO_3/Ag (40 nm) (both purchased from Testbourne Ltd.). Finally, a 20 nm thick layer of aluminium was evaporated to form the gate electrode.

4.1.3 Contact workfunction modification

Modifying the workfunction of the evaporated metals for thin film transistors is a crucial step. The workfunction of the metal is required to be close to the organic

semiconducting layer to reduce the injection/extraction barrier, as described in Chapter 2.4.5. For p-type devices gold source-drain electrodes were treated with a self-assembled monolayer (SAM) of 2,3,4,5,6-pentafluorothiophenol (PFBT, purchased from Sigma-Aldrich), in order to decrease the workfunction of gold of about 0.8eV. PFBT on a metal surface induces strong surface dipoles, which leads to a shift in the workfunction. [72] The substrates were immersed in a 5 mM PFBT solution in isopropanol for 30 minutes. Substrates were then rinsed with clean isopropanol and dried with a nitrogen blow gun, before transferring them to a nitrogen filled glovebox for the next steps of the device fabrication.

4.1.4 Solution processing: p-type doping of OSCs

The solution preparation for the experiments, as presented in Chapter 5, are described in this section. Organic semiconducting solutions were prepared one day in advance prior to deposition, in order for the materials to become fully dissolved in anhydrous solvents. Solutions were prepared in a nitrogen filled glovebox and stirred for at least 10 hours on a magnetic hotplate. All chemicals and solvents were purchased from Sigma-Alridch, unless the supplier is stated in brackets. The materials were stored in a glovebox.

As a p-type dopant tris(pentafluorophenyl)borane [$B(C_6F_5)_3$] was applied in several small molecule and polymer transistors. The dopant was added in the organic semiconducting hosts 2 hours prior to the spin-coating deposition. The amount of the dopant to the host was calculated in mol% with respect to the organic material. For the calculation of the molar mass of the polymers, the molar mass of one repeat unit was used for the calculation. The solvent of the dopant was kept the same as the organic host for the single compound TFTs, while for the blends it was 1,2-dichlorobenzene. Table 4.1 shows the OSC concentration [C], the solvent for each solution, the dopant concentration [D], as well as the heating temperature [T_s] of the solution prion spin coating and the thin film annealing temperature [T_f] and time for the several organic semiconductors. 2,8-Difluoro-5,11-bis(triethylsilylethynyl)anthradithiophene (diF-TESADT) was supplied by Merck Chemicals Ltd, 2,7-dioctyl[1]-benzothieno[3,2-b][1]benzothiophene (C_8-BTBT) was purchased from 1-Material and 6,13-bis(triisopropylsilylethynyl) pentacene (TIPS- pentacene) were supplied by Prof. John Anthony (Department of Chemistry, University of Kentucky). The polymer indacenodithiophene-benzothiadiazole (C_{16}IDT-BT) was synthesised by Dr. Zhuping Fei and Prof. Martin Heeney (Department of Chemistry, Imperial College London) and poly(triarylamine) (PTAA) was purchased from Flexink.

For the organic semiconducting blend studies, the solutions were prepared as shown in Table 4.2. Organic semiconductors were prepared in separate solutions and they were

Table 4.1: Solution preparation for single compound p-type organic semiconductor solutions for TFTs which shows the concentration, the solvent (cb: chlorobenzene, tol: toluene), the solution heating temperature, the dopant concentration and the thin film annealing temperature in bracket.

p-type OSCs	[C] (mg/mL)	Solvent	T_s (°C)	[D] (mg/mL)	T_f (°C)
diF-TESADT	5	Cb	50	5.1	100 (10')
C_8-BTBT	2	Cb	50	0.1	100 (10')
TIPS-pentacene	5	Cb	50	5.1	100 (10')
C_{16}-IDTBT	2	Cb	50	0.1	100 (10')
PTAA	10	Tol	70	0.1	100 (10')

then added in one formulation. The blend ratio and total blend concentration [C], the solvent, the solution heating temperature [T_s], the dopant concentration [D] and the thin film annealing temperature are provided [T_f].

Table 4.2: Solution preparation for blend organic semiconductors, which shows the total concentration of the blend (the mixing ratio), the solvents (Cb is the chlorobenzene and Tet is the 1,2,3,4 tetrahydronapthalene), the solution heating temperature, the dopant concentration and the thin film annealing temperature in bracket.

OSC blend	[C] (mg/mL)	Solvent	T_s (°C)	[D] (mg/mL)	T_f (°C)
diF-TESADT:PTAA	10 (1:1)	Cb:Tet (1:1)	50	5.1	100 (15')
C_8-BTBT:C_{16}-IDTBT	10 (3:1)	Cb:Tet (1:1)	50	0.1	120 (2')
TIPS-pentacene:PTAA	10 (1:1)	Cb:Tet (1:1)	50	5.1	100 (15')

4.1.5 Solution processing: n-type doping of OSCs

For the n-type doping of organic compounds, which is studied in Chapter 6, (12a,18a)-5,6,12,12a,13,18,18a,19-Octahydro-5,6-dimethyl-13,18[1',2']benzenobisbenzimidazo [1,2-b:2',1'-d]benzo[i][2.5] (DMBI-BDZC) was used as the n-type dopant and purchased from Strem Chemicals. The dopant was used from $1x10^{-3}$M solution in chlorobenzene.

As an organic host poly[N,N9-bis(2-octyldodecyl)-naphthalene-1,4,5,8-bis (dicarboximide)-2,6-diyl]-alt-5,59-(2,29-bithiophene) P(NDI2OD-T2) (N2200) was synthesised by Dr. Simeng Wang and Prof. Martin Heeney (Department of Chemistry, Imperial College London) and the naphthalene diimides fused with 2-(1,3-dithiol-2-ylidene)malononitrile groups (NDI-DTYM2) (NDI3HU-DTYM2) small molecule was supplied by Merck KGaA. Solutions were prepared as presented in Table 4.3.

Table 4.3: Solution preparation for n-type doping of organic semiconductors, which shows the concentration of the solution, the solvent, the solution heating temperature, the dopant concentration and the thin film annealing temperature.

n-type OSCs	[C] (mg/mL)	Solvent	T_s (°C)	[D] (mg/mL)	T_f (°C)
N2200	5	P-xylene	50	0.2	150 (15')
NDI3HU-DTYM2	9.8	Mesitylene	50	1	100 (15')

4.1.6 Solution processing: OLETs

For the organic light emitting transistors (Chapter 7), poly[[6,6,12,12-tetrakis(4-hexadecylphenyl)-6,12-dihydroindeno[1,2-b]indeno[2',1':4,5] thieno[2,3-d]thiophene-2,8-diyl] thieno[3,2-b]thiophene-2,5-diyl] (PDITTTT) and 2,7-dioctyl[1]-benzothieno[3,2-b][1]benzothiophene (C_8-BTBT) were used. PDITTTT was supplied by Merck KGaA [115] and C_8-BTBT was purchased from 1-Material. Devices from single components and their blend were fabricated. The solution preparation method is presented in Table 4.4. After preparing the single component solutions, the C_8–BTBT:PDITTTT blend was mixed in a 1:3 ratio.

Table 4.4: Preparation for single compound p-type organic semiconductor solutions for TFTs, showing the concentration, the solvent (cb: chlorobenzene, tol: toluene), the solution heating temperature, the dopant concentration and the thin film annealing temperature in brackets.

OSC material	[C] (mg/mL)	Solvent	T_s (°C)	T_f (°C)
PDITTTT	10	Tet	50	100 (15')
C_8-BTBT	10	Cb	50	100 (15')
		For the OSC blend		
PDITTTT	15	Tet	50	120 (15')
C_8-BTBT	20	Cb	50	120 (15')

4.1.7 Organic thin film deposition

After treating the source-drain contacts, the organic semiconductors were deposited via spin coating followed by thermal annealing. Organic thin films in this project for device fabrication and characterisation were prepared by spin coating in a nitrogen filled glovebox. Spin coating is a widely used technique for depositing solution processed materials. The solution is dropped onto the surface and the thin film is formed by spinning the substrate as shown in Figure 4.1. By spinning of the substrate, excess solution of the material is spun off due to centrifugal forces. The solvent evaporates

during spinning. The amount of the evaporated solvent depends on the spin speed and duration, as well as the boiling point of the solvent and the viscosity of the solution.

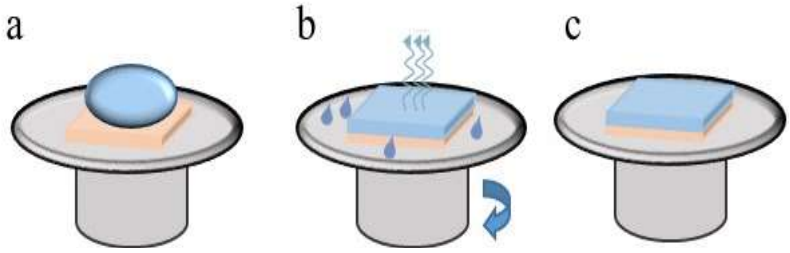


Figure 4.1: Steps of the spin coating technique: (a) Solution (blue) is dropped onto the substrate. (b) Spin of the substrate spreads the solution and excess is spun off due to centrifugal forces while solvent is evaporating. (c) The thin film is produced.

The spinning conditions for the solutions used in this project varied depending on the solvent used and the organic semiconducting material. For the organic semiconducting blends. A two-step spin coating procedure was applied starting at 500 rpm for 10 seconds followed by 2000 rpm for 30 seconds with acceleration 9 (9 is the slowest speed increment). For the single component organic semiconductors, the spin speed was 2000 rpm for 30 seconds. All organic semiconducting thin films were then annealed at different temperatures. When thin film transistors were fabricated, the gate dielectric layer was spin coated after the organic semiconductor layer. CYTOP (as purchased from AGC Chemicals) was used as the gate dielectric without further processing. As it is a viscous solution, prolonged spin time was used; 2000 rpm for 60 seconds resulting in a film of 900 nm thickness (with geometric capacitance 2.1 nF/cm^2). The gate dielectric was thermal annealed at 100°C for 1 hour. Poly(methyl methacrylate) (PMMA) was used as the gate dielectric for the N2200 OTFTs of Chapter 6. PMMA was spin coated from 80 mg/ml solution in butyl acetate at 2000 rpm for 60 seconds producing a film of 560 nm thickness (with geometric capacitance 5.5 nF/cm^2).

4.2 Electrical Characterisation

Data analysis was performed using the following programs: Origin, Matlab and Python.

4.2.1 Current - voltage measurements

The transfer and output curves of the thin film transistor devices were measured with an Agilent B2902A semiconductor parameter analyser (SPA) in combination with a probe station in a nitrogen filled glovebox. The SPA has several source measurement

units (SMUs), which were connected to the terminals of the transistors. A set of micro-positioning needles were used to make contacts with the device's electrodes with the help of a camera.

4.2.2 Low - temperature measurements

For the low-temperature current-voltage measurements a cryogenic probe station (Figure 4.2) (Janis ST-500) was connected to an Agilent B2902A. The chamber of the probe station cooled down with liquid nitrogen to 73 K in high vacuum ($\sim 10^{-5}$ mbar). Transistor characteristics were measured in a range of temperatures starting from 73-310 K with an increment of 10 K. A script as written in Autohotkey was used to control the measurements to make sure that the difference in temperature from the two embedded sensors in the chamber for each measurement was kept constant.

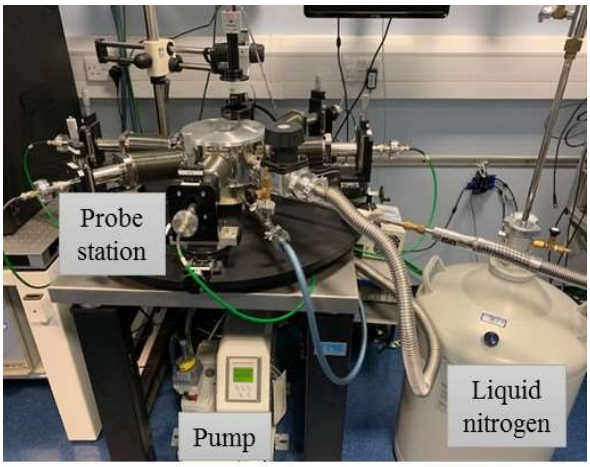


Figure 4.2: Experimental set-up of the low temperature system used to measure TFTs with a cryogenic probe station.

4.2.3 Brightness measurements

The device luminance for the OLETs were evaluated from the photodiode current. The photodiode current was initially calibrated with an organic light emitting diode (OLED) by using a luminance meter (Konica Minolta LS-100). The calibration of the photomultiplier tube was performed with a super-yellow (SY) based OLED with a known area and brightness (Figure 4.3). The controlled SY OLED had a photocurrent of 71 nA per cd m^{-2} with an area of 0.92 mm^2.

These measurements and data analysis, as presented in Chapter 7, were performed by Dr. Mujeeb Ullah Chaudhry at Durham University.

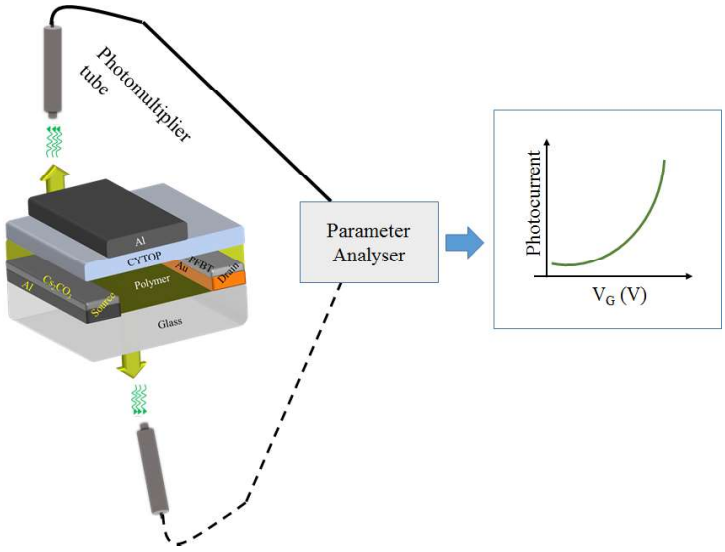


Figure 4.3: Experimental set up of the spectrometer used to determine the evolution of the brightness of the OLETs. The photomultiplier tube converts the light detected by the photodetector.

4.2.4 External Quantum Efficiency

The external quantum efficiency (EQE) is an important parameter for the OLET devices, as it quantifies their efficiency. EQE is defined as the ratio of the generated photons per number of injected photons. This parameter can be extracted from the current-voltage (transfer curve) of the OLET. Assuming a Lambertian emission, where the radiation is directly proportional to the cosine of the angle (θ) formed between the surface and the incident light. Thus, the total luminous flux Φ_v can be calculated as Equation 4.1 shows

$$\Phi_v = 2\pi I_o \int_0^{\pi/2} cos\theta sin\theta d\theta \tag{4.1}$$

where I_o is the luminance (cd m^{-2}) of the emission. By simplifying Equation 4.1, the luminous flux (Equation 4.2)

$$\Phi_v = \pi I_o A \tag{4.2}$$

where A is the area of the emission zone of the device and thus the units of Φv are (cd sr). A human eye response curve was used to weight all the spectral components of the measured light. The curve has a sensitivity peak at 555 nm and flux of 683 lm/W. Thus the power and the measured flux can be related, as Equation 4.3 describes,

$$\Phi_v = 683 Power \frac{\int ER(\lambda) El(\lambda) d\lambda}{\int El(\lambda) d\lambda} \tag{4.3}$$

where ER is the eye response curve and El is the area under the electroluminescence

curve. Then the number of the emitted photons (n) can be calculated as Equation 4.4 shows,

$$E = \frac{nhc}{\lambda} \tag{4.4}$$

where h is Planck's constant, c is the speed of light and λ is the wavelength of the light being measured. Since different wavelengths were used, the calculation of the centroid wavelength λ_c was required:

$$\lambda_c = \frac{\int El(\lambda)d\lambda}{\int El(\lambda)d\lambda} \tag{4.5}$$

and thus the number of emitted photons (n_{ph}) per second is:

$$n_{ph} = Power\frac{\int El(\lambda)d\lambda}{\int El(\lambda)d\lambda}\frac{1}{hc} \tag{4.6}$$

By dividing the drain current by the fundamental charge the number of injected electrons per second can be calculated. Finally, EQE is the ratio of the number of photons emitted from the device divided by the number of electrons injected into the device. The EQE analysis (Chapter 7) was performed by Dr. Mujeeb Ullah Chaudhry at Durham University.

4.3 Thin film characterisation

4.3.1 Polarised optical microscopy

Polarised optical microscopy (POM) was used in this thesis to evaluate the thin film's morphology. Information such as thin film uniformity and crystallinity of the films can easily be examined. By combining the images with the open source software ImageJ, the crystalline domains of the films can be observed. This technique was also used to measure the transistor channel's dimensions.

The polarised optical microscope is based on the birefringence of asymmetrically ordered materials, which in this case are the organic semiconductors. When a beam of light is incident on a birefringent medium it splits in to ordinary and extraordinary beams (perpendicularly polarised), as shown in Figure 4.4. Whilst these beams travel through the medium they interact with the refractive index of the crystal and due to their difference in speed they exit the crystal out-of-phase. A polarising filter is placed before the birefringent medium so that only two polarisations can pass through. A second polarising filter (analyser) perpendicular to first one is used to combine these two beams. In order for the light to pass through, the cross-polarisers have to change its polarisation. An interference pattern is then created due to the phase difference between the ordinary and extraordinary beams.

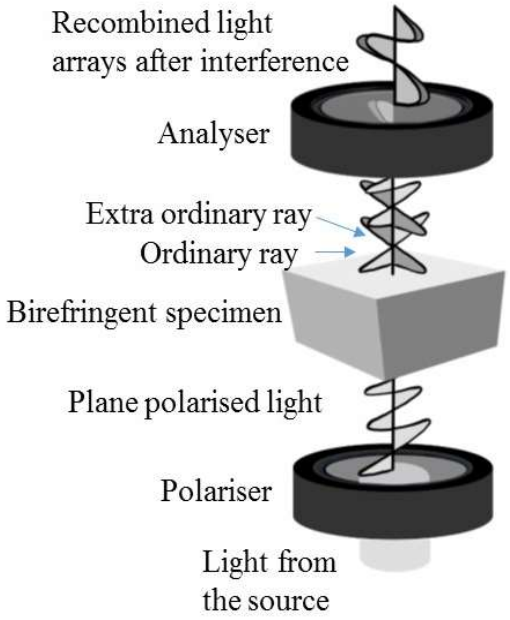


Figure 4.4: Schematic configuration of a polarised light microscope.

The polarised optical microscope used in this work was a Nikon LV 100, equipped with 5-50x magnification lenses connected to a CCD camera for capturing the images.

4.3.2 Atomic Force Microscopy

Atomic force microscopy (AFM) is a powerful technique for morphological characterisation of thin films. A helium-neon laser radiates the tip which is on a cantilever and a photodiode detects the deflection in case of the topography. The sample is placed on a piezoelectric tube where with the feedback loop constructs the topography image. The schematic set-up is shown in Figure 4.5.

The scanning windows can vary between 0.5x0.5 μm (HR-AFM) to 50x50 μm depending on the desired resolution and scanning area. There are various scanning modes available, but for organic materials it is common to use the tapping mode. This is a non-contact scanning method, where the cantilever oscillates on top of the sample surface. Information such as the topography, the amplitude and the phase of the sample can be recorded. By further data analysis, the film roughness, the height distribution and analysis of the crystalline layers can be obtained.

In this work, an Agilent 5500 AFM was used under an ambient environment with a silicon tip with resonant frequency 300 kHz and force constant 40 N/m (purchased from Budget Sensors). Data analysis was performed with Gwyddion.

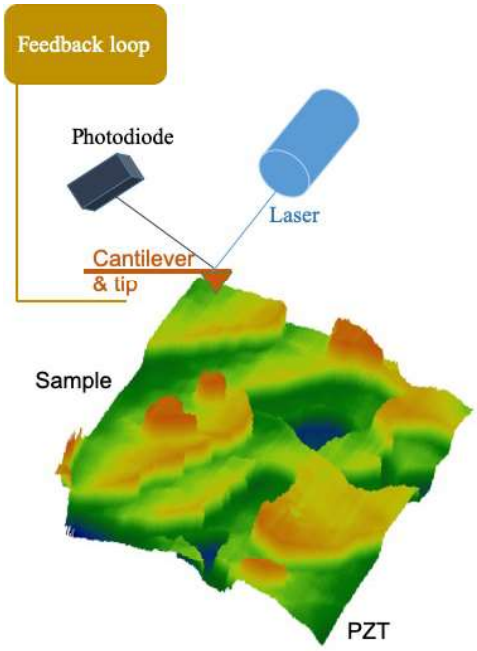


Figure 4.5: Cartoon schematic of the AFM system. A laser beam is irradiating the tip and the photodiode detects the signal which then via the feedback loop and the piezoelectric tube (PZT) converts the signal to image. The sample in this figure is an n-type organic small molecule in 3D which it was used in this work.

4.3.3 X-Ray Diffraction

X-Ray diffraction is a common technique used to identify the crystallinity and the material's structure. X-Rays are generated in a cathode ray tube by heating a filament to produce electrons. By applying a voltage, electrons are accelerated towards the target sample. Only when the electrons have enough energy to remove an electron from the inner shell can X-ray spectra be produced.

As presented in Figure 4.6 the scattered rays from the crystal can interfere either constructively or destructively. The detector only collects the signal when constructive interference occurs. Constructive interference only occurs if the path difference (2d sinθ) is a multiple of the wavelength of the X-Ray beam, according to Bragg equation (nλ=2d sinθ).

For the p-type doping and light emitting transistor's materials analysis (Chapters 5&7), XRD measurements were conducted by Panos Patsalas and George Vourlias, (Department of Physics, Aristotle University of Thessaloniki, Greece), using a Rigaky Ultima diffractometer equipped with a copper anode was used. Thin film organic semiconductors were deposited on heavily doped Si^{++} substrates.

For the n-type project (Chapter 6) XRD measurements were performed by Jaspreet Kainth and Dr. Martyn McLachlan (Department of Materials, Imperial College London, U.K). A PANanalytical X'Pert Pro MPD with a copper anode was used. Samples

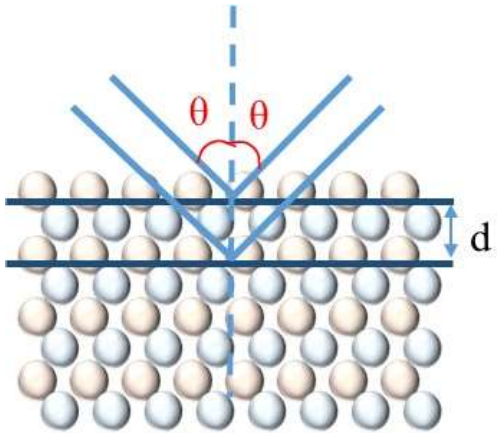


Figure 4.6: Schematic representation of Bragg's law.

were prepared on a glass substrate.

4.3.4 Kelvin Probe & Air Photoemission Spectroscopy

A combination of Kelvin Probe (KP) and Air Photoemission Spectroscopy (APS) are valuable analytical tools for metals and semiconductors, as their energy levels can be determined. KP measures the potential difference between the vibrating tip and a conductive grounded sample. The tip vibrates 0.2-2 mm away from the sample surface and an electrical contact between them is made. A parallel-plate geometry capacitor is formed between the tip and the sample. Due to the electrical contact, the Fermi level of the tip and sample align resulting in charge flow. Surface potential is then determined by the charge flow. KP is a non-contact and non-destructive way to measure the surface potential of the topmost 1-3 layers of atoms of the sample.

APS is used to measure the absolute work function (valence band) of the semiconductor by photoemission in air. An incident light with excitation range 3.3 to 6.8 eV is used and it is based on the photoelectric effect. By varying the energy of the incident light, the absolute work function can be measured. The HOMO energy level of the organic semiconductor was extracted by applying Fowler's analysis on the cube root of the photoelectron versus incident photon energy. [113]

In this work a KP Technology Kelvin Probe SKP5050/APS02 system was used to measure the work function of the pristine and doped organic semiconductors as well as the work function of the evaporated metals. Silver was used as reference sample and the incident light for the APS measurement was scanning from 6 to 4 eV, recording the photocurrent response in a nitrogen filled chamber.

4.3.5 Electron Paramagnetic Resonance

Electron paramagnetic resonance (EPR) or electron spin resonance (ESR) is a spectroscopic technique which detects unpaired electrons. An external magnetic field is applied, and the paramagnetic electrons could either orient parallel to the field direction or antiparallel. Two very distinct energy levels are created for the unpaired electrons, which allow us to measure them. In this project, EPR was used to explore whether the molecular additives had generated unpaired electrons.

The EPR results, as presented in Chapter 6, were measured by Abdul – Hamid Emwas and Dr. Alexandra F. Paterson (King Abdullah University of Science and Technology (KAUST), Saudi Arabia). OSCs were deposited via drop casting on glass substrates. The EPR was measured using a 5 G modulation amplitude, 100 kHz modulation frequency and 25 dB microwave attenuation. All spectra were measured at low temperatures, which were achieved using liquid helium (∼4 K). A Bruker x-band continuous wave EMX PLUS spectrometer was used to record all the EPR spectra, where the latter was operated at (9.384688) GHz with a standard resonator, CW-EPR, allowing for high sensitivity signal detection.

4.4 Optical properties of thin films and devices

4.4.1 Ultraviolet-visible-near infrared absorption spectroscopy (UV-Vis-NIR)

UV-Vis-NIR spectroscopy technique is often used to study the optical properties of organic semiconductor materials. Thin films were deposited on quartz substrates by spin coating. A beam of monochromatic light passes through the sample and the transmittance in percentage can be measured. Quartz substrates were used as the reference sample. The absorption results, as presented in Chapter 7, were measured by Alice Smith (Oxford University, U.K.) using a Shimadzu UV-2600.

4.4.2 Electroluminescence and Photoluminescence

In the electroluminescence measurements the applied field is responsible for charge recombination and light emission, whereas in photoluminescence measurements the excitation of charges is via light. The electroluminescence (El) and photoluminescence (Pl) of the light emitting transistors were measured using an optical fibre coupled (Ocean-Optics USB4000-XR) spectrometer. The experimental results, as presented in Chapter 7. Dr. Mujeeb Ullah Chaudhry performed the EQE measurements and data analysis in Durham University.

4.4.3 Steady state and time-resolved PL & solid-state photoluminescence quantum efficiency (PLQE)

The time-resolved PL measurements provide useful information to understand the recombination mechanism, as the PL intensity is monitored over time (nanoseconds). These measurements were performed by Dr. Sungho Nam (Oxford University, U.K.), using a time correlated single photon counting apparatus (FluoTime 300, PicoQuant GmbH). Thin films were deposited on quartz substrates which were excited with a frequency of 10 MHz using a 405 nm pulsed laser head (detection wavelength 537 nm). The instrument response function (IRF) was also considered for the calculation of delay times. A biexponetial fit was used to extract the decay parameters for the samples. The data analysis is presented in Chapter 7.

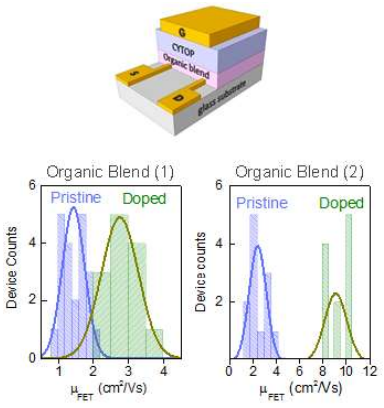
Solid-state photoluminescence quantum efficiency (PLQE) measurements were performed in thin films and are presented in Chapter 7. Alice Smith (Oxford University, U.K.) conducted the measurements using a Horiba Scientific FloroMax-4 Spectrophotometer and Horiba Scientific Quantum-ϕ Integrating Sphere. Directly and indirectly excited emission spectra were recorded for the thin films at a slit width of 0.9 nm. The PLQE was then calculated using the de Mello method [114], with the Jacobian correction applied to all wavelength/energy spectral conversions. [115]

4.5 Summary

In this chapter the experimental techniques, as used for the work in this thesis are presented in detail. In the first section the device fabrication is described, including thin film deposition and metal evaporation. Then the OSC and doping solutions are listed for the result chapters separately. The electrical characterisation (I-V) of the thin film transistors then follows. Lastly, the thin film characterisation is discussed including POM, AFM, XRD and KP and APS, as well as the techniques to understand the optical properties of the thin films.

Chapter 5

P-type Doping OTFTs



This chapter describes a simple method for enhancing the charge transport properties of several organic semiconducting systems including p-type small molecules, polymers and their blends. This method is based on admixing the Lewis acid $B(C_6F_5)_3$ in the semiconductor formulation. In two organic semiconducting blended systems $B(C_6F_5)_3$ showed a remarkable improvement in the hole charge carrier mobility; for blends of 2,8-difluoro 5,11-triethylsilylethynyl anthradithiophene: poly(triarylamine) (diF-TESADT:PTAA), and 2,7-dioctyl[1]-benzothieno[3,2-b][1] benzothiophene: indacenodithiophene-benzothiadiazole (C_8-BTBT: C_{16}-IDTBT), hole mobilities of 8 and 11 cm^2/Vs, respectively were obtained from OTFTs. From further analysis of the single and blend materials $B(C_6F_5)_3$ revealed that it has a dual role: an effective p-type dopant and a microstructural modifier in the organic layer of the device.

5.1 Introduction

In the field of organic electronics the continuous demand for high performing organic thin film transistors (OTFTs) has been the driving force behind the tremendous progress witnessed during the past decade. New synthetic routes have been explored leading to new materials with enhanced charge transport properties. [34, 42] Another approach to enhance charge transport in organic semiconductors and improve the overall OTFT performance, is by the addition of molecular dopants. [57, 116] In this chapter, the addition of Lewis acid molecules in several p-type organic semiconductor blends is investigated. OTFTs were studied from both pristine and doped organic semiconductors with the Lewis acid. Further analysis on the morphology of the thin films were obtained by several techniques.

5.2 Organic Semiconducting Blends

In this chapter, the impact of the Lewis acid $B(C_6F_5)_3$ in several organic semiconducting blends was investigated. Blending a small molecule and a polymeric material is a common approach to achieve high film uniformity and good charge transport properties. It has been shown that when blending 2,8-difluoro-5,11-bis(triethylsilylethynyl) anthradithiophene (diF-TESADT) with poly(triarylamine) (PTAA) the charge carrier mobility increases to 2.4 cm^2/Vs, of which structures are presented in Figure 5.1a. [55] By further analysis of the organic compounds the system tends to undergo vertical phase separation with the first 15-25 nm consisting of diF-TESADT. [55, 61, 117, 118] The same behaviour was observed when 6,13-bis(triisopropylsilylethynyl) pentacene (TIPS-pentacene) TIPS-pen:PTAA and 2,7-dioctyl[1]- benzothieno[3,2-b][1]benzothiophene (C_8-BTBT) and the indacenodithiophene - benzothiadiazole (C_{16}IDT-BT) are blended. [55, 57] The charge carrier mobility values of several organic blend systems are presented in Table 5.2.1 as measured in BC-TG OTFTs configuration. Further information on the solution processing and device fabrication can be found in Chapter 4.

Table 5.1: Hole charge carrier mobility of pristine organic semiconducting blend systems as measured in this project.

OSC blend	Hole mobility (cm^2/Vs)
diF-TESADT:PTAA	2.4
TIPS-Pentacene:PTAA	1.1
C_8-BTBT:C_{16}IDT-BT	2.5

With reference to the organic semiconductor blends, as presented in Table 5.1, the

effect of the Lewis acid tris(pentafluorophenyl) borane $B(C_6F_5)_3$ when added in the organic blend formulations was studied in terms of charge transport properties and thin film morphology.

5.3 Doping Mechanism

As described in Chapter 3, there are several mechanisms explaining the doping procedure in organic semiconductors. A range of techniques was used to extract the energy levels of the OSC, including density functional theory (DFT) calculations, cyclic voltammetry measurements, Kelvin Probe (KP) and Air Photoemission Spectroscopy (APS) technique.

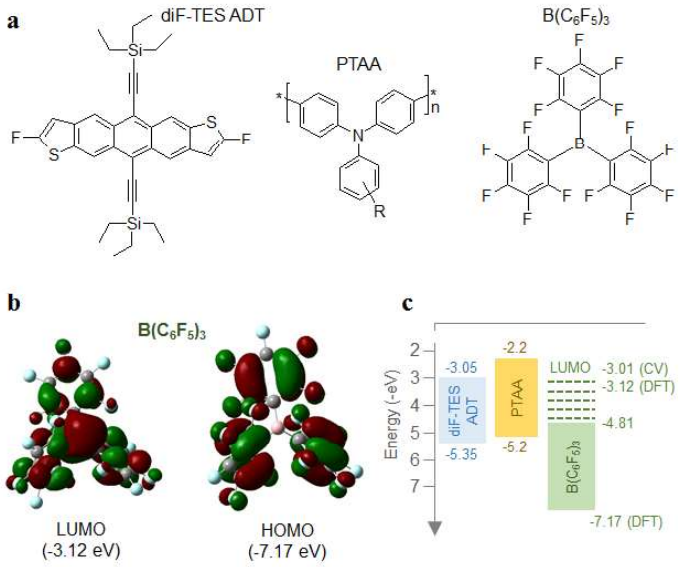


Figure 5.1: (a) Chemical structures of diF-TESADT, PTAA and $B(C_6F_5)_3$. (b) LUMO and HOMO energies for $B(C_6F_5)_3$ calculated via the DFT method. The HOMO is predicted to be localised on phenyl groups whilst the LUMO is delocalised over the whole molecule. (c) HOMO and LUMO energies of diF-TESADT, PTAA and $B(C_6F_5)_3$.

The chemical structures of the first organic semiconducting blend system included the diF-TESADT as a small molecule and the PTAA as the polymer are presented in Figure 5.1a, along with the structure of the dopant $B(C_6F_5)_3$. Density functional theory (DFT) calculations for the $B(C_6F_5)_3$ showed that the highest occupied molecular orbital (HOMO) is at -7.17 eV, whereas the lowest unoccupied molecular orbital (LUMO) is at -3.12 eV (Figure 5.1b). Figure 5.1c presents the energy levels of the organic materials, and as it can be seen, a large energy offset is observed between the dopant and the host from CV and DFT studies. Although the latter picture may appear to rule out ground state integer electron transfer from the blend to the $B(C_6F_5)_3$, a recent study suggests that such a process is possible since they reported the LUMO energy level of

$B(C_6F_5)_3$ at -4.81 eV. However, the way that they measured or calculated this value is not stated [120]. The LUMO energy value for $B(C_6F_5)_3$ of -3.01 eV was measured by CV as taken from reference [119].

An alternative proposed mechanism for this doped system, is the Lewis acid-base interactions between certain chemical species and the dopant. Integer electron transfer may occur from the organic semiconductors to the $B(C_6F_5)_3$, resulting in a formation of radical cations and thus p-type doping of the organic hosts.

5.4 p-Type Thin Film Transistors

In order to evaluate the p-type doping hypothesis bottom-contact top-gate (BC-TG) organic thin film transistors (OTFTs) were fabricated, where structure and an array of OTFTs are presented in Figure 5.2. The contacts of the devices were deposited via thermal evaporation of gold and aluminium metals under high vacuum. For the organic semiconductor and the dielectric deposition, spin-coating was used. Further details on the experimental procedure can be found in Chapter 4.

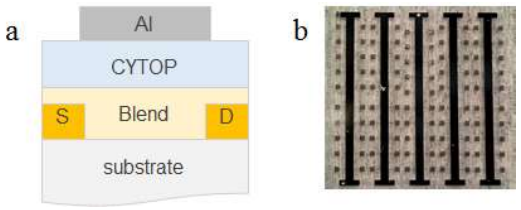


Figure 5.2: Bottom-contact top-gate (BC-TG) thin film transistor a) device architecture and b) array of fabricated OTFTs on a glass substrate.

5.4.1 Organic Semiconductor Blends

As the organic semiconductor layer, the diF-TESADT:PTAA blend was used, of which transfer curves are presented in Figure 5.3 with the green line (0 mol%). Introducing molecules of $B(C_6F_5)_3$ in the organic semiconducting blend affects the transfer characteristics (Figure 5.3a), where a clear increase in the on-current (I_{ON}) is observed by adding 1.5 and 2.4 mol%. The increase of the (I_{ON}) is more pronounced in the square root of the drain (I_D) current vs the gate voltage (V_G) plot, Figure 5.3b. Moreover, the off-current (I_{OFF}) is also increased when molecules of $B(C_6F_5)_3$, were added in the diF-TESADT:PTAA blend. This phenomenon has been observed in other doped semiconducting systems and it is attributed to the increased bulk conductivity, which is due to the increased concentration of free charges in the semiconducting layer. [121]

Representative output curves (I_D vs V_D) of the best performance devices for diF-TESADT:PTAA and diF-TESADT:PTAA: $B(C_6F_5)_3$ (2.4 mol%) are presented in Fig-

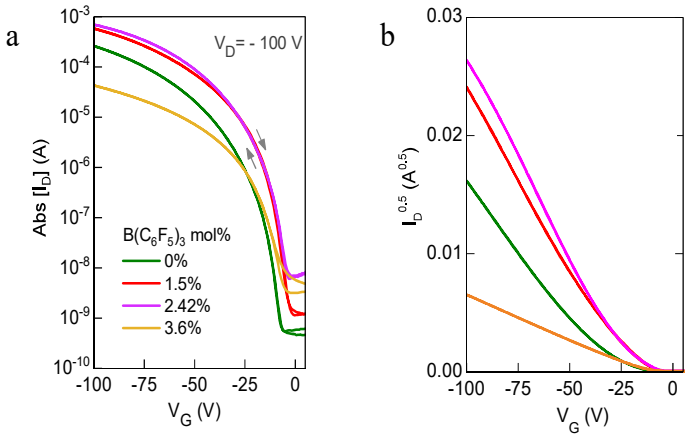


Figure 5.3: Transfer characteristics as measured for top-gate, bottom-contact diF-TESADT:PTAA transistors with different $B(C_6F_5)_3$ concentrations in the range of 0-3.6 mol%.

ure 5.4. The increase in the I_D is more obvious in the output curves. Minimal hysteresis is also observed in these OTFTs, indicating a good quality semiconductor/dielectric interface.

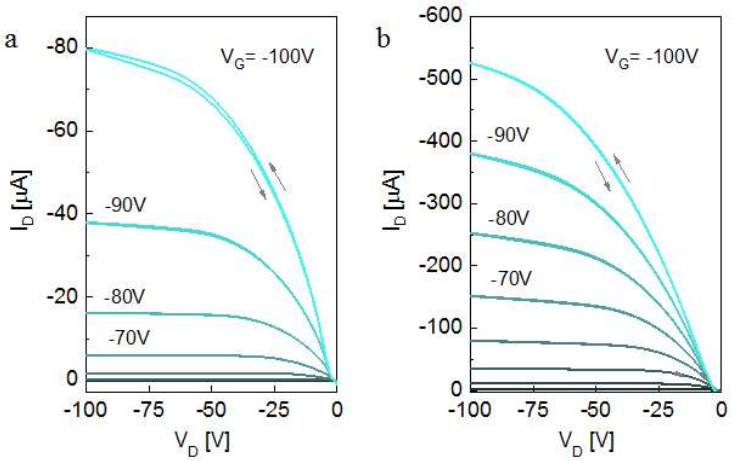


Figure 5.4: Output characteristics (I_D vs V_D) for the organic semiconducting blend (a) diF-TESADT:PTAA and (b) diF-TESADT:PTAA:$B(C_6F_5)_3$ (2.4 mol%)

By further analysis of the transistor's characteristics the field effect mobility was extracted by using the equations as described in Chapter 2.4 for both linear and saturation regime. Pristine (0 mol%) TFTs exhibit hole charge carrier mobility on average in the saturation regime ($\mu_{h\,(SAT)}$) of 2 cm^2/Vs, as presented in Figure 5.5a. By admixing the $B(C_6F_5)_3$ in the organic semiconducting blend an increase in both linear ($\mu_{h\,(LIN)}$) and saturation regime is observed. The highest hole mobility of ~8

cm^2/Vs in the saturation regime was found when 2.4 mol% of $B(C_6F_5)_3$ was added in the diF-TESADT:PTAA blend. This value is higher than reported for single-crystal diF-TESADT OTFTs ($6cm^2$/Vs). [49] For OTFT applications, parameters such as threshold voltage (V_{Th}), on-off current ratio $I_{ON/OFF}$ and contact resistance (R_C) are crucial. Figure 5.5b shows the evolution of the V_{Th} by varying the mol% concentration of $B(C_6F_5)_3$ in the diF-TESADT:PTAA blend. A sharp decrease in the V_{Th} is observed once $B(C_6F_5)_3$ was added up to 1 mol%, which then remains at relatively constant voltages. Increasing $B(C_6F_5)_3$ concentration to >2.4 mol% results in an increase in the channel off-current and on/off ratio deterioration, as presented in Figure 5.5c. A further positive effect associated with the presence of $B(C_6F_5)_3$, is the reduction of the contact resistance (R_C). Figure 5.5d shows the evolution of R_C for pristine and $B(C_6F_5)_3$-doped (2.4 mol%) OTFTs as calculated using the transmission line method (TLM). [122] Although the dependence of R_C on V_G for the pristine and doped devices appears similar, $B(C_6F_5)_3$-doped OTFTs exhibit significantly reduced R_C. This is an important finding and highlights the important role of R_C on the mobility enhancement observed (Figure 5.5a) while indirectly supports the p-doping effect, as the trap states in the semiconducting layer have been filled by the dopant.

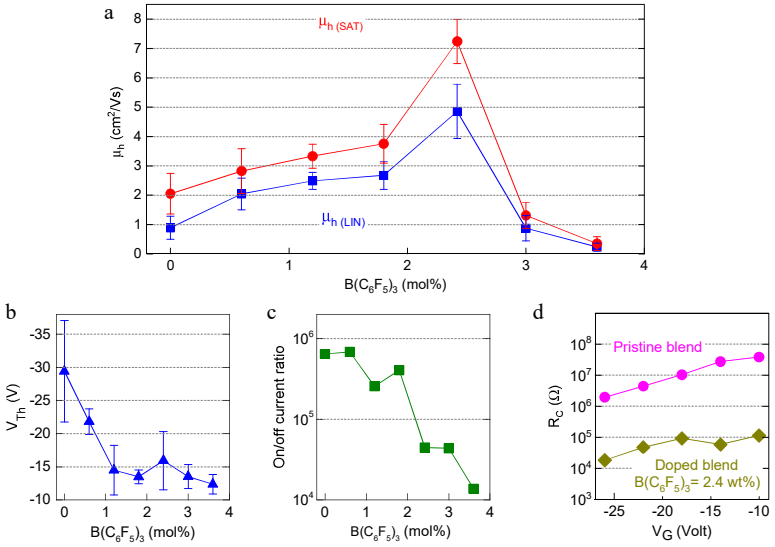


Figure 5.5: (a) Evolution of hole mobility (μ_h) as a function of $B(C_6F_5)_3$ concentration for the diF-TESADT:PTAA: $B(C_6F_5)_3$ blend. (b) & (c) display the evolution of threshold voltage (V_{Th}) and current on-off ratio, respectively, as a function of $B(C_6F_5)_3$ concentration and (d) evolution of contact resistance (R_C) versus V_G calculated for the pristine and $B(C_6F_5)_3$ (2.4 mol%)-doped diF-TESADT:PTAA OTFTs.

To investigate whether the Lewis acid doping approach is applicable to other organic semiconductors the study was extended to two other already known organic semiconducting blend systems in the literature: 6,13-bis(triisopropylsilylethynyl) pentacene (TIPS- pentacene) with poly(triarylamine) (PTAA), TIPS-pen:PTAA and the

small molecule 2,7-dioctyl[1]- benzothieno[3,2-b][1]benzothiophene (C_8-BTBT) with the indacenodithiophene- benzothiadiazole polymer (C_{16}IDT-BT), C_8-BTBT:C_{16}IDT-BT. TIPS-pen as well as C_8-BTBT are highly crystalline small molecules with good charge transport properties. The chemical structures of the compounds as well as their HOMO energy levels are presented in Figure 5.6. The HOMO energy level of the semiconductors was measured via Air Photoemission Spectroscopy (APS).

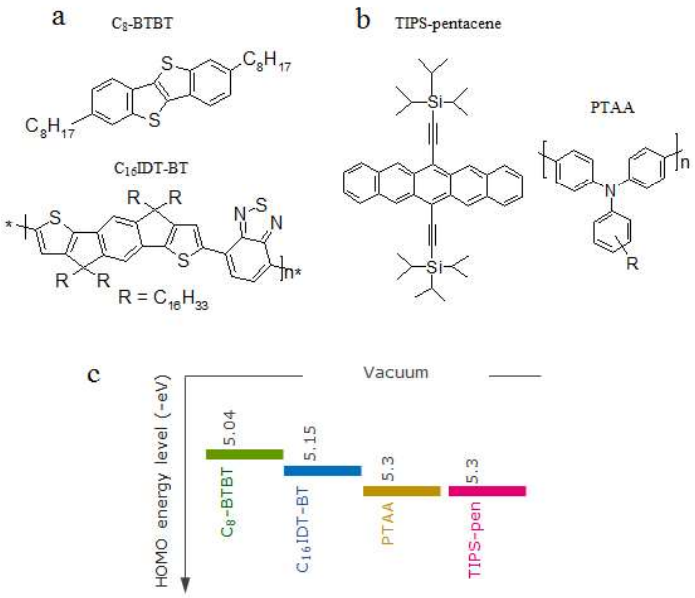


Figure 5.6: (a, b) Chemical structures of the additional organic semiconducting materials used for blends and (c) their HOMO energy level, as measured by APS.

The conditions for blending these materials were by as described in Chapter 4. The dopant was used in the range of 0-0.5 mol% for the C_8-BTBT:C_{16}IDT-BT blend and in the range of 0-5 mol% for TIPS-pen:PTAA, in order to find the optimum dopant concentration where the OTFTs showed the best performance. Figure 5.7 shows representative transfer characteristics of the pristine (0 mol%) blends and OTFTs with the optimum amount of $B(C_6F_5)_3$ in each system. For the OTFTs with the C_8-BTBT:C_{16}IDT-BT, the optimum amount of $B(C_6F_5)_3$ was found when 0.05 mol% were added, while for the TIPS-pen:PTAA blend at 2.4 mol%. For the C_8-BTBT:C_{16}IDT-BT blend OTFTs, the enhance in the I_{ON} is significant, since from 4.7×10^{-5} increases to 2.2×10^{-4}A for the 0.05 mol% $B(C_6F_5)_3$-doped, whereas in the TIPS-pen:PTAA it was less pronounced.

The hole charge carrier mobility was extracted from several devices for each blend by following the gradual channel approximation equations, as presented in the histograms of Figure 5.8. Pristine C_8-BTBT:C_{16}IDT-BT OTFTs show charge carrier mobility in the saturation regime in the range of 1-4 cm^2/Vs, which is in accordance with reported values for this particular organic semiconducting blend. [57] Addition of only 0.05

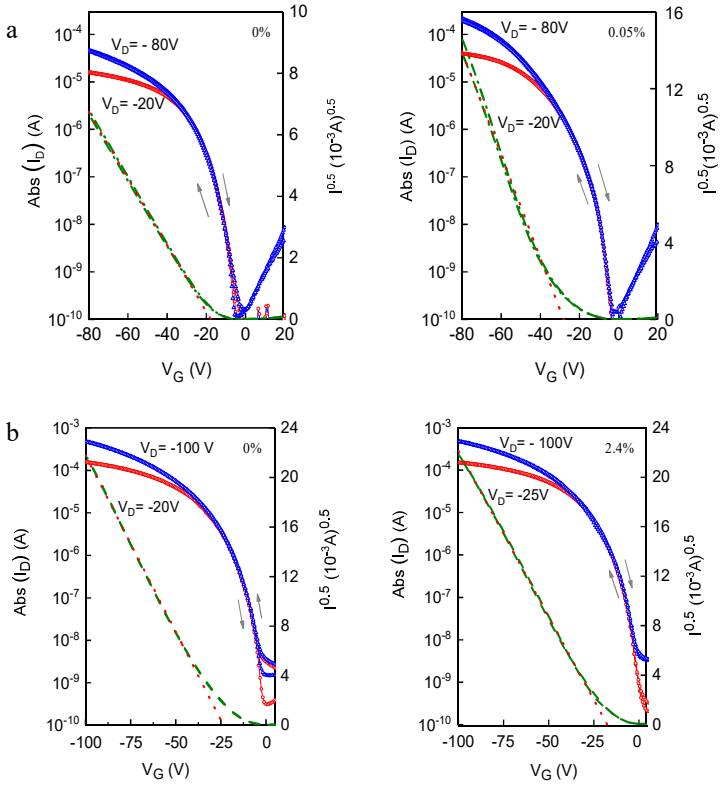


Figure 5.7: Transfer characteristics measured for top-gate, bottom-contact (a) C_8-BTBT:C_{16}IDT-BT and (b) TIPS-pen:PTAA blends.

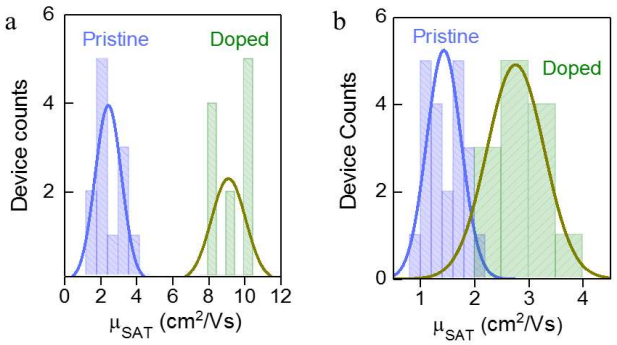


Figure 5.8: Histograms of saturation mobility for (a) pristine C_8-BTBT:C_{16}IDT-BT:$B(C_6F_5)_3$ (0 mol%) and doped C_8-BTBT:C_{16}IDT-BT:$B(C_6F_5)_3$ (0.05 mol%) and (b) pristine TIPS-pen:PTAA: $B(C_6F_5)_3$(0 mol%) and doped TIPS-pen:PTAA: $B(C_6F_5)_3$ (2.4 mol%).

mol% $B(C_6F_5)_3$ led to a significant improvement in the hole transport with values now reaching ~11 cm^2/Vs. A similar but less pronounced effect is observed for the TIPS-pen:PTAA blend, which upon doping with 2.4 mol% demonstrates charge carrier mobility of ~3.7 cm^2/Vs.

Overall, a positive impact is observed in hole charge transport properties of the organic semiconductor blends when admixing them with $B(C_6F_5)_3$. Not only is the charge carrier mobility enhanced, but other important parameters for OTFTs are improved, such as the decrease of the V_{Th} and the reduction of the R_C upon doping.

5.4.2 Single component TFTs

To further explore the impact of $B(C_6F_5)_3$ in the organic semiconducting materials used for the OSC blend OTFTs, OTFTs from single OSCs were fabricated. The purpose of this experiment was to understand whether $B(C_6F_5)_3$ has higher impact in the small molecules, the polymers or in both materials. For this reason, BC-TG OTFTs were fabricated from the small molecules diF-TESADT, C_8-BTBT and TIPS-pent, as well as from the polymers PTAA and C_{16}IDT-BT. Experimental details of the solution preparation and the device fabrication are described in Chapter 4.

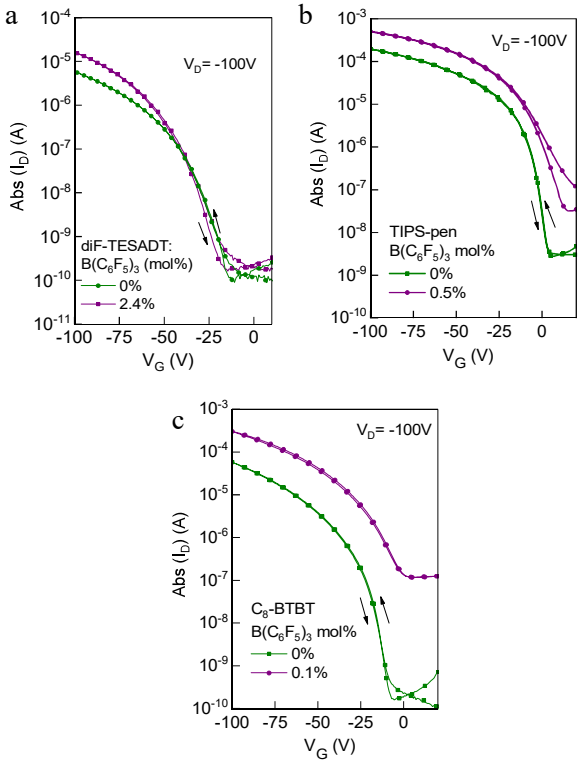


Figure 5.9: Transfer characteristics for the small molecule OTFTs with (a) diF-TESADT:$B(C_6F_5)_3$ 0 mol% & 2.4 mol%, (b) TIPS-pen:$B(C_6F_5)_3$ 0 mol% & 0.5 mol% and (c) C_8-BTBT:$B(C_6F_5)_3$ 0 mol% & 0.1 mol%.

Figure 5.9a shows the transfer characteristics of the small molecule diF-TESADT pristine (0 mol%) and doped diF-TESADT:$B(C_6F_5)_3$ (2.4 mol%) OTFTs. An increase in the I_{ON} is observed when the dopant is added, which led to an increase in the hole

charge carrier mobility from 0.5 to 1 cm^2/Vs for the linear and from 1 cm^2/Vs to 1.7 cm^2/Vs for the saturation regime. A small decrease in the threshold voltage is also observed of ∼5 V, which is attributed to trap filling caused by the dopant addition. Tips-pen:$B(C_6F_5)_3$ showed a similar behaviour when 0.5 mol% of $B(C_6F_5)_3$ was added, as shown in Figure 5.9b. From the transfer characteristics an increase in both I_{ON} and I_{OFF} is observed, where the former has an impact in the mobility and the latter is a sign of effecting p-type doping. Charge carrier mobility is enhanced from 0.5 to 1.2 cm^2/Vs for the linear and from 0.8 cm^2/Vs to 1.9 cm^2/Vs for the saturation regime. Lastly, an increase in the mobility of the C_8-BTBT doped OTFTs with 0.1 mol% of $B(C_6F_5)_3$ was also observe; the transfer curves of pristine and doped OTFTs are presented in Figure 5.9c. An increase in the hole mobility was observed from 0.2 to 0.8 cm^2/Vs for the linear and from 0.4 cm^2/Vs to 1.4 cm^2/Vs for the saturation regime. Overall for the three small molecules, as tested, $B(C_6F_5)_3$ has a positive impact in the charge transport properties, with an increase in the hole mobility and decrease in the threshold voltage.

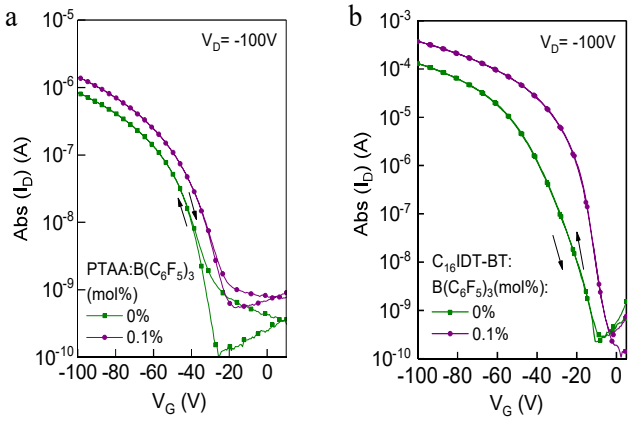


Figure 5.10: Transfer characteristics for the polymer OTFTs with (a) PTAA: $B(C_6F_5)_3$ 0 mol% & 0.1 mol% and (b) C_{16}IDT-BT: $B(C_6F_5)_3$0 mol% & 0.1 mol%.

Next, OTFTs fabricated in BC-TG configuration from the two polymers, PTAA and the C_{16}IDT-BT, were measured and their transfer curves are presented in Figure 5.10 from pristine and doped solutions. For both systems, the addition of 0.1 mol% of $B(C_6F_5)_3$ show an increase in the I_{ON} and in the hole mobility. In particular, a small increase in the charge carrier mobility was observed for the PTAA OTFTs from 0.003 to 0.007 cm^2/Vs for the linear and from 0.005 to 0.01 cm^2/Vs for the saturation regime. More significant was the impact for C_{16}IDT-BT, whose mobility was enhanced from 0.09 to 0.2 cm^2/Vs in the linear and from 0.16 to 0.34 cm^2/Vs for the saturation regime when 0.1 mol% were added in the host solution. Both polymers show that the

addition of $B(C_6F_5)_3$ has a positive impact on the charge carrier mobility as measured from the OTFTs.

From the single component OTFT results, $B(C_6F_5)_3$ shows that it dopes both the small molecules and the polymer materials used in this work. Charge carrier mobility was improved with the addition of an optimum amount of the dopant, threshold voltage was reduced and a small increase in the I_{OFF} was observed in some cases.

5.5 Thin film morphology

5.5.1 POM and AFM imaging

The morphology of the organic semiconducting layer is important for OTFT applications. Several techniques were used in order to examine whether the addition of $B(C_6F_5)_3$ has affected the microstructure of the thin films, as the semiconductor/dielectric interface is crucial for the transistors. Polarised optical microscopy (POM) in combination with Atomic Forced Microscopy (AFM) were applied for the organic thin films.

From the POM images (Figures 5.11a&b), the common spherulite type microstructure of diF-TESADT crystals was observed [29, 56, 117]. The two films of diF-TESADT:PTAA and diF-TESADT:PTAA:$B(C_6F_5)_3$ (2.4 mol%) appeared to have similar microstructure, in which the latter forms smaller crystals. To confirm this finding, thin films were studied with AFM in tapping mode and their topographic images are shown in Figures 5.11c&d. From the height distribution (Figure 5.11e) of the films as extracted from the topography images, different types of microstructure were revealed. The diF-TESADT:PTAA layers exhibit two broad peaks, one with a centre at ~5.8 nm (peak 1) and one at ~30 nm (peak 2). These peaks are assigned in the different regions of the surface where peak 1 is attributed to the flat regions on the film surface (highlighted by box 1), whereas peak 2 refers to regions with a larger height variation (box 2) in Figure 5.11c.

On the other hand, the diF-TESADT:PTAA:$B(C_6F_5)_3$ (2.4 mol%) film exhibited well defined multimodal height distribution indicating the presence of molecularly flat crystalline plateaus. From the height distribution of the (Figure 5.11e) diF-TESADT:PTAA: $B(C_6F_5)_3$ (2.4 mol%) layer three peaks are observed, one centred at ~5 nm (peak 1), ~16 nm (peak 2) and ~31 nm (peak 3). These features are visible in the high-resolution AFM scan (Figure 5.11d) where the numbered boxes are attributed to each peak of the height distribution.

From the AFM scanning, the pristine and doped samples show two different surface topographies as presented in the cartoon schematic of Figure 5.11f. The most drastic change in the microstructure is the formation of molecular terraces in the doped film,

with the crystalline plateaus extending to >10 μm, i.e. distances comparable to the channel length of the OTFTs employed.

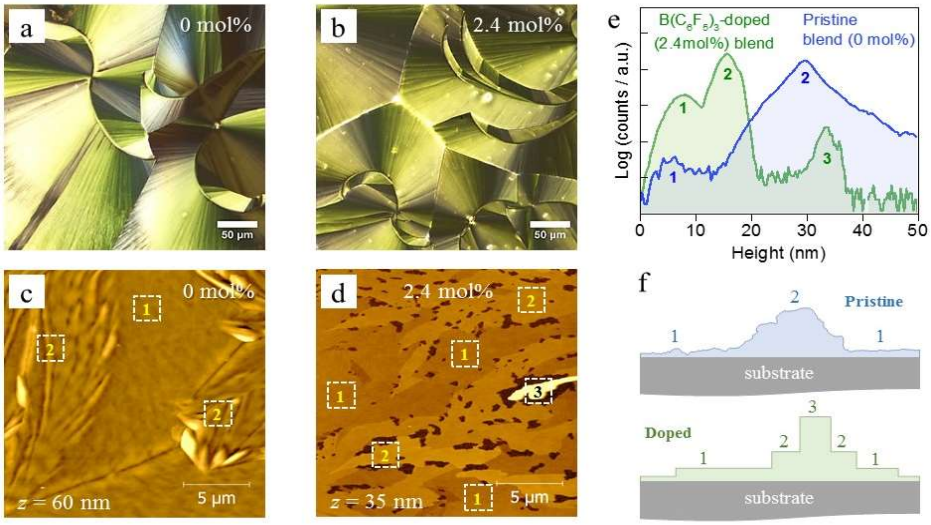


Figure 5.11: Polarised optical microscopy images of diF-TESADT:PTAA (a) a pristine (0 mol%) and (b) $B(C_6F_5)_3$-doped (2.4 mol%) blend layer. Topographical AFM images of diF-TESADT:PTAA (a) a pristine (0 mol%) and (b) $B(C_6F_5)_3$-doped (2.4 mol%) blend layer and (e) their corresponding height histograms. (f) Cartoons representing schematics of the layer cross-section of the pristine and $B(C_6F_5)_3$-doped diF-TESADT:PTAA layers.

The molecularly flat domains which were found in the $B(C_6F_5)_3$ layer resemble molecular terraces, as reported previously in the literature for single crystals diF-TESADT [49] and polycrystalline layers [123]. The diF-TESADT terraces are multiples of the d_{001} spacing of 16.3 $\AA$ of the triclinic $\overline{P}1$ space group.[49, 124] More specifically, the peak 1 of the height distribution of the diF-TESADT:PTAA:$B(C_6F_5)_3$ (2.4 mol%) film (Figure 5.11e) centred at ~8 nm corresponds to an average terrace height profile of five monomolecular layers assuming a monolayer (ML) height of ~16$\AA$. Similarly, peaks 2 and 3 represent terraces compromised of 10 and 20 monomolecular layers. The value of the one ML (~16$\AA$) is close to the d_{001} spacing of the triclinic diF-TESADT crystal. High-resolution AFM scans along with further analysis of the highlighted region (box A) as shown in Figure 5.12a revealed the coexistence of single monolayers (1ML) ~1.6 nm (line scan 1) in height (Figure 5.12c) and multiple monomolecular terraces (line scan 2) in agreement with Figure 5.11e.

From the AFM analysis, the $B(C_6F_5)_3$ doped diF-TESADT:PTAA layer exhibit long range molecular terracing with the c-axis of the diF-TESADT oriented orthogonal to the substrate, whereas the a-b parallel to it. Since these features are only present in the doped layers, the addition of $B(C_6F_5)_3$ mediates the small molecule crystallisation with profound impact on the layer microstructure. The drastic im-

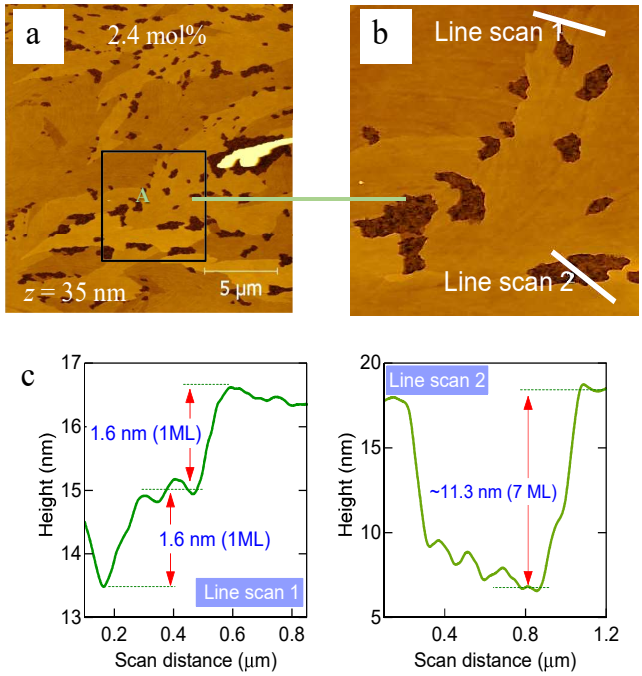


Figure 5.12: (a) AFM topography image for diF-TESADT:PTAA:B(C_6F_5)$_3$- doped layer and (b) high resolution AFM image of region A (box) highlighted in (a). (c) Line scans 1 and 2 obtained from the AFM image in (b).

provement in the crystallinity of the upper phase separated diF-TESADT layer in the diF-TESADT:PTAA:B(C_6F_5)$_3$ (2.4 mol%) blend is playing an important role in the hole mobility enhancement in the OTFTs.

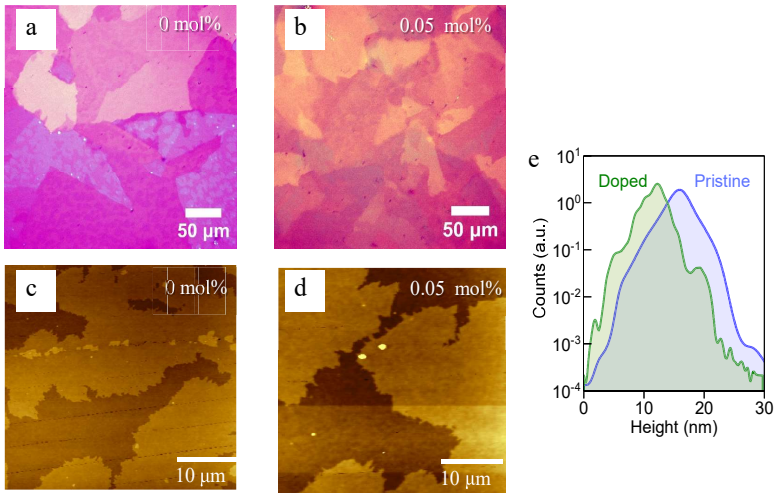


Figure 5.13: POM images for (a) C_8-BTBT:C_{16}IDT-BT & (b) C_8-BTBT:C_{16}IDT-BT:B(C_6F_5)$_3$ (0.05 mol%). Topographical images for (c) pristine C_8-BTBT:C_{16}IDT-BT, (d) doped C_8-BTBT:C_{16}IDT-BT: B(C_6F_5)$_3$ (0.05 mol%) and (e) their corresponding height distribution histograms.

POM and AFM morphology analyse were also applied for the C_8-BTBT:C_{16}IDT-BT and the TIPS-pen:PTAA blends for both pristine and $B(C_6F_5)_3$ doped thin films. Figures 5.13 a&b shows POM images of the C_8-BTBT:C_{16}IDT-BT pristine (0 mol%) and 0.05 mol% $B(C_6F_5)_3$ doped thin films. Spherulitic type morphology is observed from the POM images, which is attributed to the small molecule C_8-BTBT. There were no obvious differences between the pristine and the doped films. For further analysis, AFM was used in tapping mode, and the topography scans are presented in Figure 5.13c&d. Analysis of the height histograms as presented in Figure 5.13e revealed a significant difference between the pristine and doped films. The pristine film exhibited broader height distribution, as compared to the doped, with the latter being characterised by a smoother surface and several distinct peaks indicative of molecular terracing, caused by the addition of $B(C_6F_5)_3$.

Furthermore, the TIPS-pen:PTAA blend films also show a spherulitic type morphology. The $B(C_6F_5)_3$ doped sample exhibits smaller crystals compared to the pristine film, as shown in Figures 5.14a&b. To gain further information in their morphology, AFM in tapping mode was applied and their topographic scans are presented in Figures 5.14 c&d. The $B(C_6F_5)_3$ dopant has a similar smoothing effect on the layer's surface topography, which can be observed from the AFM images and their corresponding height histograms (Figure 5.14e), since the peak of the pristine is broader. However, unlike the other two blend systems, there is no evidence of molecular terracing in the TIPS-pen:PTAA:$B(C_6F_5)_3$ film.

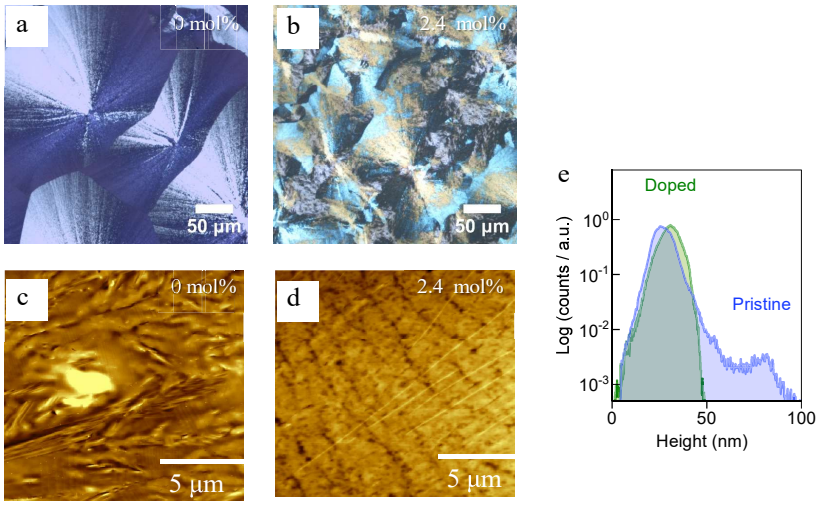


Figure 5.14: POM images for (a) TIPS-pen:PTAA & (b) TIPS-pen:PTAA:$B(C_6F_5)_3$ (2.4 mol%). Topographical images for (c) pristine TIPS-pen:PTAA, (d) doped TIPS-pen:PTAA:$B(C_6F_5)_3$ (2.4 mol%) and (e) their corresponding height distribution histograms.

To conclude on the film morphology, as examined by the POM and AFM analyses,

on the three blend systems diF-TESADT:PTAA, C_8-BTBT:C_{16}IDT-BT and TIPS-pen:PTAA, $B(C_6F_5)_3$ has a positive impact on their morphology. In these organic blend systems enhanced crystallinity was observed by the POM images with smaller size crystals. The AFM analysis revealed that $B(C_6F_5)_3$ addition in certain systems exhibit long-range molecular terracing.

5.5.2 XRD Analysis

Further analysis was conducted on the diF-TESADT:PTAA blend, in order to gain a better understanding of the impact of the $B(C_6F_5)_3$ on the crystallinity of the films by X-ray Diffraction (XRD) in Bragg Brentano geometry. The XRD diffractograms of diF-TESADT, diF-TESADT:PTAA and diF-TESADT:PTAA:$B(C_6F_5)_3$ (2.4 mol%) are presented in Figure 5.15. A thin film of PTAA was also measured, but did not show any peaks, since it is a completely amorphous polymer. The samples exhibit strong diffraction peaks at 2.72-2.74°, which correspond to the d_{001} spacing of the triclinic diF-TESADT crystal ($\overline{P}1$ space group). This finding is in accordance with the AFM observations, where the diF-TESADT peaks were identified as multiples of the d_{001} spacing. Peaks at higher angles were also identified and they correspond to the (00h) family of planes suggesting a (001) lamellar structure parallel to the substrate. The d_{00h} spacing values along with the peak position of the measured samples are presented in Table 2.3.

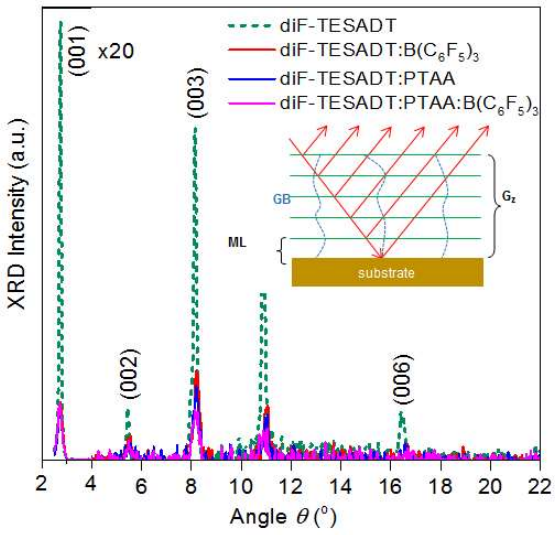


Figure 5.15: XRD diffractograms for diF-TESADT, diF-TESADT:PTAA and diF-TESADT:PTAA:$B(C_6F_5)_3$ (2.4 mol%) thin films.

In order to quantify the XRD results the prominent (00h) diffraction peaks were fitted with Voight curves which they are consisting of a Lorentzian and Gaussian contribution. For the single peak analysis the size broadening is Lorentzian, whereas the

strain broadening is Gaussian. [125] In this case, the size broadening is related to variations in the vertical grain size (G_z), while the latter is related to the microstrain (ϵs), which in turn relates to structural defects and the microscopic strain field around them.[126]

Table 5.2: The Bragg angles (θ) of the three stronger peaks of the films and the corresponding d001 values.

Sample	001		003		004	
	θ^o	d (nm)	θ^o	d (nm)	θ^o	d (nm)
diF-TESADT	2.74	1.61	8.14	1.62	10.89	1.63
diF-TESADT:B(C_6F_5)$_3$	2.73	1.61	8.22	1.61	11.01	1.61
diF-TESADT:PTAA	2.72	1.61	8.19	1.62	10.99	1.61
diF-TESADT:PTAA:B(C_6F_5)$_3$	2.71	1.62	8.16	1.62	N/A	N/A

The cartoon schematic in Figure 5.15 illustrates the origin of microstrain in the case of lamellar layer type of morphology, due to the existence of grain boundaries (GB).[29, 117] As the diffracted X-rays are propagating through the crystalline layers they interact with the strained regions surrounding the diF-TESADT grain boundaries (GBs). The contribution of the strained regions to the XRD signal is expected to be associated with the increased density of GBs in the film. Thus microstrain (ϵs) and grain size (G_z) can be used as indicators of the lateral and out-of-plane crystallinity, respectively. A Gaussian broadening (WG) was used to estimate microstrain (ϵs), while a Lorentzian broadening (WL) was introduced in to Scherrer's formula to determine G_z along the z-direction.

The Voigt fit was applied in the (001) diffraction peaks as they offer the best compromise between the intrinsic angular resolution limits of the XRD measurements and the signal-to-noise ratio. Figure 5.16 shows the (001) peak with the corresponding Voigt fits for the diF-TESADT, diF-TESADT:PTAA and diF-TESADT:PTAA: B(C_6F_5)$_3$ (2.4 mol%) films. Data analysis (Table 5.2) revealed that diF-TESADT:PTAA layers exhibit inferior crystallinity, both out of plane (small G_z) and laterally (large ϵs), as compared to neat diF-TESADT layers. On the other hand, doped diF-TESADT:PTAA: B(C_6F_5)$_3$ (2.4 mol%) layers yield substantially reduced G_z and ϵs values suggesting the existence of thinner layers with enhanced lateral long-range crystallinity. These results are in good agreement with the molecular terraces seen in the AFM analysis. It also suggests that diF-TESADT:PTAA:B(C_6F_5)$_3$ (2.4 mol%) layers contain fewer GBs, which are known to be associated with hole trap states [117], and may explain the improved OTFT performance.

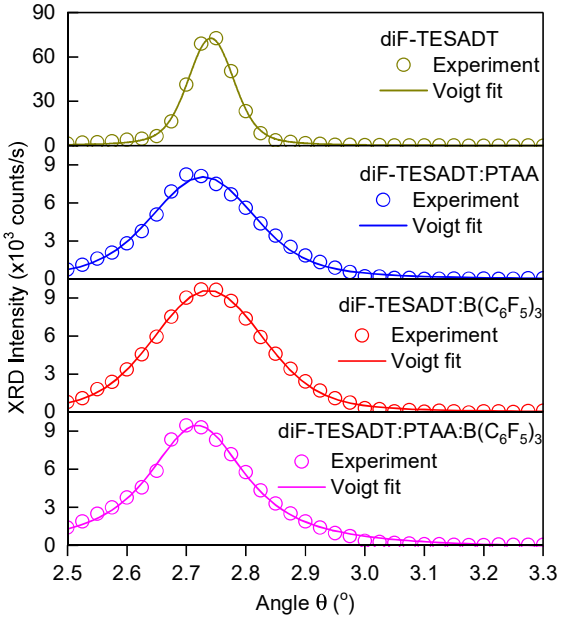


Figure 5.16: X-ray diffractograms around the (001) peak and the corresponding Voigt fits for the diF-TESADT, diF-TESADT:$B(C_6F_5)_3$, diF-TESADT:PTAA, and the diF-TESADT: PTAA:$B(C_6F_5)_3$ (2.4 mol%) films.

Table 5.3: The vertical grain size (G_z) and the microstrain (ϵs) as determined from the three stronger peaks of the films. G_z is an indicator of the vertical crystallinity, whereas ϵs is an indicator of the lateral crystallinity.

Sample	Gz			ϵs		
	(001)	(003)	(004)	(001)	(003)	(004)
diF-TESADT	269.59	50.04	57.50	0.0064	0.0048	0.0022
diF-TESADT:$B(C_6F_5)_3$	130.97	36.40	54.08	0.0168	0.0380	0.0379
diF-TESADT:PTAA	84.66	27.16	12.48	0.0139	0.0592	$6.46\text{x}10^{-8}$
diF-TESADT:PTAA:$B(C_6F_5)_3$	44.16	13.96	N/A	0.0050	$1.94\text{x}10^{-16}$	N/A

5.5.3 Energy levels

The energy levels of the semiconducting pristine and $B(C_6F_5)_3$ doped layers were measured by Kelvin Probe (KP) and Air Photoemission Spectroscopy (APS). The former was used to obtain information for the workfunction, whereas the latter was used for the HOMO energy level of the OSC thin films.

For the diF-TESADT:PTAA blend (Figure 5.17a) a decrease in the workfunction level once $B(C_6F_5)_3$ was added in the blend was observed. At higher doping concentrations (5 mol%) the reduction of the workfunction is about 0.2 eV, while the HOMO level stays at the same level across all samples. The impact of the $B(C_6F_5)_3$ in the

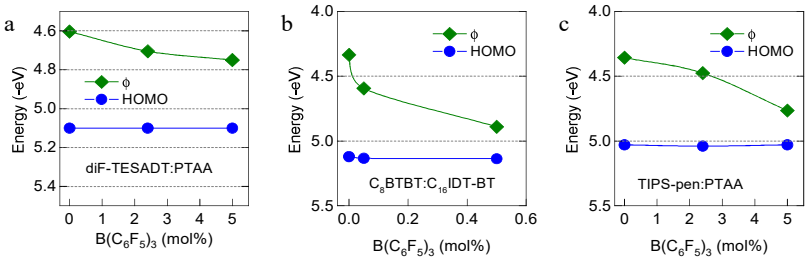


Figure 5.17: Workfunction (ϕ) and HOMO energy levels for the (a) diF-TESADT:PTAA, (b) C_8-BTBT:C_{16}IDT-BT and (c) TIPS-pen:PTAA blends by varying the $B(C_6F_5)_3$ concentration.

C_8-BTBT:C_{16}IDT-BT blend is significant, as the workfunction decrease is about 0.5 eV in the range of 0-0.5 mol%. The HOMO level remains unchanged for this blend too. Lastly, for the TIPS-pen:PTAA blend the overall decrease of the workfunction is about 0.3 eV in the range of 0-5 mol% of $B(C_6F_5)_3$. Overall, the shift in the workfunction is associated with filling the trap states in the organic semiconductor layer due to the existence of the $B(C_6F_5)_3$ dopant in the organic semiconducting blends. Trap filling due to dopants has been studied from several groups via UV photoemission (UPS) and inverse photoemission spectroscopy (IPES). [127, 128]

5.6 Summary

In this chapter, the use of $B(C_6F_5)_3$ as a molecular additive in several organic semiconducting materials is investigated. DFT calculations in a combination with experimental techniques such as KP and APS were used in order to extract the energy levels (HOMO and LUMO) of the semiconducting compounds. As a model organic semiconductor initially the diF-TESADT:PTAA blend was studied, which is a highly crystalline compound – an ideal material for p-type OTFT applications. The energy level difference between the LUMO of the $B(C_6F_5)_3$ (-3.12 eV via DFT) and the HOMO level of the semiconductors ($\sim$5.2 eV) suggested high energy offset and thus ground state integer charge transfer is not favourable. However, a recent study suggested that this is possible to happen as they reported the LUMO of $B(C_6F_5)_3$ at 4.81 eV without stating how they measured it. [120] If integer charge transfer took place in these systems, it would most likely involve the charge transfer from the HOMO level of the blend to the LUMO level of $B(C_6F_5)_3$ resulting in the formation of radical cations, which then lead to p-type doping.

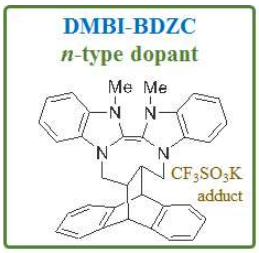
To evaluate the doping effect in the organic semiconducting blends, BC-TG OTFTs were fabricated by varying the concentration of $B(C_6F_5)_3$. Hole charge carrier mobili-

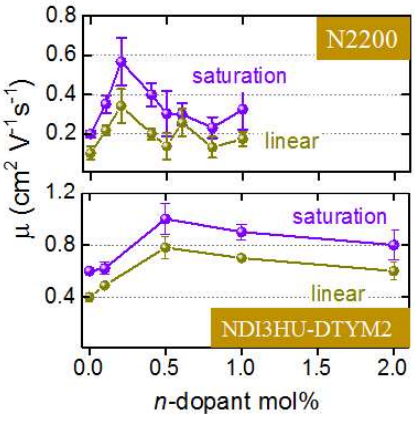
ties up to ∼8 and 11 cm^2/Vs for the diF-TESADT:PTAA and the C_8-BTBT:C_{16}IDT-BT blends, respectively were obtained. Doping the TIPS-pen:PTAA blend also resulted in an improved mobility of 3.7 cm^2/Vs. Further analysis on the data indicated the reduction of the contact resistance due to trap filling by $B(C_6F_5)_3$. Single component OTFTs were also fabricated seperately in order to examine the effect of $B(C_6F_5)_3$ on each component of the blends. It was shown that $B(C_6F_5)_3$ is a powerful dopant in both small molecules and polymers.

A further important discovery was the positive impact of the $B(C_6F_5)_3$ in the thin film microstructure of the organic semiconductor blends, with certain systems exhibiting long-range molecular terracing. X-Ray diffraction is in accordance with the AFM analysis, where the results suggested that the doped diF-TESADT:PTAA layer consist of single or multiple molecular terraces of 1.6 nm. Furthermore, the shift in the work-function upon doping was measured by KP and APS technique for the three blends presented in this work. To conclude, the semiconducting blends undergo simultaneous p-doping with enhanced charge transport properties along with improved crystallinity.

Chapter 6

N-type Doping OTFTs





In this chapter, a new and non-volatile n-type molecular dopant (12a,18a)-5,6,12, 12a,13,18,18a,19- Octahydro-5,6 -dimethyl-13,18[1', 2']- benzenobisbenzimidazo[1,2-b:2',1'-d]benzo[i][2.5] benzodiazocine potassium triflate adduct (DMBI-BDZC) is presented for doping the organic semiconducting layer of thin film transistor. There is a need of new organic semiconducting materials that can perform as n-type dopants. According to DFT calculations and due to the position of the HOMO level of the DMBI-BDZC, ground state integer charge transfer is possible to occur between the selected OSCs for this study. To investigate this experimentally, EPR was used and the generation of unpaired electrons in the doped samples were observed. OTFTs were also used to study the impact of the DMBI-BDZC in films of a small molecule and a polymer as an n-type dopant. Not only the charge carrier transport of the doped films was enhanced, but also other crucial OTFT parameters were significantly improved, including the contact resistance and the threshold voltage of the devices. Finally, the impact of the dopant on the morphology of the semiconducting thin films was evaluated with AFM and XRD studies.

6.1 Introduction

Doping the organic semiconductor materials for electronic applications is a common approach to improve the semiconductor properties. [93, 104] For thin film transistors not only the charge carrier mobility is enhanced, but other crucial device parameters are improved. Although extensive work has been performed in doping p-type organic semiconductors, limited work is available for n-type OSC materials. One reason behind this is the requirement of electron deficient units in the OSC molecule with lowest unoccupied molecular orbitals (LUMO) energy levels that are not too low. [34] Materials with low LUMO levels usually result in molecules which are not air stable and difficult to chemically synthesise; the LUMO level should be below ∼4 eV in order to be air stable. Identifying materials that can be used as n-type molecular dopants is significantly challenging and this was the motivation behind this project.

6.2 Organic semiconducting materials

The use of a previously unidentified n-type material which can be used as a molecular additive for n-type organic semiconductors is presented: the (12a,18a)-5,6,12,12a,13,18,18a,19-octahydro -5,6-dimethyl-13,18[1',2']- benzenobisbenzimidazo[1,2-b:2',1'-d]benzo[i][2.5] benzodiazocine potassium triflate adduct (DMBI-BDZC). Density Functional Theory (DFT) calculations were used to identify the energetics of the organic semiconducting materials and the dopant. The energy of the frontier orbital of the LUMO of the DMBI-BDZC was found to be -0.74 eV, whereas the HOMO was at -3.84 eV. As organic semiconducting hosts NDI semiconductors were selected: the polymer poly((N,N'-bis(2-octyldodecyl)-naphthalene-1,4,5,8-bis(dicarboximide)-2,6-diyl)-alt- 5,5'-(2,2'-bithiophene)) (N2200) and small molecule naphthalene diimides fused with 2- (1,3-dithiol-2-ylidene) malononitrile groups (NDI-DTYM2) (NDI3HU-DTYM2), whose molecular structures are presented in Figure 6.1.

Both materials are known from the literature for their electron transporting properties and high charge carrier mobilities in OTFTs. [129–131] According to DFT calculations, N2200 has dimer HOMO and LUMO energy levels at -5.8 and -3.8 eV respectively, consistent with previous reported values. [41] As presented in Figure 6.2 there is a minimal energy offset (0.04 eV) between the HOMO of the DMBI-BDZC and the LUMO of N2200. Ground state integer charge transfer is possible between DMBI-BDZC and N2200 polymer.

Furthermore, for the small molecule NDI3HU-DTYM2 the HOMO energy level was found to be at -7.09 eV and the LUMO at -4.80 eV from the DFT calculations. The energy offset for the NDI3HU-DTYM2 and the DMBI-BDZC is higher and thus charge transfer is most likely to occur between them. Due to its low HOMO level (3.84 eV)

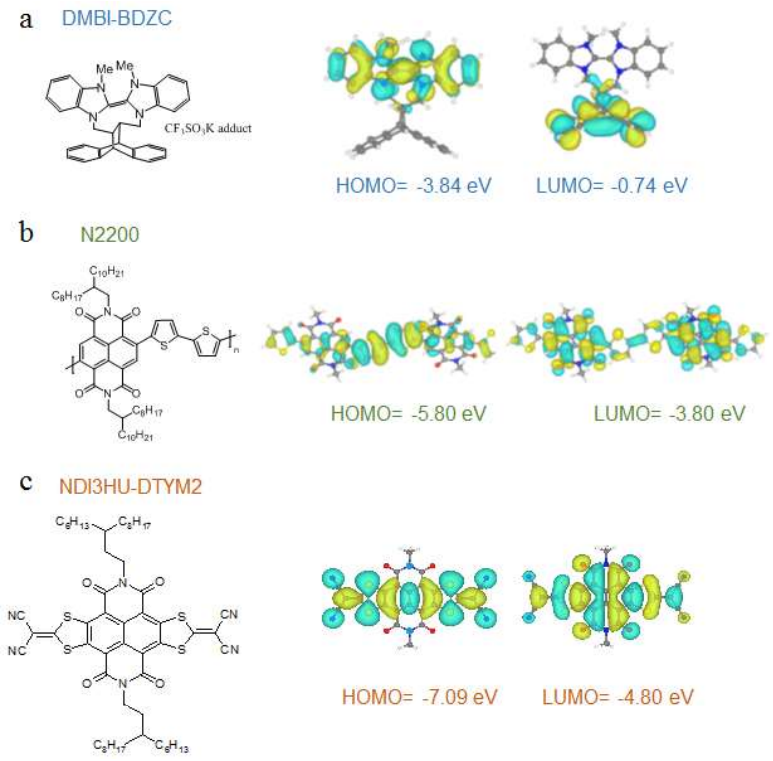


Figure 6.1: Molecular structures of n-type organic semiconductors and their energy levels as predicted by DFT calculations (a) for the molecular dopant DMBI-BDZC, (b) the polymer N2200 and (c) the small molecule NDI3HU-DTYM2.

according to the DFT calculation, DMBI-BDZC is a strong candidate for n-type doping of organic semiconductors.

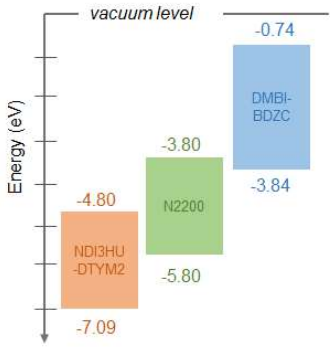


Figure 6.2: Energy levels as predicted by DFT calculations (a) for the molecular dopant DMBI-BDZC, (b) the polymer N2200 and (c) the small molecule NDI3HU-DTYM2.

6.3 Electron Paramagnetic Resonance Measurements

Electron paramagnetic resonance was used to evaluate whether DMBI-BDZC has doping effect on the N2200 and NDI3HU-DTYM2 semiconducting host materials, as pre-

dicted by the DFT calculations. As described in Chapter 4.3.5, the EPR technique has been widely used in organic semiconductors to assess doping, as it can detect the presence of unpaired electrons. [129, 132] A magnetic field was applied to promote the transition of the free electrons in the n-type pristine (0 mol%) and DMBI-BDZC doped layers. Figures 6.3a&c show the EPR signal for the pristine and doped N2200 and NDI3HI-DTYM2 doped layers. In both cases the pristine films show no EPR signal, whereas with a small amount of DMBI-BDZC there is a clear increase in the signal intensity, which is evidence of successful n-type doping of the host semiconductors. For the N2200 polymer, as seen in Figure 6.3b the energy offset (ΔE) between the HOMO of the DMBI-BDZC and the LUMO of the N2200 is small (0.04 eV), thus electron transfer is occurring. In the case of NDI3HU-DTYM2, ΔE is larger ($\sim$ 1 eV) leading to successful n-type doping, as shown in the EPR results of Figure 6.3b. According to the EPR results, a small addition of DMBI-BDZC in the organic semiconducting host solutions generates free charge carriers.

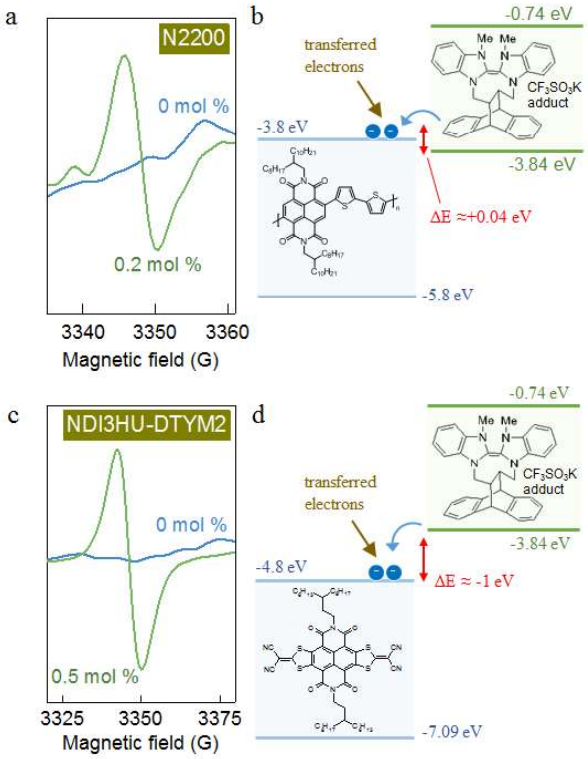


Figure 6.3: EPR measurements (a&c) and doping mechanism (b&d) for the n-type doped layers with DMBI-BDZC for the (a&b) N2200 and (c&d) NDI3HU-DTYM2.

6.4 Electrical Characterisation

To study the charge transport properties of the pristine (0 mol%) and DMBI-BDZC doped N2200 and NDI3HU-DTYM2 materials, thin film transistors were used. OTFTs in bottom contact-top gate (BC-TG) configuration were fabricated on glass substrates. Further experimental details on the device fabrication and solution processing are presented in Chapter 4.1. For the polymer N2200, doping was explored in the range of 0-1 mol%, whereas for the small molecule NDI3HU-DTYM2 the range was varied from 0 to 2 mol%. V_G

6.4.1 N-type OTFTs

Representative transfer (I_D vs V_G) and output curves (I_D vs V_D) of N2200:DMBI-BDZC (0-1 mol%) OTFTs with their corresponding square root of the drain current vs gate voltage ($I_D^{1/2}$ vs V_G) are presented in Figures 6.4a,b&e. Transfer curves were measured by applying V_D=80 V for the saturation regime.

From the transfer curves (Figure 6.4a) the doping effect can be clearly seen, as there is a small increase in the off-current I_{OFF} until 0.8 mol% followed by a large increase when 1 mol% of DMBI-BDZC were added in the N2200 solution. From the $I_D^{1/2}$ (Figure 6.4b) the shift of the threshold voltage (ΔV_T) towards less positive values of about 20 V can be observed, as well as the increase in the on-current I_{ON} upon doping. The shift on the V_T is mainly attributed to two factors: the increased density of free charge carriers in the channel and due to the filling of trap states caused by the dopant addition. [136,137] Representative output curves of N2200:DMBI-BDZC (0-1 mol%) are presented in Figure 6.4e as measured by applying V_G=80 V, where the increase in the I_D is clear with the dopant addition.

In a similar manner, doping of the small molecule NDI3HU-DTYM2 was explored in the range of 0-2 mol%. There is a clear increase in the I_{OFF} (Figure 6.4c), which is caused by the traps filling and it is more pronounced in the case of the NDI3HU-DTYM2 when comparing with the N2200 polymer. DMBI-BDZC also causes a positive shift in the V_T as presented in Figure 6.5b. Representative output curves of NDI3HU-DTYM2:DMBI-BDZC (0-2 mol%) are presented in Figure 6.4f, as measured by applying V_G=100 V, where the difference in the drain current between the pristine and the doped is pronounced. Evidently, DMBI-BDZC has a notable impact on the OTFTs based on both organic semiconducting materials with significant signs of n-doping.

Doping with DMBI-BDZC also has a profound effect on the electron transport characteristics of both polymer and small molecule OTFTs, since the channel current is enhanced. The electron charge carrier mobility was extracted for both linear and saturation regimes and their evolution with the DMBI-BDZC mol% addition is presented in Figures 6.5a&b. The pristine (0 mol%) N2200 OTFTs show charge carrier

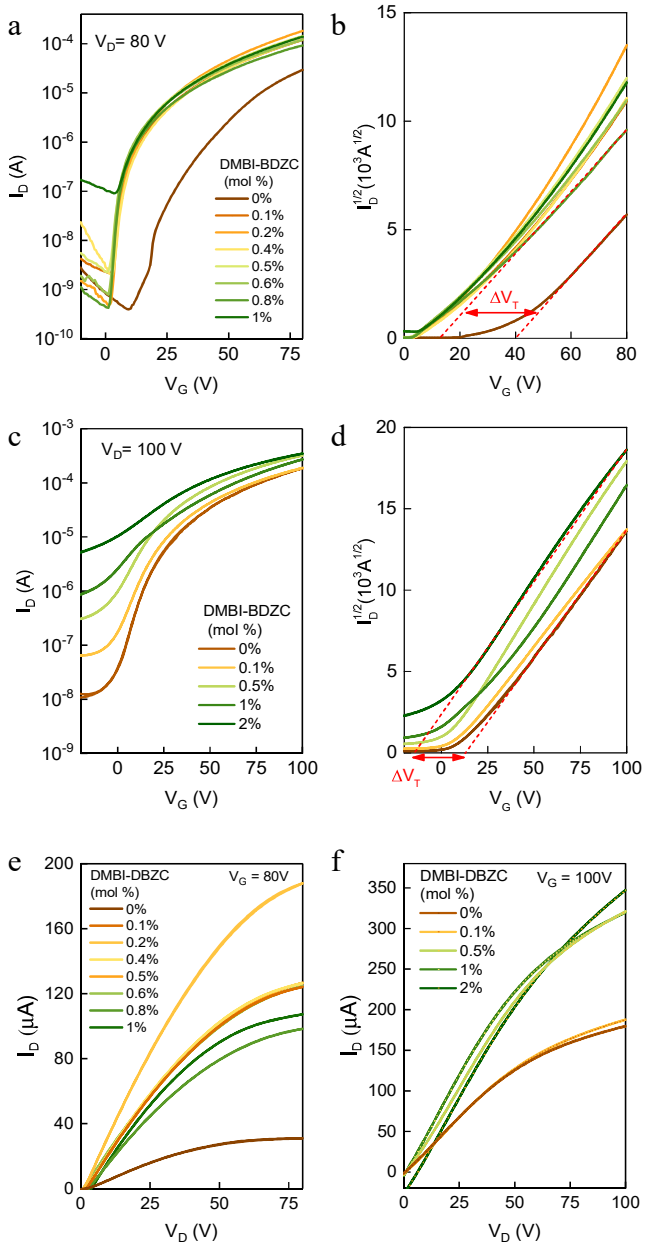


Figure 6.4: Transfer characteristics (a&c) of the (a) N2200:DMBI-BDZC TFTs and (b) NDI3HU-DTYM2:DMBI-BDZC with their corresponding square root of the I_D vs V_G plots (b&d). The output curves (e&f) for the N2200:DMBI-BDZC (e) (0-1 mol%) and NDI3HU-DTYM2:DMBI-BDZC (f) (0-2 mol%).

mobilities of 0.1 and 0.2 cm^2/Vs in the linear and saturation regimes, respectively. A maximum mobility of 0.4 and 0.7 cm^2/Vs was obtained when a 0.2 mol% solution of DMBI-BDZC was added to the N2200 solution.

A similar behaviour was observed for the NDI3HU-DTYM2 OTFTs, where the pristine devices showed charge carrier mobilities of 0.4 in the linear regime and 0.8

cm^2/Vs in the saturation regime, whereas the highest electron mobility was achieved with the addition of a 0.5 mol% solution of DMBI-BDZC OTFTs with values reaching 0.8 and 1.1 cm^2/Vs in the linear and saturation regime, respectively. For both systems there is a similar trend in the charge carrier mobility, whereas when the dopant concentration increases beyond the optimal amount, the mobility reduces. The addition of the DMBI-BDZC has also a drastic impact on the threshold voltage V_T, as can be seen in Figures 6.5 a&b. V_T reduces with 0.1 mol% of DMBI-BDZC and then remains at similar levels for the higher doping concentrations. Finally, the characteristic decrease in the on-off ratio ($I_{ON/OFF}$) can be observed in both N2200 and NDI3HU-DTYM2 OTFTs upon doping (Figure 6.5 a&b). The main reason behind this degradation is the increase in the off current by the dopant addition in the OSC.

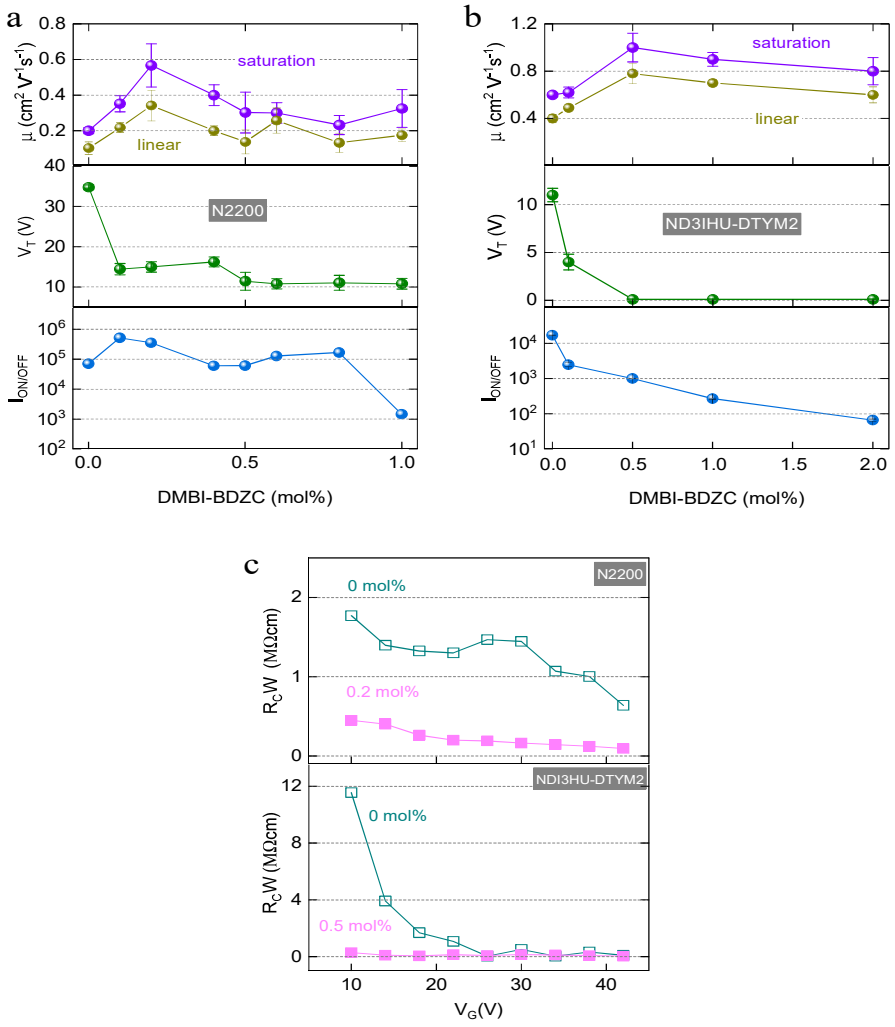


Figure 6.5: Electron charge carrier mobility, threshold voltage and on/off current ratio evolution for (a) N2200:DMBI-BDZC (0-1 mol%) and (b) NDI3HU-DTYM2 (0-2 mol%) OTFTs. (c) Contact resistance for pristine (0 mol%) and DMBI-BDZC doped OTFTs as calculated via the TLM method.

Another important parameter of the OTFTs is the contact resistance (R_C), in which has been proven that addition of the molecular dopants can reduce the value significantly.[34] Parasitic contact resistance affects the device operation and leads to inaccurate device parameter extraction, such as overestimation of the charge carrier mobility. [133] Contact resistance was calculated from transistor characteristics by following the TLM method, as described in Chapter 2.4.5. Figure 6.5c shows R_C with increasing V_G as calculated for the pristine and best performed DMBI-BDZC doped OTFTs with N2200 and NDI3HU-DTYM2 as host semiconductors. In N2200 OTFTs, R_C is found to be reduced from 1.8 to 4.8 MΩ cm at V_G =10 V. In the case of NDI3HU-DTYM2 OTFTs, n-doping with DMBI-BDZC reduces R_C by approximately one order of magnitude at low V_G values (V_G = 10 V), but approaching similar values at higher V_G.

Overall, for the OTFTs with N2200 and NDI3HU-DTYM2 the addition of DMBI-BDZC not only to enhances the charge transport properties of the semiconductors, but also improves important OTFT parameters such as the threshold voltage and the contact resistance.

6.4.2 Low temperature measurements

To gain a better understanding in the charge transport properties caused by the addition of the DMBI-BDZC dopant, transfer curves of the OTFTs were measured over a temperature range of 77 to 310 K. Transfer curves in the linear regime (V_D= 10 V) for N200:DMBI-BDZC 0 & 0.2 mol% and NDI3HU-DTYM2:DMBI-BDZC 0&0.5 mol% from OTFTs with channel width 1000 μm and length 40 and 30 μm, respectively are presented in Figure 6.6. The effect of the temperature on the OTFTs is more pronounced for the polymer (N2200) devices when comparing them with the small molecule (NDI3HU-DTYM2).The reason behind this is attributed to the fact that the polymer and the small molecule have different intermolecular interactions. The electronic overlap in the polymer is much smaller than the small molecule and so the polymer requires more thermal energy in order to achieve enough orbital overlap for effective charge transport. [134]

The drain current in the linear regime of the devices was used for the activation energy (E_A) calculations. As described in Chapter 2.2.2 the extraction of E_A was based in the Multiple Trapping and Release (MTR) and Meyer-Neldel models, which relate the effective mobility (μ_{eff}) with the activation energy and the temperature. This analysis averages all trap states over the deep traps and tail states in the band gap. The activation energy is considered as the trap energy level relative to the transport level. The Arrhenius plots of the $\ln(\mu_{eff})$ vs 1000/T for the pristine and DMBI-BDZC doped N2200 and NDI3HU-DTYM2 OTFTs are presented in Figures 6.7 a-d

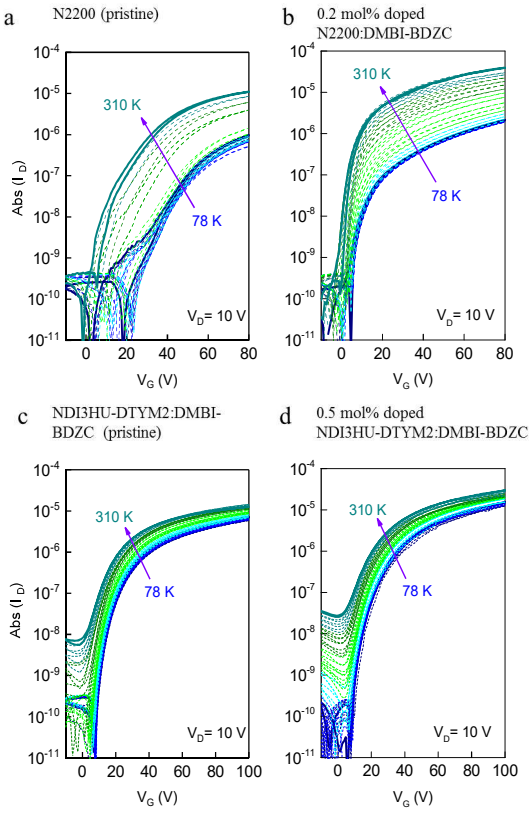


Figure 6.6: Temperature dependent charge transport measurements performed in the range 78-310 K. Transfer characteristics of (a) pristine & (b) 0.2 mol% DMBI-BDZC-doped N2200 OTFTs, with channel width 1000 μm and length 40 μm. Transfer characteristics of (c) pristine & (d) 0.5 mol% DMBI-BDZC-doped NDI3HU-DTYM2 OTFTs, with channel width and length of 1000 and 30 μm, respectively.

for different drain voltages V_D. In both systems, temperature activated charge carrier transport with two distinguishable conduction regimes is observed. This effect has been observed in other organic semiconducting systems and it is related to the higher thermal energy required for the additional charge transport pathways, which result in higher activation energy at higher temperature. [32, 134, 135]

The temperature value which separates the low from the high temperature regime is different for the pristine and doped OTFTs. For the pristine N2200 OTFTs this temperature is at ~193 K, while for the 0.2 mol% it is ~178 K, both highlighted in the shaded areas in Figure 6.4.4a&b. This area in both 0 and 0.2 mol% DMBI-DBZC doped N2200 OTFTs is well defined and remains unchanged by increasing the V_G. The electron mobility of the pristine OTFTs varies over three orders of magnitude with a minimum value of $\sim 10^{-4}$ cm^2/Vs at 78 K and a highest value of 0.1 cm^2/Vs at 300 K. On the other hand, doping the N2200 devices with 0.2 mol% DMBI-BDZC seems to have a significant effect on the electron mobility which shows a maximum at 0.6 cm^2/Vs (300 K) and a minimum of $\sim 10^{-2}$ cm^2/Vs (78 K).

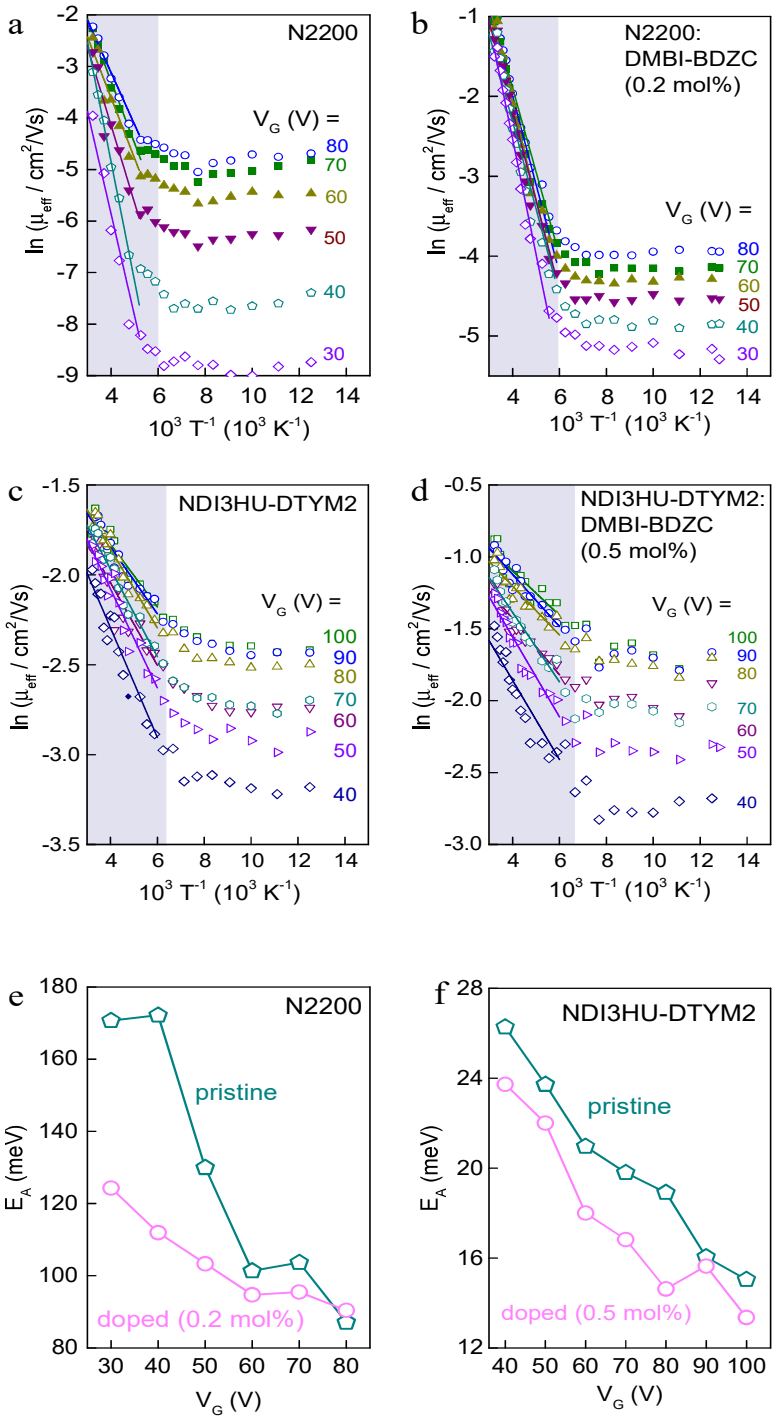


Figure 6.7: Arrhenius plots of N2200:DMBI-BDZC OTFTs with channel width 1000 μm and length 40 μm for (a) 0 mol% & (b) 0.2 mol% and NDI3HU-DTYM2:DMBI-BDZC with channel width 1000 μm and length 30 μm for (c) 0 mol% and (d) 0.5 mol%, as extracted from OTFTs when measured by applying V_D= 10 V. Activation energy E_A as function of V_G, as extracted from (a-d) for (e) N2200:DMBI-BDZC and (f) NDI3HU-DTYM2:DMBI-BDZC OTFTs.

The activation energy was calculated for both systems as presented in Figure 6.7e by varying the V_G. A decrease in the activation energy is observed as the gate voltage increases, which is related to the charges filling the lower-lying state induced by the gate voltage. [134] More importantly, there is a significant difference in the E_A of the pristine and 0.2 mol% doped OTFTs, as E_A decreases by almost 50 meV from its initial value of 170 meV for the pristine (at V_G = 30 V). The decrease in the E_A is expected as the dopant fills the trap states and shifts the Fermi energy towards the LUMO level. [136]

Regarding NDI3HU-DTYM2 OTFTs, for the pristine devices the transition temperature is at 169 K, whereas for the 0.5 mol% DMBI-BDZC it is 175 K, as indicated by the highlighted box as in Figures 6.7c&d. The reduction of the E_A in this case is less dramatic, as in the 0.5 mol% doped OTFTs it only reduces by 2 meV at V_G= 40 V. This observation is possible due to the highly crystalline nature of the material, which has the tendency to expel the dopant molecule away from its lattice upon nucleation.

6.4.3 Trap density

From the data analysis, as presented in Section 6.4.1-6.4.2, the DMBI-BDZC is acting as an effective n-type dopant in the two OSC systems presented by filling the trap states in the OSC/dielectric interface. To verify this, the trap density and trap concentration were extracted from the transfer characteristics (Figure 6.6) of the OTFTs. By using the formulas described in Chapter 2.4.4.2, the relative variation of ΔN_{tr} and ΔD_{tr} versus the DMBI-BDZC concentration is presented in Figure 6.8.

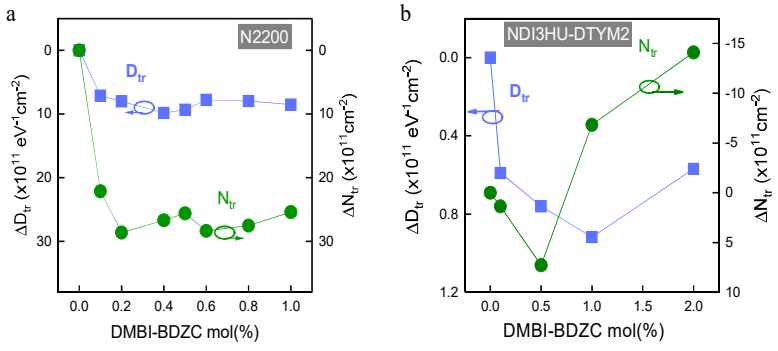


Figure 6.8: Relative trap density (ΔN_{tr}) and trap concentration (ΔD_{tr}) for the (a) N200:DMBI-BDZC and (b) NDI3HU-DTYM2:DMBI-BDZC OTFTs as calculated from the transfer curves.

Both trap density and trap concentration decrease by introducing the dopant in the N2200. This finding is consistent with the reduction in the activation energy of ∼50

meV (Figure 6.7) and the reduced contact resistance and threshold voltage (Figure 6.5). Moreover, the dopant in the small molecule NDI3HU-DTYM2 does not affect the N2200 OTFs the trap concentration as much, which was also evident in the activation energy analysis (Figure 6.7). On the hand, the trap density decreases when 0.1-0.5 mol% solutions of DMBI-BDZC were added in the NDI3HU-DTYM2, followed by a sharp increase at higher doping concentrations. This observation is likely to be related to structural defects induced in the small molecule layer upon doping, which is in agreement with previous reports. [66, 129]

6.5 Morphology Characterisation

The morphology of the organic semiconducting thin film is important in order to understand whether addition of the dopant molecules caused any disruption in the lattice of the hosts. Thus in this section, several morphology characterisation techniques are presented including polarised optical microscopy (POM), X-Ray diffraction (XRD) and Atomic Force Microscopy (AFM). A brief description of these techniques is given in Chapter 4.3.

Polarised microscopy is a useful technique which enables the observation of the crystalline features in the organic semiconductor layers. Figure 6.9 shows POM images of the small molecule pristine NDI3HU-DTYM2 and DMBI-BDZC doped in the range of 0.1-2 mol%. The material is highly crystalline with needle-type morphology. Obvious conclusions can not be drawn to understand the impact of the dopant in the small molecule.

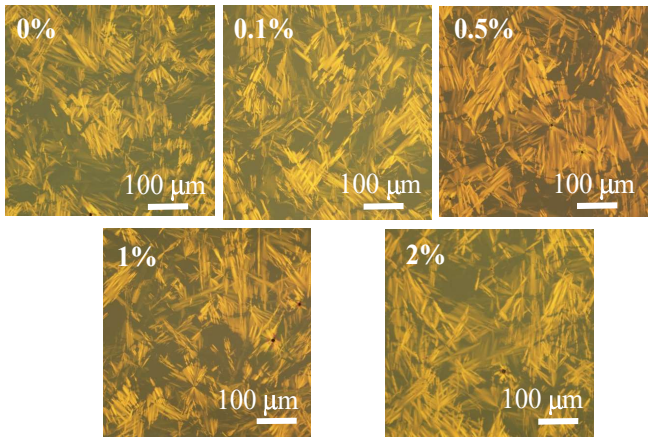


Figure 6.9: POM images of NDI3HU-DTYM2:DMBI-BDZC 0-2 mol% thin films.

On the other hand, using POM to analyse the morphology of the polymer N2200, revealed that the material is not crystalline and thus no patterns could be observed by the polarised microscope. Further experimental techniques are required to investigate

their morphology.

6.5.1 AFM Characterisation

Atomic force microscopy (AFM) was used for both pristine and DMBI-BDZC doped N2200 and NDI3HU-DTYM2 thin films.

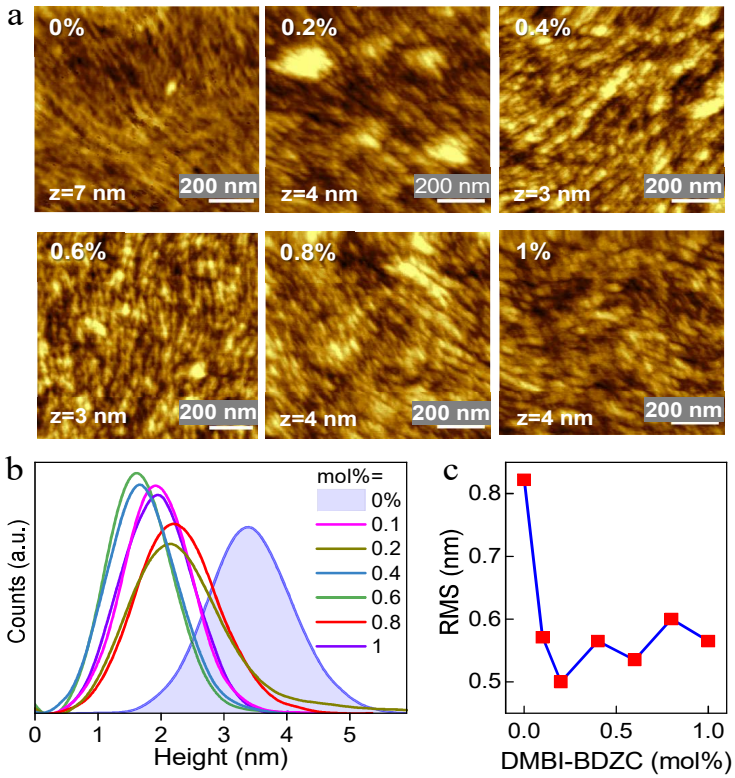


Figure 6.10: AFM morphology analysis for N2200:DMBI-BDZC (0-1 mol%) (a) Topography AFM scans of thin films, (b) their corresponding height histogram and (c) the surface roughness (RMS) as a function of DMBI-BDZC mol%, as extracted from the topography scans.

Information about the thin film morphology, crystalline layers and their roughness can be extracted by the topography scans. Figure 6.10a shows the AFM scans of the pristine (0 mol%) and 0.2-1 mol% DMBI-BDZC N2200 thin films. A similar fibril type surface morphology was observed for all the films. However, a significant shift ($\sim$ 2 nm) in their height distribution towards smaller height values indicates that the dopant addition leads to a smoother film surface (Figure 6.10b). The width of the peaks also decreased, when comparing the pristine and doped samples leading to lower root mean square (RMS) surface roughness values, as presented in Figure 6.10c. The RMS value decreases by about 2 nm when a 0.1 mol% of solution DMBI-BDZC was added to the N2200. At higher dopant concentrations RMS stays at a similar value.

AFM analysis was also performed for the pristine NDI3HU-DTYM2 and DBMI-BDZC doped small molecule thin films. Topography scans are presented in Figure 6.11a, where they show high crystalline terrace-like morphology. Further information arose from the height distribution (Figure 6.11b) of the films as extracted from the topography scan, where the presence of distinct peaks was revealed. The peaks on the height distribution correspond to different plateau/terraces as they are indicated on the AFM scan images. The height difference between the terraces, as calculated from the distance between the peaks, is between 2-3 nm for most of the films. Further morphological investigation is required to understand better the impact of the dopant in the organic semiconducting thin films.

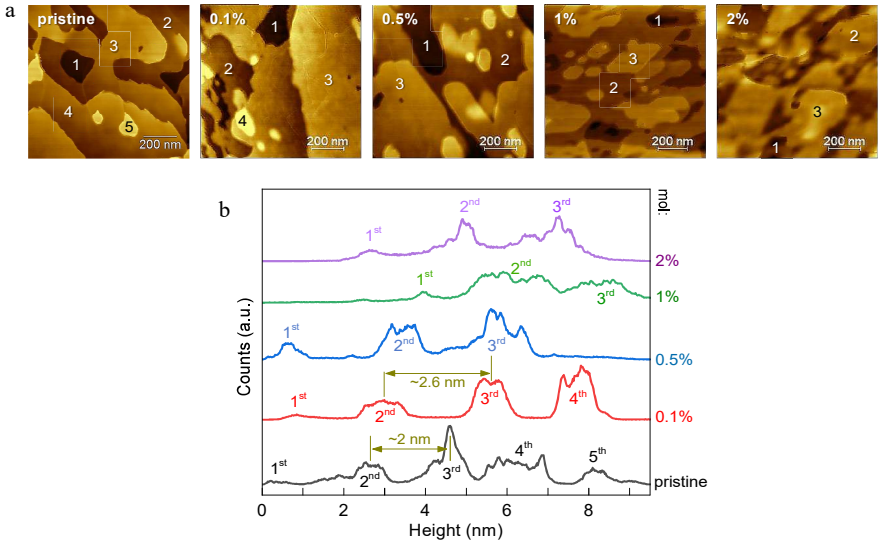


Figure 6.11: AFM morphology analysis for NDI3HU-DTYM2:DMBI-BDZC (0-2 mol%). (a) Topography AFM scans of thin films and (b) their corresponding height histogram.

6.5.2 X-Ray Diffraction Characterisation

X-Ray diffraction analysis was performed in pristine and DMBI-BDZC doped thin films of N2200 and NDI3HU-DTYM2 in order to gain a better understanding whether their crystallinity was affected by the dopant. Thin films were deposited on glass substrates and the XRD patterns are presented, as measured in the range of 2-25°, in Figure 6.12.

The N2200 thin film exhibits a lamellar structure with diffraction peaks (100) and (200) at 2θ = 3.57° and 7.22°, respectively, with a lamellar packing distance of 2.41 and 1.22 nm, as showed in Figure 6.12a. Also, a-π-π stacking peak (010) at 2θ = 22.92° is observed, which corresponds to a π-π stacking distance of 0.39 nm. These observations are in good agreement with previously reported data in the literature. [129] DMBI-BDZC addition in the range of 0.2-2 mol% does not change the diffraction

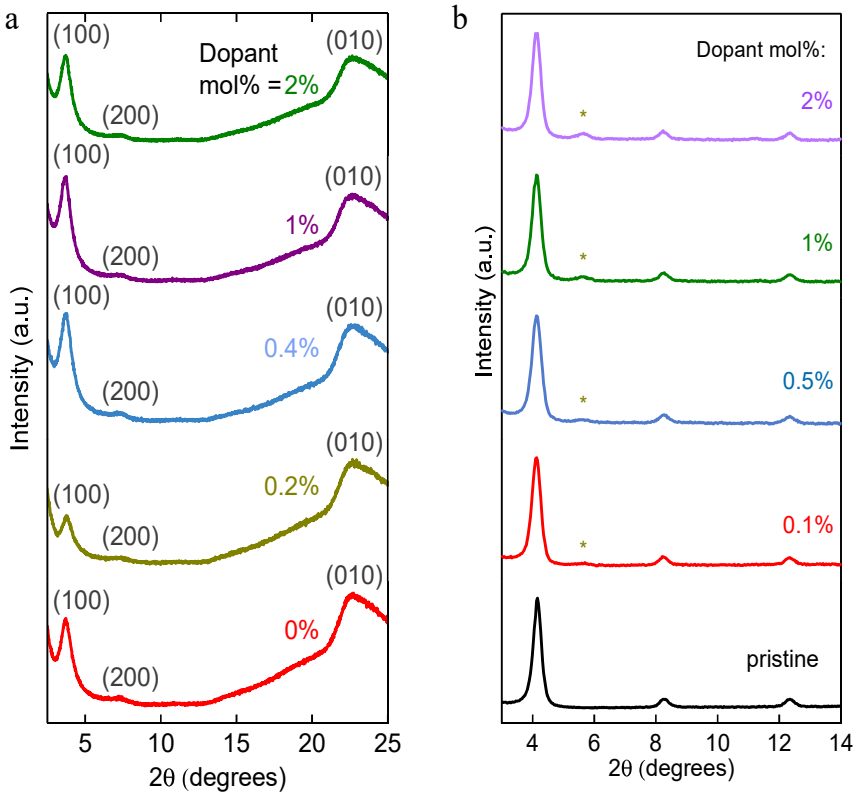


Figure 6.12: X-Ray diffraction patterns for pristine and DMBI-BDZC doped (a) N2200 and (b) NDI3HU-DTYM2 thin films.

peaks and thus the packing of the polymer is not affected, which is in accordance with the results from the AFM analysis (Chapter 6.5.1).

Figure 6.12b shows the XRD patterns of the pristine NDI3HU-DTYM2 thin films and DMBI-BDZC doped in the range of (0.1-2 mol%). Similar patterns are observed for all the films with diffraction peaks at 2θ = 4.16°, 8.27° and 12.34°, with d-spacing of 2.13, 1.07 and 0.72 nm, respectively, which is in accordance with previously reported data.[130] The DMBI-BDZC addition in the small molecule leads to an additional peak at 5.70°, with a d-spacing of 1.55 nm (indicated by the asterisk in Figure 6.12b). It can be observed that by increasing the dopant amount (mol%) the intensity of this peak is also increasing; this can be related to either the dopant segregation or change in the packing motif of the small molecule. Interestingly, the XRD results suggested a d-spacing of ∼2 nm which is in accordance with the difference in the terrace height different as extracted from AFM analysis (Figure 6.10), indicating the presence of large monomolecular terraces, in agreement with previous reports. [130]

6.6 Summary

In this chapter, a previously unidentified material, DMBI-BDZC, is presented as a strong candidate for the application of an n-type dopant for organic electronics. In particular, due to its HOMO energy level at -3.84 eV, doping is occurring via the conventional ground state integer charge transfer mechanism, as predicted by the DFT simulations. Two organic semiconductors were used as hosts, the polymer N2200 and the small molecule NDI3HU-DTYM2 and it was showed via DFT that electron transfer is possible to happen. This hypothesis was confirmed with the EPR measurements, where an increased signal intensity observed for the doped films, in comparison to the pristine films. This signal is attributed to the unpaired or free electrons generated in the host semiconductors with the addition of the dopant.

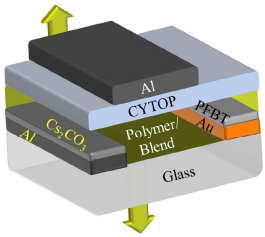
As an application of this new dopant, organic thin films transistors were fabricated from both the small molecule and the polymer from pristine and doped solutions. The charge carrier mobilities in linear and saturation regimea were increased when small amounts of the DMBI-BDZC were added to N2200 (0.2 mol%) and NDI3HU-DTYM2 (0.5 mol%). A large decrease on the threshold voltage was obtained, which is attributed to the successful filling of the trap states from the dopant. Thin film transistor devices were also measured under different temperatures in the range of 70-320 K, in order to study the effect of the dopant in the activation energy. For the N2200 devices a drastic decrease on activation energy on the doped devices was found, which is in agreement with our results on successful doping. A less profound difference was observed in the activation energy for the pristine NDI3HU-DTYM2 and doped OTFTs.

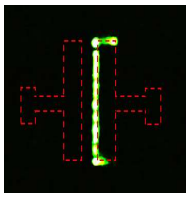
In the last section of this chapter, morphology characterisation of the pristine and doped thin films is presented. POM showed high crystalline films were fabricated from the NDI3HU-DTYM2 small molecule, whereas no patterns were observed for the polymer N2200. Furthermore, AFM analysis revealed that the dopant has a smoothening effect on both materials, since for all the doped thin films lower values of RMS were measured. XRD on N2200 showed that the dopant addition is not affecting the structure of the material. On the other hand, for the NDI3HU-DTYM2 small molecule a new peak was observed in the XRD pattern which might be related to the dopant segregation or change in the packing motif of the small molecule.

Overall, this chapter demonstrates DMBI-BDZC as a new n-type dopant for organic semiconductors with application in organic thin film transistors and opens a new area for research. The applicability on this material for other device applications, such as solar cells will be an interesting next step. Further research is also required to gain a better understanding on the impact of the dopant on the morphology of small molecules.

Chapter 7

Organic Light Emitting Transistors





This chapter describes the development of an organic semiconducting blend for light emitting transistors (OLETs). The use of a high mobility light emitting polymer blended with a small molecule enabled the fabrication of single layer OLETs. A charge carrier hole mobility $\succ 1$ cm^2/Vs was achieved, which is an important development for high perfomance OLETs.

7.1 Introduction

In the past decade progress in light emitting transistors (OLETs) has been significant, due to their potential applications, including optical communication systems, electroluminescent displays, solid state lighting sources [137, 138] and electrically pumped organic lasing. [77] OLETs combine the electrical characteristics of the organic thin film transistors with the light emitting properties of the organic light emitting diodes (OLEDs). [81, 139]

OLETs were first introduced in early 2000s with the use of sublimed tetracene as the organic light emitting material. [78, 84, 140] Since then, unipolar OLETs have improved by following different strategies, such as the application of asymmetric electrodes, shortening the channel dimensions of the device and by incorporating bilayer transporting layers. [141] The first ambipolar OLETs were based on active layers of PPV derivatives via solution processing, where the recombination zone could be tuned by simply varying the applied voltage in the device. [142] More recently, green light emitting OLETs were fabricated from poly(9,9-dioctylfluorene-alt-benzothiadiazole) (F8BT) by modifying the source and drain electrodes with zinc oxide, reaching an external quantum efficiency of 8%.[143, 144]

Depending on the active layer that is incorporated in OLETs devices, they can either be unipolar or ambipolar. For the unipolar devices, exciton generation is happening close to one of the contact electrodes – the source or the drain, where for the ambipolar the recombination zone is often in the middle of the accumulation zone, where the electrons recombine with the holes. [145]Ideally for efficient OLETs, ambipolar organic semiconductors are required, as both type of carriers are present in the device channel and efficient exciton generation is occurring.

A major issue, which still remains for OLETs, is the fact that high mobility ambipolar light emitting materials are rather limited and different approaches in the device designs have to be employed. [141, 146, 147] Although significant progress has been accomplished, further development is required for OLETs in both external quantum efficiency and luminance, but also their power efficiency needs improvement. This can be achieved by optimising the organic semiconducting material to offer both balanced carrier mobility and high luminescence efficiency. Another approach is by device engineering to minimise losses and exciton quenching.

In this chapter, a polymer that has not been reported before for OLET applications is presented. This material has high charge carrier hole mobility and it is light emitting. This polymer was also blended with a high mobility small molecule to enhance its charge transport properties, without disturbing its morphology or luminescence efficiency.

7.2 Organic semiconducting materials

For OLETs, as described in Chapter 7.1, organic light emitting materials with high charge transport properties are required. For this reason, the use of the poly[[6,6,12,12-tetrakis(4-hexadecylphenyl)-6,12-dihydroindeno[1,2-b] indeno [2',1':4,5] thieno [2,3-d] thiophene-2,8-diyl]thieno[3,2-b]thiophene-2,5-diyl] (PDITTTT) [148], with Mw 242 kDa and polydispersity of 2.85, as measured by GPC against polystyrene standards, is applied in this project. This polymer hasn't been reported before for its possible application in OLETs and it has a hole charge carrier mobility of 1 cm^2/Vs. [149]

The polymer was also blended with the 2,7-dioctyl[1] -benzothieno [3,2-b[1] benzothiophene (C_8-BTBT) small molecule, in order to achieve higher change transport properties and improved thin film morphology. C_8-BTBT possess a large optical band gap (∼3.6 eV) and high hole charge carrier mobility, when deposited by sublimation (∼5 cm^2/Vs) [150]. The molecular structures of the materials used in this project, PDITTTT and C_8-BTBT, as well as their HOMO energy levels as measured by the KP technique, are presented in Figure 7.1.

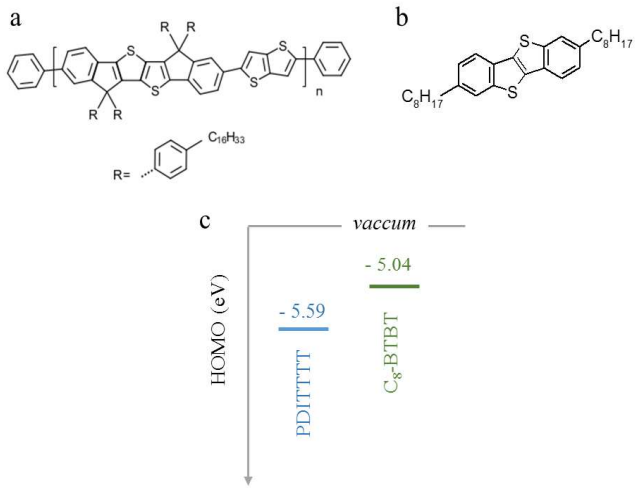


Figure 7.1: Chemical structures of (a) PDITTTT & (b) C_8-BTBT and (c) their HOMO energy level.

7.2.1 Optical properties

The absorbance and the photoluminescence (PL) of PDITTT and C_8-BTBT: PDITTTT thin films before and after annealing are presented in Figure 7.2. The PL of the thin films was measured at 534 nm pumped at 405 nm.

The vibronic absorption and PL of the PDITTTT films (Figure 7.2a) do not show high levels of disorder and thus its long side chains are not impacting the planarity

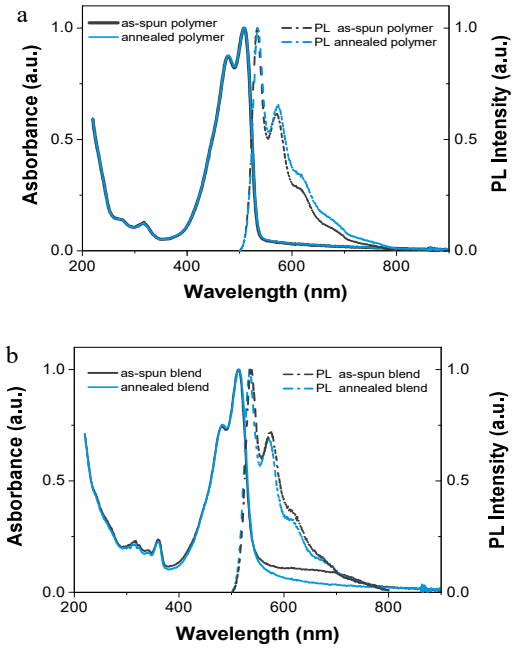


Figure 7.2: Normalised absorption spectra and photoluminescence (PL) for (a) PDITTTT polymer and (b) C_8-BTBT: PDITTTT blend films. The solid lines (left ordinate) are absorption and the dashed lines (right ordinate) PL, with black for as spin-coated and blue for post-annealing.

of the polymer molecules. The structure of the C_8-BTBT:PDITTT blend, as seen in Figure 7.2b, is not affected by the C_8-BTBT addition. However, the scattering tail seen in the 'as-spun' C_8-BTBT:PDITTT absorbance can be attributed to a rougher film surface, which then decreases once the film has been annealed.

The photoluminescence quantum efficiency (PLQE) was also measured for the PDITTTT and C_8-BTBT:PDITTTT films. In order to investigate the contribution of C_8-BTBT to the PLQE of the system, the blending ratio of the small molecule to the polymer was varied. For the PLQE measurements and data analysis, the de Mello method was applied, which involves direct, indirect and blank excitation.[156] The photoluminescence quantum efficiency (Figure 7.3) of PDITTTT is 11.7% and for C_8-BTBT:PDITTTT varies from 10-13.3% depending on the concentration of polymer. The highest PLQE value was observed when 75% of the blend was PDITTTT.

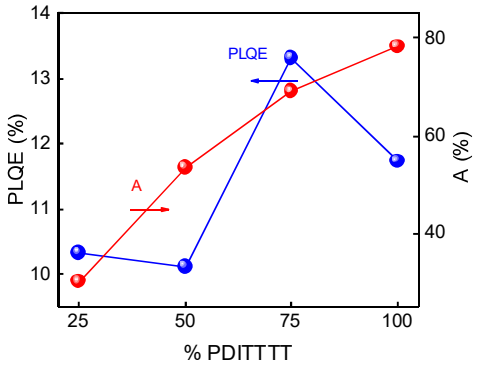


Figure 7.3: PLQE and absorption of the thin films by varying the concentration of the polymer PDITTTT in the small molecule:polymer blend.

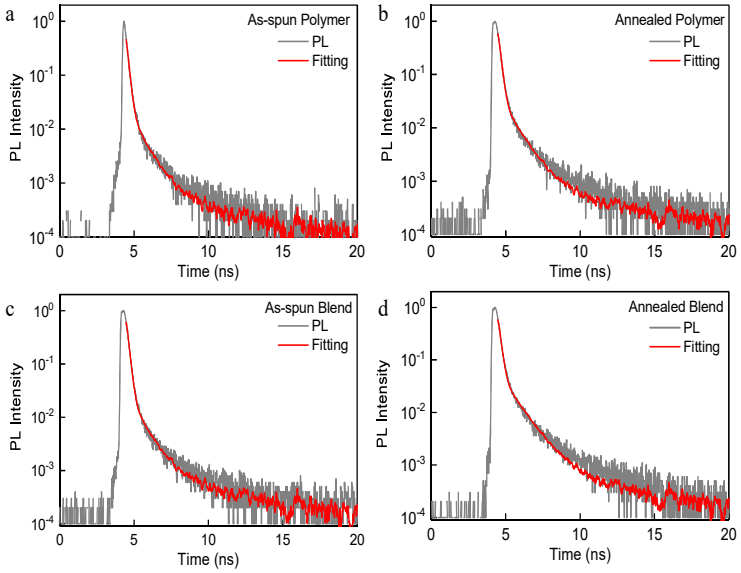


Figure 7.4: Normalised time-resolved PL (537 nm, pumped at 405 nm) for PDITTTT polymer (a) as-spun and (b) annealed and for the C_8-BTBT: PDITTTT blend films (c) as-spun and (d) annealed.

In order to gain a better understanding of the optical properties of the organic semiconductors, time resolved PL was performed in polymer and blended thin films. PL (pumped at 405 nm) pulsed studies were conducted before and after annealing the thin films at 120°C, and the data presented in Figure 7.4. A bi-exponential decay was observed with slightly longer decay times for the C_8-BTBT: PDITTTT blend than the PDITTTT polymer, whose values are presented in Table 7.1.

Table 7.1: Decay time as extracted by fitting the experimental data of the time-resolved PL for the PDITTTT and C_8-BTBT: PDITTTT films before and after annealing (120°C).

Decay time	PDITTTT		C8-BTBT:PDITTTT	
	As spun	Annealed	As spun	Annealed
τ_1 (ns)	0.05	0.08	0.09	0.07
τ_2 (ns)	0.78	0.89	1.00	0.80

7.2.2 Thin film morphology

The microstructure of the thin films was studied by Atomic Force Microscopy (AFM) and X-Ray Diffraction (XRD) measurements. Thin films on glass substrates were prepared for both techniques annealed at 120°C. Figure 7.5 show the topography images from the PDITTTT and C_8-BTBT: PDITTTT blend as well as their height distribution, as extracted from the AFM scans.

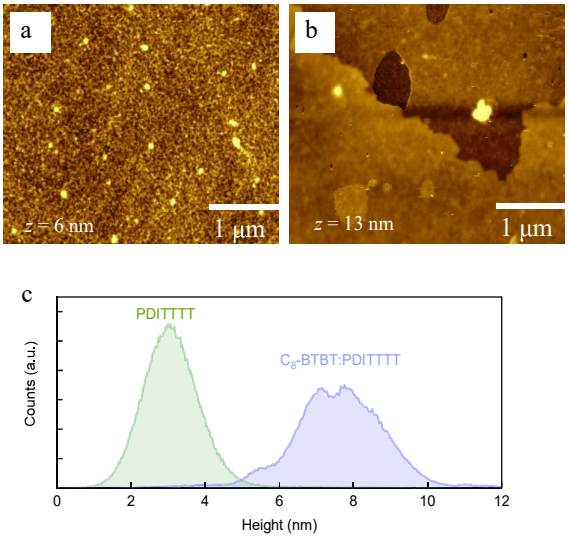


Figure 7.5: AFM topography images for (a) PDITTTT and (b) C_8-BTBT: PDITTTT. (c) Their height distribution as extracted from (a) & (b).

The polymer (Figure 7.5a) seems to be very smooth with surface roughness of 0.8 nm, large disorder and no evidence of crystallinity in the film. On the other hand, the film of the blend (Figure 7.5b) appeared to be highly crystalline due to the small molecule phase separated in the first few nanometers. The film roughness as extracted from the topographic images is 1.2 nm, with crystalline plateaus of $\sim$ 1nm. These results are in accordance with the scattering observed in the absorption spectra in the film of the blend (Figure 7.2b), due to rougher surface film.

X-Ray diffraction patterns were recorded for the organic semiconducting compounds

and their blend. As seen in Figure 7.6 the PDITTTT does not show evidence of diffraction peaks, as the polymer is amorphous.

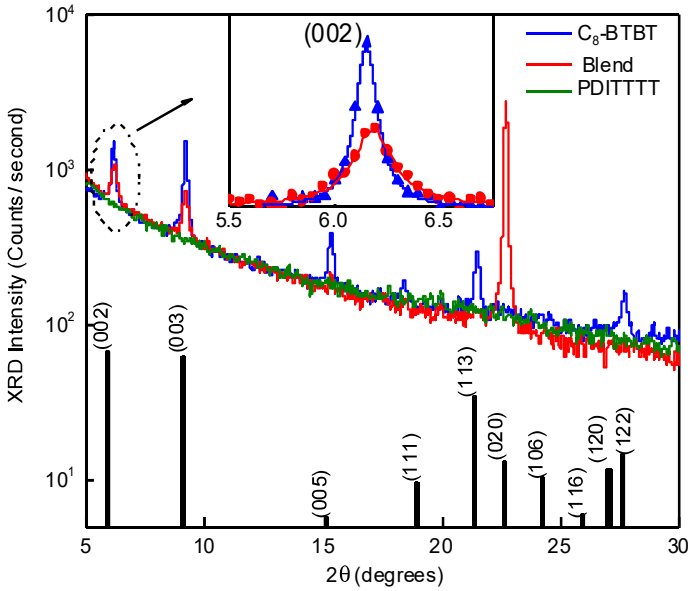


Figure 7.6: X-Ray diffraction pattern for C_8-BTBT, PDITTTT and the C_8-BTBT: PDITTTT blend. Peak position of C_8-BTBT according to previously reported values. [151]

On the other hand, the C_8-BTBT small molecule is highly crystalline with strong diffraction peaks at 6° and 9° which correspond to the (00h) planes, which is in accordance with previous reported C_8-BTBT XRD pattern.[151] For the C_8-BTBT: PDITTTT blend the existence of the (020) peak is observed, which is usually manifested under strain. [152] This is also confirmed by the shift of the (002) peak upon blending, as shown in the inset of Figure 7.6, which indicates a substantial deformation of the C_8-BTBT crystals. The shift is accompanied by changes in the profile of this peak, which are related to reduced strain and increased broadening.

In order to quantify the XRD results, the (002) peaks were fitted with the Voigt profile, which is a convolution of a Lorentz and a Gauss function. The Lorentzian contribution is associated with the vertical size grain size (G_z), while the Gaussian contribution is related to microstrain (ϵ_s). Microstrain in the films is attributed to structural defects and the microscopic strain field around them. The microstrain was found to be exceptionally small and similar across both samples, suggesting that the deformation of C_8-BTBT within the blend is of a hydrostatic nature and does not cause any additional structural defects. In addition, G_z was calculated to be 69 and 38 nm for pure C_8-BTBT and the blend, respectively. Given that the lateral lamellar size is

not affected by blending, it seems that the polymer is distributed in between of the wide C_8-BTBT lamellae along the z-direction resembling an intercalation process.

7.3 Organic semiconducting devices

7.3.1 OTFTs

Organic semiconducting devices were fabricated to evaluate the charge transport and electrical properties of the PDITTTT polymer. To begin with, thin film transistors (OTFTs) were fabricated from PDITTTT and C_8-BTBT: PDITTTT blends in different blending ratios. The best performing OTFTs resulted by blending the organic semiconductors in 1:3 ratio of small molecule to polymer. OTFTs in bottom-contact top-gate configuration were fabricated as described in Chapter 3, as this device configuration is more suitable when organic semiconducting blends are used, due to the phase separation that is occurring in the blends. The device structures for both polymer and small molecule:polymer blend OTFTs are presented in Figure 7.7. For the OTFTs, gold source-drain electrodes were treated with a self-assembled monolayer (SAM). The organic semiconducting layer and the dielectric were deposited by spin coating in a nitrogen filled glovebox. The device fabrication was completed with the deposition of aluminium to form the gate for the devices.

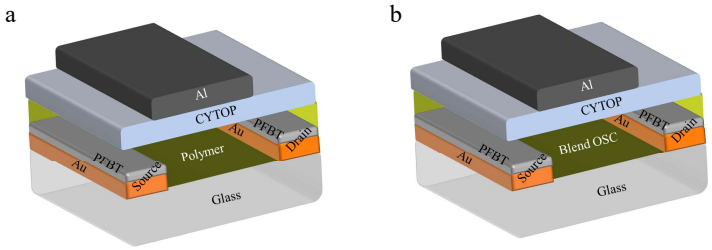


Figure 7.7: Device structure for bottom-contact top-gate (BC-TG) OTFTs for the (a) polymer PDITTTT and (b) C_8-BTBT:PDITTTT blend devices.

Representative transfer and output curves of the bottom-contact top-gate (BC-TG) OTFTs with PDITTTT and C_8-BTBT:PDITTTT (1:3) blend are presented in Figure 7.8. The PDITTTT OTFTs show excellent hysteresis-free p-channel operation in both liner (V_D =-20 V) and saturation regime (V_D =-100 V) with charge carrier mobility of 0.7 and 1 cm^2/Vs, respectively. The devices exhibit a low threshold voltage ($V_T \sim$ -18V as extracted from 10 devices) and high current ON/OFF ratio ($I_{ON/OFF} \sim 10^5$). For the C_8-BTBT:PDITTTT devices higher charge carrier mobilities was extracted from both linear (1.1 cm^2/Vs) and saturation (1.6 cm^2/Vs) regime on average from

10 devices. The OTFTs had channel dimensions of 50 μm length and 1000 μm width. As expected blending the PDITTTT polymer with C_8-BTBT enhances the charge transport properties of the semiconductor.

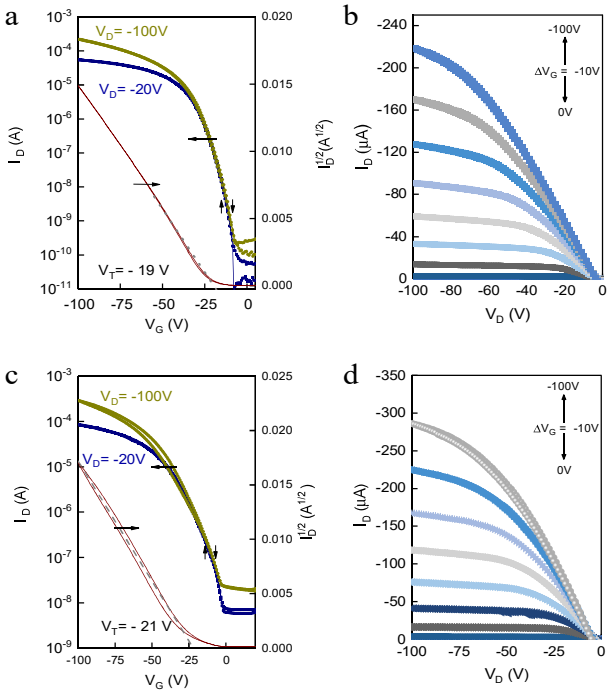


Figure 7.8: Transfer (a&c) and output (b&d) curves for (a&b) PDITTTT and (c&d) C_8-BTBT:PDITTTT BC-TG OTFTs.

7.3.2 OLETs

In a similar manner, organic light emitting transistors (OLETs) were fabricated in bottom-contact top-gate configuration as presented in Figure 7.9. For the OLET devices asymmetric electrodes, metals with different workfunction, were used in order to achieve balanced carrier injection.

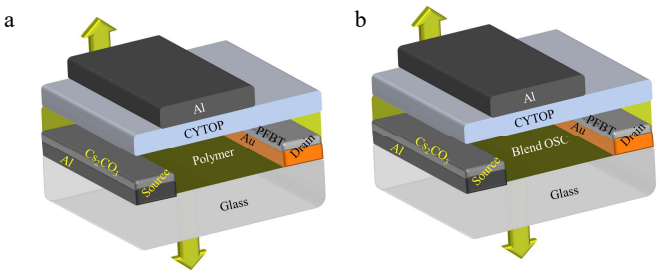


Figure 7.9: Device structure for bottom-contact top-gate (BC-TG) OLETs for the (a) polymer PDITTTT and (b) C_8-BTBT:PDITTTT blend devices.

Gold electrodes were treated with a self-assembled monolayer (SAM) which were used for hole injection, whilst a bilayer of caesium carbonate/ silver were used as the electron injection electrode. The organic and the dielectric layer were then deposited by spin-coating followed by thermal annealing. The devices were completed with 10 nm of aluminium as the gate electrode; further experimental details on the device fabrication and solution processing are presented in Chapter 4.1.6.

Representative transfer and output curves for the pure PDITTTT and blend C_8–BTBT:PDITTTT OLETs are presented in Figure 7.10. As can be seen, the OLET devices exhibit p-type operation only, however electron injection from the Cs_2CO_3/Ag electrode into the LUMO of the organic semiconductor occurred since light emission was observed. The PDITTTT OLETs have on average 0.4 and 0.8 cm^2/Vs linear and saturation mobilities with a threshold voltage of –45 V. The C_8-BTBT:PDITTTT OLETs have hole mobility of 2.3 and 3.6 cm^2/Vs on average for the linear and saturation regimes, respectively. Transfer and output characteristics of the OLET devices exhibit similar behaviour with the OTFTs (Figure 7.8) as fabricated from the same materials.

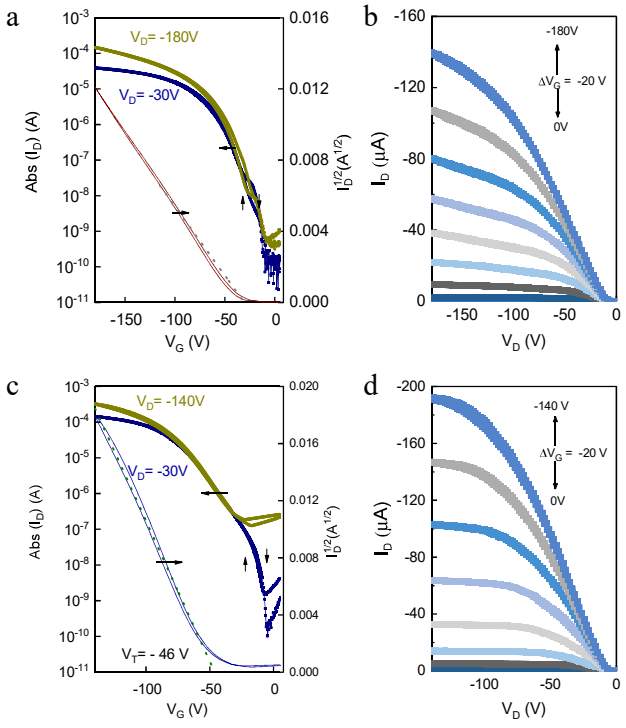


Figure 7.10: Transfer (a&c) and output (b&d) curves for (a&b) PDITTTT and (c&d) C_8-BTBT:PDITTTT BC-TG OLETs.

7.3.3 Device Characterisation

Since OLETs had no significant differences from the OTFTs, despite the use of different metals for electrodes, the devices showed good charge transport in the p-type region. The electrical and optical characteristics of the devices were then measured by combining an Agilent B2902A semiconductor analyser and a probe station fitted with two calibrated photodiodes positioned below and above the active region of the OLETs. The luminance of the OLETs was determined from the photodiode current and the emission zone was calculated from the intensity profiles of the microscopic images of the OLETs. Finally, the external quantum efficiency (EQE) was calculated using the photocurrent, the source- drain current and the emission spectrum under the assumption that the emission is Lambertian. [141, 153]

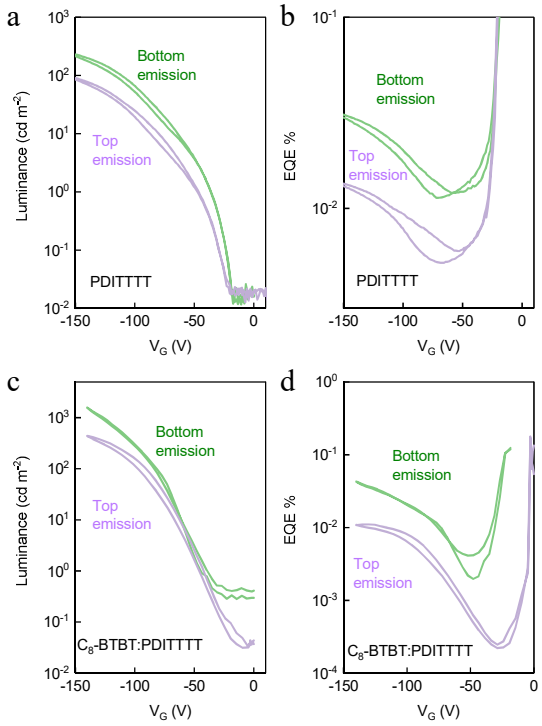


Figure 7.11: Luminance and EQE voltage dependence for the PDITTTT (polymer) and C_8-BTBT:PDITTTT (blend) OLET devices. Both top (black) and bottom (red) emission is showed.

Figures 7.11a&b shows the luminance (cd m^{-2}) and external quantum efficiency (EQE) for the PDITTTT as a function of the gate voltage (V_G). An increase in the luminance (L= 100 cd m^{-2}) is observed at V_G = -150 V with EQE= 3.1x10^{-2}% for the bottom emission, whereas L=300 cd m^{-2} at V_G = -150 V with the same EQE was observed for the top emission. The better performance of the latter is mainly due to the difference between the transmittance of the glass substrate and the semi-transparent aluminium electrode. Luminance and EQE are higher in the case of C_8-

BTBT:PDITTTT blend OLETs, as seen in Figures 7.11c&d. For the top emission, luminance is at 500 cd m^{-2} with EQE= 1x10^{-2}%, whereas L$\sim$ 1700 cd m^{-2} with EQE= 3.1x10^{-2}% for the bottom emission. The maximum current density for the PDITTTT devices was found to be 1.6 A/cm^2, whereas 3.6 A/cm^2 for the blend OLETs, which indicates that the blended devices have better optical performance than the polymer only devices.

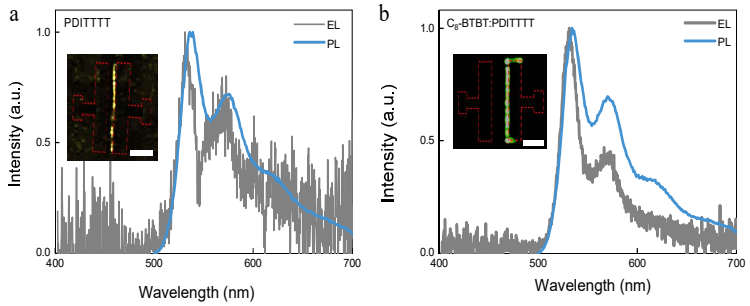


Figure 7.12: Photoluminescence and electroluminescence spectra for (a) PDITTTT and (b) C_8-BTBT:PDITTTT thin films, along with the microscope images of their emission zone (scale bar: 250 μm)

The emission zone of the devices appeared to be close to the electron injecting electrode as a narrow zone, which does not move in the middle of the channel. This observation is attributed to the unipolarity of the organic semiconductors. The emission zone was calculated by measuring the intensity profiles of the images, as recorded from the microscope (inset of Figure 7.12). The emission zone of the PDITTTT OLETs was found to be $\sim$6 μm, whereas for the C_8-BTBT:PDITTTT found to be $\sim$14 μm. The photoluminescence (PL) and electroluminescence (EL) were measured from the top-emission of the PDITTTT and C_8-BTBT:PDITTTT OLET devices, as presented in Figure 7.12. Vibronic emission is observed from both materials with peak at 531 nm, with a good matching of their PL spectra.

Since the organic semiconducting polymer and the blend are both p-type materials the light emission is happening close to the drain electrode, as expected. The operating principle of the light emitting devices is presented in Figure 7.13. The application of negative gate (V_G) drain voltage (V_D) injects holes from the gold electrode, which are then accumulated at the semiconductor-dielectric interface and they are travelling in the channel of the device. Electrons, on the other hand, are injected from the aluminium electrode which then recombine with the holes. Electrons in this case are the majority charge carrier in the channel, since the organic semiconductors are p-type. Due to this fact, the exciton formation and light emission is occurring near the aluminium electrode of the device.

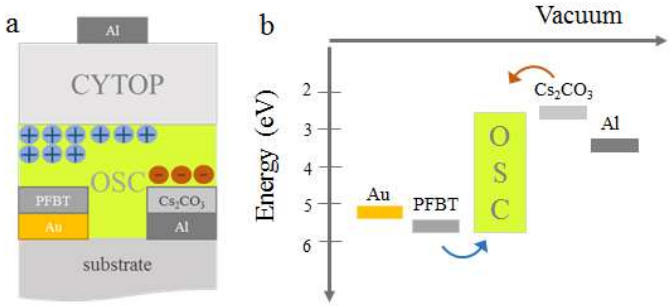


Figure 7.13: OLET (a) structure and (b) charge transfer mechanism.

7.4 Summary

In this chapter, the application of light emitting transistors (OLETs) is investigated from a polymer and a small molecule:polymer blend of organic semiconductors. In particular for this project, a p-type polymer is presented as a good candidate for OLET application, since it combines both good charge carrier mobility and effective light emission. The charge transport properties of the polymer and blend were investigated via the fabrication of thin film transistors, which showed charge carrier mobilities of 1 and 1.6 cm^2/Vs in the linear and saturation regimes, respectively. OLETs were employed in the same configuration resulting in devices with an enhanced charge carrier mobility of 3.6 cm^2/Vs, which is significantly higher than any previously reported polymer OLET. Devices with green light emission and brightness of 1700 cd m^{-2} and quantum efficiency of $\sim 10^{-2}$% were achieved by employing asymmetric electrodes. These findings highlight the use of a high mobility light emitting material that has not been reported before.

Chapter 8

Conclusion & Future Work

The thesis is focused on organic semiconductors for solution processed thin film transistors. A generic approach to enhance the charge transport properties of the semiconductors is via the addition of molecular dopants. Doping the organic semiconductors in order to increase the charge carrier mobility and improve the overall performance of the device was demonstrated for both p and n-type transistor devices.

A Lewis acid $B(C_6F_5)_3$ was demonstrated as an effective p-type dopant for organic small molecule, polymers and their blends. Similar patterns were observed in all the organic semiconductors which were tested, including a significant increase in the hole mobility, increase in the off-current of the device, reduction in both the threshold voltage and contact resistance of the transistors. The doping was also verified by the shift of the workfunction level towards the HOMO upon dopant addition in the semiconductors. Furthermore, $B(C_6F_5)_3$ induced long-range molecular terracing in certain systems. According to their energy levels, as calculated from DFT, integer charge transport is not a possible doping mechanism due to the mismatch of their energy levels, whereas charge transfer complex formation between $B(C_6F_5)_3$ and certain elements of the semiconductors is more feasible. The understanding of the doping mechanism between $B(C_6F_5)_3$ and several organic semiconductors is under study through collaboration between theoretical physicists and spectroscopists collaborators. As future steps, thin film transistors should be measured under low temperatures, in order to study the charge transport mechanism of the doped systems. Furthermore, $B(C_6F_5)_3$ should be explored in other electronic devices, such as the addition in the hole transporting layer of the solar cell.

There is extensive progress in p-type organic semiconductors, whereas research on n-type OSCs is rather limited. Doping n-type semiconductors is rather challenging, due to the requirement of the energy level of the dopant. In this thesis, DMBI-BDZC is presented as an effective n-type dopant, which was tested on an n-type small molecule and polymer. According to DFT calculations, their energy level predictions show that integer transfer from the dopant to the organic semiconductor is possible. The existence

of unpaired electrons in the doped organic films was verified by electron paramagnetic resonance measurements. To evaluate this theory, thin film transistors were fabricated from both the polymer and the small molecule. In particular dopant addition resulted in an increase in the electron mobility and reduction in the threshold voltage, contact resistance and activation energy. The thin film morphology analysis showed that the polymer was not disrupted by the dopant, whereas some minor influences in the packing of the small molecule were noted. Overall, this work demonstrates DMBI-BDZC as a new n-type dopant for organic semiconductors. Further investigation on the morphology of the doped layer is required in order to understand the impact of DMBI-BDZC in the organic semiconducting layer.

Lastly, a single polymer layer light emitting transistor was demonstrated. This was achieved by using a polymer with high charge transport properties and light emission. The device was further enhanced with the use of a small molecule: polymer blend, the small molecule was added in order to further enhance the mobility of the device. Green light emission was achieved with modest brightness and internal quantum efficiency. These results suggest that the incorporation of organic semiconducting blends for numerous opto-electronic applications will further improve the field. The device architecture requires further optimisation in order to enhance the light efficiency, as well as the organic semiconductor. For instance, replacing the C_8-BTBT with other small molecules or polymer materials, and/or using different solvents.

Bibliography

[1] Over 50 Years of Moore's Law, 2019.

[2] Julius Edgar Lilienfeld. Method and apparatus for controlling electric currents, oct 1926.

[3] Julius Edgar Lilienfeld. Amplifier for Electric Currents, dec 1932.

[4] Julius Edgar Lilienfeld. Methods and apparatus for controlling electric currents, 1930.

[5] J. Bardeen and W. H. Brattain. Physical Principles Involved in Transistor Action. *Bell System Technical Journal*, 28(2):239–277, apr 1949.

[6] J. Bardeen and W. H. Brattain. The transistor, a semi-conductor triode, jul 1948.

[7] Nobelprize.org. The Nobel Prize in Physics 1956, 2003.

[8] The Transistor Computer (Digital 60), 1998.

[9] P.K. Weimer. The TFT A New Thin-Film Transistor. *Proceedings of the IRE*, 50(6):1462–1469, 1962.

[10] T. P. Brody, Juris A. Asars, and G. Douglas Dixon. A 6 X 6 Inch 20 Lines-per-Inch Liquid-Crystal Display Panel. *IEEE Transactions on Electron Devices*, 20(11):995–1001, nov 1973.

[11] P.G. le Comber, W.E. Spear, and A. Ghaith. Amorphous-silicon field-effect device and possible application. *Electronics Letters*, 15(6):179, 2007.

[12] K. Kawasaki S. Hotta, S. Nagata, Y. Miyata, K. Yokoyama, K. Adadachi, T. Chikamura, M. Yoshiyama, A. Nishikawa. Full Color Multi-Gap LC-TV Display Panel Addressed by a-Si TFTs. In *SID International Symposium, Digest of Technical Papers*, pages 296–297, 1986.

[13] E. Fortunato, P. Barquinha, and R. Martins. Oxide semiconductor thin-film transistors: A review of recent advances, jun 2012.

[14] Zachary A. Lamport, Hamna F. Haneef, Sajant Anand, Matthew Waldrip, and Oana D. Jurchescu. Tutorial: Organic field-effect transistors: Materials, structure and operation. *Journal of Applied Physics*, 124(7):071101, 2018.

[15] H. Koezuka, A. Tsumura, and T. Ando. Field-effect transistor with polythiophene thin film. *Synthetic Metals*, 18(1-3):699–704, feb 1987.

[16] Hanying Li, Benjamin C-K. Tee, Judy J. Cha, Yi Cui, Jong Won Chung, Sang Yoon Lee, and Zhenan Bao. High-Mobility Field-Effect Transistors from Large-Area Solution-Grown Aligned C ₆₀ Single Crystals. *Journal of the American Chemical Society*, 134(5):2760–2765, feb 2012.

[17] Stuart R. Thomas, Pichaya Pattanasattayavong, and Thomas D. Anthopoulos. Solution-processable metal oxide semiconductors for thin-film transistor applications. *Chemical Society Reviews*, 42(16):6910–6923, jul 2013.

[18] Alexandra F. Paterson and Thomas D. Anthopoulos. Enabling thin-film transistor technologies and the device metrics that matter, dec 2018.

[19] Apple Inc. iPhone XS - Apple, 2018.

[20] FlexEnable. Flexible displays for automotive applications, 2019.

[21] Sarah Yang. *Organic electronics could lead to cheap, wearable medical sensors.* 2014.

[22] LG. LG OLED TVs, 2019.

[23] • IoT: number of connected devices worldwide 2012-2025 — Statista, 2016.

[24] Anna Köhler and Heinz Bässler. *Electronic Process in Organic Semiconductors: An Introduction.* Wiley-VCH, 2015.

[25] Veaceslav Coropceanu, Jérôme Cornil, Demetrio A Da, Silva Filho, Yoann Olivier, Robert Silbey, and Jean-Luc Brédas. Charge Transport in Organic Semiconductors. *Chem. Rev.*, 107:926–952, 2006.

[26] Brutting Wolfgang. *Physics of Organic Semiconductors.* Wiley-VCH, 2005.

[27] N. F. Mott and Davis Edward Arthur. *Electronic processes in non-crystalline materials.* Oxford: Clarendn Press, 1979.

[28] Nianduan Lu, Ling Li, Writam Banerjee, Pengxiao Sun, Nan Gao, and Ming Liu. Charge carrier hopping transport based on Marcus theory and variable-range hopping theory in organic semiconductors. *Journal of Applied Physics*, 118(4):045701, jul 2015.

[29] Simon Hunter, Jihua Chen, and Thomas D. Anthopoulos. Microstructural Control of Charge Transport in Organic Blend Thin-Film Transistors. *Advanced Functional Materials*, 24(38):5969–5976, 2014.

[30] Martin Schwarze, Christopher Gaul, Reinhard Scholz, Fabio Bussolotti, Andreas Hofacker, Karl Sebastian Schellhammer, Bernhard Nell, Benjamin D Naab, Zhenan Bao, Donato Spoltore, Koen Vandewal, Johannes Widmer, Satoshi Kera, Nobuo Ueno, Frank Ortmann, and Karl Leo. Molecular parameters responsible for thermally activated transport in doped organic semiconductors. *Nature Materials*, 18:242–248, 2019.

[31] David Kiefer, Renee Kroon, Anna I Hofmann, Hengda Sun, Xianjie Liu, Alexander Giovannitti, Dominik Stegerer, Alexander Cano, Jonna Hynynen, Liyang Yu, Yadong Zhang, Dingqi Nai, Thomas F Harrelson, Michael Sommer, Adam J Moulé, Martijn Kemerink, Seth R Marder, Iain McCulloch, Mats Fahlman, Simone Fabiano, and Christian Müller. Double doping of conjugated polymers with monomer molecular dopants. *Nature Materials*, 18:149–155, 2019.

[32] R. A. Street, J. E. Northrup, and A. Salleo. Transport in polycrystalline polymer thin-film transistors. *Physical Review B*, 71(16):165202, 2005.

[33] Yong Sheng Zhao, Hongbing Fu, Aidong Peng, Ying Ma, Debao Xiao, and Jiannian Yao. Low-dimensional nanomaterials based on small organic molecules: Preparation and optoelectronic properties, aug 2008.

[34] Alexandra F. Paterson, Saumya Singh, Kealan J. Fallon, Thomas Hodsden, Yang Han, Bob C. Schroeder, Hugo Bronstein, Martin Heeney, Iain McCulloch, and Thomas D. Anthopoulos. Recent Progress in High-Mobility Organic Transistors: A Reality Check. *Advanced Materials*, 30(36):1801079, sep 2018.

[35] G. Barbarella, M. Melucci, and G. Sotgiu. The Versatile Thiophene: An Overview of Recent Research on Thiophene-Based Materials. *Advanced Materials*, 17(13):1581–1593, jul 2005.

[36] Michael L. Chabinyc, Leslie H. Jimison, Jonathan Rivnay, and Alberto Salleo. Connecting Electrical and Molecular Properties of Semiconducting Polymers for Thin-Film Transistors. *MRS Bulletin*, 33(7):683–689, jul 2008.

[37] Iain McCulloch, Martin Heeney, Clare Bailey, Kristijonas Genevicius, Iain MacDonald, Maxim Shkunov, David Sparrowe, Steve Tierney, Robert Wagner, Weimin Zhang, Michael L. Chabinyc, R. Joseph Kline, Michael D. McGehee, and Michael F. Toney. Liquid-crystalline semiconducting polymers with high charge-carrier mobility. *Nature Materials*, 5(4):328–333, apr 2006.

[38] Beng S. Ong, Yiliang Wu, Ping Liu, and Sandra Gardner. High-Performance Semiconducting Polythiophenes for Organic Thin-Film Transistors. *Journal of American Chemistry Society*, 126:3378–3379, 2004.

[39] Xinran Zhang, Hugo Bronstein, Auke J. Kronemeijer, Jeremy Smith, Youngju Kim, R. Joseph Kline, Lee J. Richter, Thomas D. Anthopoulos, Henning Sirringhaus, Kigook Song, Martin Heeney, Weimin Zhang, Iain McCulloch, and Dean M. DeLongchamp. Molecular origin of high field-effect mobility in an indacenodithiophene–benzothiadiazole copolymer. *Nature Communications*, 4(1):2238, oct 2013.

[40] Hoi Nok Tsao, Don M. Cho, Insun Park, Michael Ryan Hansen, Alexey Mavrinskiy, Do Y. Yoon, Robert Graf, Wojciech Pisula, Hans Wolfgang Spiess, and Klaus Muullen. Ultrahigh Mobility in Polymer Field-Effect Transistors by Design. *Journal of the American Chemical Society*, 133(8):2605–2612, mar 2011.

[41] He Yan, Zhihua Chen, Yan Zheng, Christopher Newman, Jordan R. Quinn, Florian Dotz, Marcel Kastler, and Antonio Facchetti. A high-mobility electron-transporting polymer for printed transistors. *Nature*, 457(7230):679–686, feb 2009.

[42] Dongyoon Khim, Alessandro Luzio, Giorgio Ernesto Bonacchini, Giuseppina Pace, Mi-Jung Lee, Yong-Young Noh, and Mario Caironi. Uniaxial Alignment of Conjugated Polymer Films for High-Performance Organic Field-Effect Transistors. *Advanced Materials*, 30(20):1705463, may 2018.

[43] Hagen Klauk, Marcus Halik, Ute Zschieschang, Florian Eder, Günter Schmid, and Christine Dehm. Pentacene organic transistors and ring oscillators on glass and on flexible polymeric substrates. *Applied Physics Letters*, 82(23):4175–4177, jun 2003.

[44] Chris D Sheraw, Thomas N Jackson, Dave L Eaton, and John E Anthony. Functionalized Pentacene Active Layer Organic Thin-Film Transistors. *Advanced Functional Materials*, 15(23):2009–2011, 2003.

[45] John E. Anthony, David L. Eaton, , and Sean R. Parkin. A Road Map to Stable, Soluble, Easily Crystallized Pentacene Derivatives. *Organic Letters*, 4(1):15–18, 2001.

[46] John A. Rogers Vikram C. Sundar, Jana Zaumseil, Vitaly Podzorov, Etienne Menard, Robert L. Willett, Takao Someya, Michael E. Gershenson. Elastomeric Transistor Stamps: Reversible Probing of Charge Transport in Organic Crystals. *Science*, 303(5509):1644–1646, mar 2004.

[47] Kazuo Takimiya, Yoshihito Kunugi, Yasushi Konda, Naoto Niihara, and Tetsuo Otsubo. 2,6-Diphenylbenzo[1,2-b:4,5-b‘]dichalcogenophenes: A New Class of High-Performance Semiconductors for Organic Field-Effect Transistors. *Journal of American Chemistry Society*, 126(16):5084–5085, 2004.

[48] Joyce G. Laquindanum, Howard E. Katz, , and Andrew J. Lovinger. Synthesis, Morphology, and Field-Effect Mobility of Anthradithiophenes. *Journal of American Chemistry Society*, 120(4):664–472, 1998.

[49] Oana D. Jurchescu, Sankar Subramanian, R. Joseph Kline, Steven D. Hudson, John E. Anthony, Thomas N. Jackson, and David J. Gundlach. Organic single-crystal field-effect transistors of a soluble anthradithiophene. *Chemistry of Materials*, 20(21):6733–6737, 2008.

[50] Sankar Subramanian, Sung Kyu Park, Sean R Parkin, Vitaly Podzorov, Thomas N Jackson, and John E Anthony. Chromophore Fluorination Enhances Crystallization and Stability of Soluble Anthradithiophene Semiconductors. *Journal of American Chemistry Society*, 130(20):6733–6737, 2008.

[51] Christian Kunkel, Christoph Schober, Johannes T Margraf, Karsten Reuter, and Harald Oberhofer. Finding the Right Bricks for Molecular Legos: A Data Mining Approach to Organic Semiconductor Design. *Chemistry of Materials*, 31:969–978, 2019.

[52] Wenwen Shi, Wei Yu, Deng Li, Doudou Zhang, Wenjun Fan, Jingying Shi, and Can Li. PTB7:PC 61 BM Bulk Heterojunction-Based Photocathodes for Efficient Hydrogen Production in Aqueous Solution. *Chemistry of Materials*, 31(6):1928–1935, 2019.

[53] Ana Claudia Arias. Vertically segregated polymer blends: Their use in organic electronics. *Polymer Reviews*, 46(1):103–125, jan 2006.

[54] Jeremy Smith, Richard Hamilton, Yabing Qi, Antoine Kahn, Donal D C Bradley, Martin Heeney, Iain McCulloch, and Thomas D. Anthopoulos. The Influence of Film Morphology in High-Mobility Small-Molecule:Polymer Blend Organic Transistors. *Advanced Functional Materials*, 20(14):2330–2337, jun 2010.

[55] Richard Hamilton, Jeremy Smith, Simon Ogier, Martin Heeney, John E. Anthony, Iain McCulloch, Janos Veres, Donal D C Bradley, and Thomas D. Anthopoulos. High-Performance Polymer-Small Molecule Blend Organic Transistors. *Advanced Materials*, 21(10-11):1166–1171, mar 2009.

[56] Jihoon Kang, Nayool Shin, Young Jang Do, Vivek M. Prabhu, and Do Y. Yoon. Structure and properties of small molecule-polymer blend semiconductors for

organic thin film transistors. *Advanced Functional Materials*, 130(37):12273–12275, 2008.

[57] Alexandra F. Paterson, Neil D. Treat, Weimin Zhang, Zhuping Fei, Gwenhivir Wyatt-Moon, Hendrik Faber, George Vourlias, Panos A. Patsalas, Olga Solomeshch, Nir Tessler, Martin Heeney, and Thomas D. Anthopoulos. Small Molecule/Polymer Blend Organic Transistors with Hole Mobility Exceeding 13 cm2/Vs. *Advanced Materials*, 28(35):7791–7798, 2016.

[58] Kui Zhao, Olga Wodo, Dingding Ren, Hadayat Ullah Khan, Muhammad Rizwan Niazi, Hanlin Hu, Maged Abdelsamie, Ruipeng Li, Er. Qiang Li, Liyang Yu, Buyi Yan, Marcia M. Payne, Jeremy Smith, John E. Anthony, Thomas D. Anthopoulos, Sigurdur T. Thoroddsen, Baskar Ganapathysubramanian, and Aram Amassian. Vertical Phase Separation in Small Molecule:Polymer Blend Organic Thin Film Transistors Can Be Dynamically Controlled. *Advanced Functional Materials*, 26(11):1737–1746, 2016.

[59] Jeremy Smith, Martin Heeney, Iain McCulloch, Jennifer Nekuda Malik, Natalie Stingelin, Donal D C Bradley, and Thomas D. Anthopoulos. Percolation behaviour in high mobility p-channel polymer/small-molecule blend organic field-effect transistors. *Organic Electronics: physics, materials, applications*, 12(1):143–147, 2011.

[60] Muhammad R. Niazi, Ruipeng Li, Er Qiang Li, Ahmad R. Kirmani, Maged Abdelsamie, Qingxiao Wang, Wenyang Pan, Marcia M. Payne, John E. Anthony, Detlef-M. Smilgies, Sigurdur T. Thoroddsen, Emmanuel P. Giannelis, and Aram Amassian. Solution-printed organic semiconductor blends exhibiting transport properties on par with single crystals. *Nature Communications*, 6:8598, 2015.

[61] Jeremy Smith, Weimin Zhang, Rachid Sougrat, Kui Zhao, Ruipeng Li, Dongkyu Cha, Aram Amassian, Martin Heeney, Iain McCulloch, and Thomas D. Anthopoulos. Solution-Processed Small Molecule-Polymer Blend Organic Thin-Film Transistors with Hole Mobility Greater than 5 cm2/Vs. *Advanced Materials*, 24(18):2441–2446, may 2012.

[62] Yaorong Su, Jiaolong Jiang, Ning Ke, Ni Zhao, Weiguang Xie, and Jianbin Xu. Low-voltage flexible pentacene thin film transistors with a solution-processed dielectric and modified copper source–drain electrodes. *Journal of Materials Chemistry C*, 1(14):2585, mar 2013.

[63] Simon G. J. Mathijssen, Martijn Kemerink, Abhinav Sharma, Michael Cölle, Peter A. Bobbert, René A. J. Janssen, and Dago M. De Leeuw. Charge trapping

at the dielectric of organic transistors visualized in real time and space. *Advanced Materials*, 20(5):975–979, mar 2008.

[64] Simon G. J. Mathijssen, Mark Jan Spijkman, Anne Marije Andringa, Paul A. Van Hal, Iain McCulloch, Martijn Kemerink, René A. J. Janssen, and Dago M. De Leeuw. Revealing buried interfaces to understand the origins of threshold voltage shifts in organic field-effect transistors. *Advanced Materials*, 22(45):5105–5109, dec 2010.

[65] Hyun Ho Choi, Moon Sung Kang, Min Kim, Haena Kim, Jeong Ho Cho, and Kilwon Cho. Decoupling the bias-stress-induced charge trapping in semiconductors and gate-dielectrics of organic transistors using a double stretched-exponential formula. *Advanced Functional Materials*, 23(6):690–696, feb 2013.

[66] Yen Hung Lin, Hendrik Faber, Stephan Rossbauer, and Thomas D. Anthopoulos. Solution-processed ZnO nanoparticle-based transistors via a room-temperature photochemical conversion process. *Applied Physics Letters*, 102(19):193516, may 2013.

[67] Guido Scavia, William Porzio, Silvia Destri, Luisa Barba, Gianmichele Arrighetti, Silvia Milita, Luca Fumagalli, Dario Natali, and Marco Sampietro. Effect of the silanization and annealing on the morphology of thin poly(3-hexylthiophene) (P3HT) layer on silicon oxide. *Surface Science*, 602(19):3106–3115, oct 2008.

[68] Tim Richards, Matthew Bird, and Henning Sirringhaus. A quantitative analytical model for static dipolar disorder broadening of the density of states at organic heterointerfaces. *Journal of Chemical Physics*, 128(23):234905, jun 2008.

[69] Janos Veres, Simon D. Ogier, Stephen W. Leeming, Domenico C. Cupertino, and Soad Mohialdin Khaffaf. Low-k insulators as the choice of dielectrics in organic field-effect transistors. *Advanced Functional Materials*, 13(3):199–204, 2003.

[70] Gilles Horowitz and Philippe Delannoy. An analytical model for organic-based thin-film transistors. *Journal of Applied Physics*, 70:469, 1991.

[71] S. M. Sze and Kwok K. NG. *Physics of Semiconductor Devices*. Hoboken, NJ, USA, 3rd edition, 2006.

[72] Sangmoo Choi, Felipe A Larrain, Cheng Yin Wang, Canek Fuentes-Hernandez, Wen Fang Chou, and Bernard Kippelen. Self-forming electrode modification in organic field-effect transistors. *Journal of Materials Chemistry C*, 4(35):8297–8303, 2016.

[73] Emily G. Bittle, James I. Basham, Thomas N. Jackson, Oana D. Jurchescu, and David J. Gundlach. Mobility overestimation due to gated contacts in organic field-effect transistors. *Nature Communications*, 7(1):10908, apr 2016.

[74] Juntao Hu, Sheng Hu, Chaochao Lu, Yang Huang, Kai Xu, and Xianghua Wang. Assistant dopant system in red phosphorescent OLEDs and its mechanism reveal. *Optical Materials*, 75:513–520, 2018.

[75] Hyun Ho Choi, Yaroslav I. Rodionov, Alexandra F. Paterson, Julianna Panidi, Danila Saranin, Nikolai Kharlamov, Sergei I. Didenko, Thomas D. Anthopoulos, Kilwon Cho, and Vitaly Podzorov. Accurate Extraction of Charge Carrier Mobility in 4-Probe Field-Effect Transistors. *Advanced Functional Materials*, 28(26):1707105, jun 2018.

[76] Alexandra F. Paterson, Saumya Singh, Kealan J. Fallon, Thomas Hodsden, Yang Han, Bob C. Schroeder, Hugo Bronstein, Martin Heeney, Iain McCulloch, and Thomas D. Anthopoulos. Recent Progress in High-Mobility Organic Transistors: A Reality Check. *Advanced Materials*, 30(36):1801079, sep 2018.

[77] Cheng-Fang Liu, Xu Liu, Wen-Yong Lai, and Wei Huang. Organic Light-Emitting Field-Effect Transistors: Device Geometries and Fabrication Techniques. *Advanced Materials*, 30(52):1802466, dec 2018.

[78] Fabio Cicoira and Clara Santato. Organic light emitting field effect transistors: Advances and perspectives. *Advanced Functional Materials*, 17(17):3421–3434, nov 2007.

[79] Jana Zaumseil and Henning Sirringhaus. Electron and ambipolar transport in organic field-effect transistors, 2007.

[80] Congcong Zhang, Penglei Chen, and Wenping Hu. Organic Light-Emitting Transistors: Materials, Device Configurations, and Operations. *Small*, 12(10):1252–1294, mar 2016.

[81] Clara Santato, Fabio Cicoira, and Richard Martel. Organic photonics: Spotlight on organic transistors. *Nature Photonics*, 5(7):392–393, jul 2011.

[82] Jana Zaumseil, Christopher R. McNeill, Matt Bird, Darryl L. Smith, P. Paul Ruden, Matthew Roberts, Mary J. McKiernan, Richard H. Friend, and Henning Sirringhaus. Quantum efficiency of ambipolar light-emitting polymer field-effect transistors. *Journal of Applied Physics*, 103(6):064517, mar 2008.

[83] Franco Dinelli, Raffaella Capelli, Maria A. Loi, Mauro Murgia, Michele Muccini, Antonio Facchetti, and Tobin J. Marks. High-mobility ambipolar transport in

organic light-emitting transistors. *Advanced Materials*, 18(11):1416–1420, jun 2006.

[84] Aline Hepp, Holger Heil, Wieland Weise, Marcus Ahles, Roland Schmechel, and Heinz Von Seggern. Light-Emitting Field-Effect Transistor Based on a Tetracene Thin Film. *Physical Review Letters*, 91(15):157406, 2003.

[85] Hideki Shirakawa, Edwin J. Louis, Alan G. MacDiarmid, Chwan K. Chiang, and Alan J. Heeger. Synthesis of electrically conducting organic polymers: Halogen derivatives of polyacetylene, (CH)x. *Journal of the Chemical Society, Chemical Communications*, (16):578–580, 1977.

[86] A J Heeger, S Kivelson, J R Schrieffer, and W. P Su. Solitons in conducting polymers. *Reviews of Modern Physics*, 60(3):781–850, 1988.

[87] Jianhui Hou, Olle Inganäs, Richard H. Friend, and Feng Gao. Organic solar cells based on non-fullerene acceptors. *Nature Materials*, 17(2):119–128, 2018.

[88] Jong Baek Park, Mehmet Isik, Hea Jung Park, In Hwan Jung, David Mecerreyes, and Do Hoon Hwang. Polystyrene-block-Poly(ionic liquid) Copolymers as Work Function Modifiers in Inverted Organic Photovoltaic Cells. *ACS Applied Materials and Interfaces*, 10(5):4887–4894, 2018.

[89] Makoto Mizukami, Seung-Il Cho, Kaori Watanabe, Miho Abiko, Yoshiyuki Suzuri, Shizuo Tokito, and Junji Kido. Flexible Organic Light-Emitting Diode Displays Driven by Inkjet Printed High Mobility Organic Thin Film Transistors. *IEEE Electron Device Letters*, 39(1):39–41, 2018.

[90] Weixuan Zeng, Hsin Yu Lai, Wei Kai Lee, Min Jiao, Yi Jiun Shiu, Cheng Zhong, Shaolong Gong, Tao Zhou, Guohua Xie, Monima Sarma, Ken Tsung Wong, Chung Chih Wu, and Chuluo Yang. Achieving Nearly 30% External Quantum Efficiency for Orange–Red Organic Light Emitting Diodes by Employing Thermally Activated Delayed Fluorescence Emitters Composed of 1,8-Naphthalimide-Acridine Hybrids. *Advanced Materials*, 30(5):1704961, 2018.

[91] I Salzmann, G Heimel, M Oehzelt, S Winkler, and N Koch. Molecular Electrical Doping of Organic Semiconductors: Fundamental Mechanisms and Emerging Dopant Design Rules. *Accounts of Chemical Research*, 49(3):370–378, 2016.

[92] Max L Tietze, Lorenzo Burtone, Moritz Riede, Björn Lüssem, and Karl Leo. Fermi level shift and doping efficiency in p-doped small molecule organic semiconductors: A photoelectron spectroscopy and theoretical study. *Physical Review B - Condensed Matter and Materials Physics*, 86(3):35320, 2012.

[93] Alexandra F. Paterson, Yen-Hung Lin, Alexander D. Mottram, Zhuping Fei, Muhammad R. Niazi, Ahmad R. Kirmani, Aram Amassian, Olga Solomeshch, Nir Tessler, Martin Heeney, and Thomas D. Anthopoulos. The Impact of Molecular p-Doping on Charge Transport in High-Mobility Small-Molecule / Polymer Blend Organic Transistors. *Advanced Electronic Materials*, 4(10):1700464, oct 2018.

[94] Alexandra F. Paterson, Neil D. Treat, Weimin Zhang, Zhuping Fei, Gwenhivir Wyatt-Moon, Hendrik Faber, George Vourlias, Panos A. Patsalas, Olga Solomeshch, Nir Tessler, Martin Heeney, and Thomas D. Anthopoulos. Small Molecule/Polymer Blend Organic Transistors with Hole Mobility Exceeding 13 cm ² V ⁻¹ s ⁻¹. *Advanced Materials*, 28(35):7791–7798, sep 2016.

[95] Henry Mendez, Georg Heimel, Stefanie Winkler, Johannes Frisch, Andreas Opitz, Katrein Sauer, Berthold Wegner, Martin Oehzelt, Christian Rothel, Steffen Duhm, Daniel Tobbens, Norbert Koch, and Ingo Salzmann. Charge-transfer crystallites as molecular electrical dopants. *Nature Communications*, 6:8560, 2015.

[96] Henry Mendez, Georg Heimel, Andreas Opitz, Katrein Sauer, Patrick Barkowski, Martin Oehzelt, Junshi Soeda, Toshihiro Okamoto, Jun Takeya, Jean-baptiste Arlin, Jean-Yves Balandier, Yves Geerts, Norbert Koch, Ingo Salzmann, Henry Mondez, Georg Heimel, Andreas Opitz, Katrein Sauer, Patrick Barkowski, Martin Oehzelt, Junshi Soeda, Toshihiro Okamoto, Jun Takeya, Jean-baptiste Arlin, Yves Balandier, Yves Geerts, Norbert Koch, and Ingo Salzmann. Doping of Organic Semiconductors : Impact of Dopant Strength and Electronic Coupling Angewandte. *Angewandte Chemie-International Edition*, 52(20061):7751–7755, 2013.

[97] Ingo Salzmann, Georg Heimel, Steffen Duhm, Martin Oehzelt, Patrick Pingel, Benjamin M George, Alexander Schnegg, Klaus Lips, Ralf-Peter Blum, Antje Vollmer, and Norbert Koch. Intermolecular Hybridization Governs Molecular Electrical Doping. *Physical Review Letters*, 108(3):35502, 2012.

[98] E. F. Aziz, A. Vollmer, S. Eisebitt, W. Eberhardt, P. Pingel, D. Neher, and N. Koch. Localized Charge Transfer in a Molecularly Doped Conducting Polymer. *Advanced Materials*, 19(20):3257–3260, sep 2007.

[99] Yang Han, George Barnes, Yen Hung Lin, Jaime Martin, Mohammed Al-Hashimi, Siham Y. Alqaradawi, Thomas D. Anthopoulos, and Martin Heeney. Doping of Large Ionization Potential Indenopyrazine Polymers via Lewis Acid Complexation with Tris(pentafluorophenyl)borane: A Simple Method for Improv-

ing the Performance of Organic Thin-Film Transistors. *Chemistry of Materials*, 28(21):8016–8024, 2016.

[100] Peng Wei, Joon Hak Oh, Guifang Dong, and Zhenan Bao. Use of a 1H-benzoimidazole derivative as an n-type dopant and to enable air-stable solution-processed n-channel organic thin-film transistors. *Journal of the American Chemical Society*, 132(26):8852–8853, 2010.

[101] S. Kobayashi, T. Nishikawa, T. Takenobu, S. Mori, T. Shimoda, T. Mitani, H. Shimotani, N. Yoshimoto, S. Ogawa, and Y. Iwasa. Control of carrier density by self-assembled monolayers in organic field-effect transistors. *Nature Materials*, 3(5):317–322, may 2004.

[102] Jung Pyo Hong, Aee Young Park, Seonghoon Lee, Jihoon Kang, Nayool Shin, and Do Y. Yoon. Tuning of Ag work functions by self-assembled monolayers of aromatic thiols for an efficient hole injection for solution processed triisopropylsilylethynyl pentacene organic thin film transistors. *Applied Physics Letters*, 92(14):143311, apr 2008.

[103] Georg Heimel, Lorenz Romaner, Egbert Zojer, and Jean Luc Bredas. The interface energetics of self-assembled monolayers on metals, jun 2008.

[104] Yong Xu, Huabin Sun, Ao Liu, Hui-Hui Hui Zhu, Wenwu Li, Yen-Fu Fu Lin, and Yong-Young Young Noh. Doping: A Key Enabler for Organic Transistors. *Advanced Materials*, 30(46):1801830, nov 2018.

[105] Takeo Minari, Peter Darmawan, Chuan Liu, Yun Li, Yong Xu, and Kazuhito Tsukagoshi. Highly enhanced charge injection in thienoacene-based organic field-effect transistors with chemically doped contact. *Applied Physics Letters*, 100(9), 2012.

[106] Jun Endo, Toshio Matsumoto, and Junji Kido. Organic electroluminescent devices with a vacuum-deposited Lewis-acid-doped hole-injecting layer. *Japanese Journal of Applied Physics, Part 2: Letters*, 41(3 B), 2002.

[107] Qiao He, Munazza Shahid, Julianna Panidi, Adam V. Marsh, Wentao Huang, Matyas Daboczi, Ji-Seon Kim, Zhuping Fei, Thomas D. Anthopoulos, and Martin Heeney. A versatile star-shaped organic semiconductor based on benzodithiophene and diketopyrrolopyrrole. *Journal of Materials Chemistry C*, 7(22):6622–6629, 2019.

[108] Masataka Kano, Takeo Minari, and Kazuhito Tsukagoshi. Improvement of subthreshold current transport by contact interface modification in p -type organic field-effect transistors. *Applied Physics Letters*, 94(14):143304, apr 2009.

[109] Lay-lay Chua, Jana Zaumseil, Jui-fen Chang, and Eric C Ou. General observation of n-type field-effect behaviour in organic semiconductors. 434(March):194–199, 2005.

[110] Björn Lüssem, Chang Min Keum, Daniel Kasemann, Ben Naab, Zhenan Bao, and Karl Leo. Doped Organic Transistors. *Chemical Reviews*, 116(22):13714–13751, 2016.

[111] Max L. Tietze, Lorenzo Burtone, Moritz Riede, Björn Lüssem, and Karl Leo. Fermi level shift and doping efficiency in p-doped small molecule organic semiconductors: A photoelectron spectroscopy and theoretical study. *Physical Review B - Condensed Matter and Materials Physics*, 86(3), 2012.

[112] Y Abe, T Hasegawa, Y Takahashi, T Yamada, and Y Tokura. Control of threshold voltage in pentacene thin-film transistors using carrier doping at the charge-transfer interface with organic acceptors. *Applied Physics Letters*, 87(15):153506, 2005.

[113] Iain D Baikie, Angela C Grain, James Sutherland, and Jamie Law. Dual Mode Kelvin Probe: featuring Ambient Pressure Photoemission Spectroscopy and Contact Potential Difference. *Energy Procedia*, 60:48–56, 2014.

[114] John C. De Mello, H. Felix Wittmann, and Richard H. Friend. An improved experimental determination of external photoluminescence quantum efficiency. *Advanced Materials*, 9(3):230–232, mar 1997.

[115] Jonathan Mooney and Patanjali Kambhampati. Get the basics right: Jacobian conversion of wavelength and energy scales for quantitative analysis of emission spectra, oct 2013.

[116] Zongrui Wang, Ye Zou, Wangqiao Chen, Yinjuan Huang, Changjiang Yao, and Qichun Zhang. The Role of Weak Molecular Dopants in Enhancing the Performance of Solution-Processed Organic Field-Effect Transistors. *Advanced Electronic Materials*, 5(2):1800547, feb 2019.

[117] Jeremy Nicholas Smith. *High-performance Organic Field Effect Transistors for Large-area Microelectronics*. PhD thesis, 2010.

[118] Simon Hunter and Thomas D. Anthopoulos. Observation of Unusual , Highly Conductive Grain Boundaries in High-Mobility Phase Separated Organic Semiconducting Blend Films Probed by Lateral-Transport. *Advanced Materials*, 25(31):4320–4326, aug 2013.

[119] Elliot J Lawrence, Vasily S Oganesyan, Gregory G Wildgoose, and Andrew E Ashley. Exploring the fate of the tris(pentafluorophenyl)borane radical anion in weakly coordinating solvents. *Dalton Trans.*, 42(3):782–789, 2013.

[120] Tengling Ye, Junhai Wang, Wenbo Chen, Yulin Yang, and Dongqing He. Improved performance and reproducibility of perovskite solar cells by well-soluble tris(pentafluorophenyl)borane as a p-type dopant. *ACS Applied Materials & Interfaces*, 9(21):17923–17931, 2017.

[121] Stephan Rossbauer, Christian Muller, and Thomas D. Anthopoulos. Comparative study of the N-type doping efficiency in solution-processed fullerenes and fullerene derivatives. *Advanced Functional Materials*, 24(45):7116–7124, 2014.

[122] Dieter K. Scroder. *Semiconductor Material and Device Characterization*. Wiley-IEEE Press, Hoboken, 3 edition, 2006.

[123] Aaron B. Naden, Joachim Loos, and Donald a. MacLaren. Structure–function relations in diF-TES-ADT blend organic field effect transistors studied by scanning probe microscopy. *J. Mater. Chem. C*, 2(2):245–255, 2014.

[124] Andrew O F Jones, Basab Chattopadhyay, Yves H. Geerts, and Roland Resel. Substrate-induced and thin-film phases: Polymorphism of organic materials on surfaces. *Advanced Functional Materials*, 26(14):2233–2255, 2016.

[125] Th. H. de Keijser, J I Langford, E J Mittemeijer, and A B P Vogels. Use of the Voigt function in a single-line method for the analysis of X-ray diffraction line broadening. *Journal of Applied Crystallography*, 15(3):308–314, 1982.

[126] L. E. Koutsokeras, G. Abadias, and P. Patsalas. Texture and microstructure evolution in single-phase TixTa1-xN alloys of rocksalt structure. *Journal of Applied Physics*, 110(4):043535, 2011.

[127] Selina Olthof, Sanjeev Singh, Swagat K Mohapatra, Stephen Barlow, Seth R Marder, Bernard Kippelen, and Antoine Kahn. Passivation of trap states in unpurified and purified C-60 and the influence on organic field-effect transistor performance. *Applied Physics Letters*, 101(25), 2012.

[128] J. Blochwitz, T. Fritz, M. Pfeiffer, K. Leo, D. M. Alloway, P. A. Lee, and N. R. Armstrong. Interface electronic structure of organic semiconductors with controlled doping levels. *Organic Electronics*, 2(2):97–104, sep 2001.

[129] Yang Han, Zhuping Fei, Yen-hung Lin, Jaime Martin, Floriana Tuna, and Thomas D Anthopoulos. Anion-induced N-doping of naphthalenediimide polymer semiconductor in organic thin-film transistors. *npj Flexible Electronics*, 2(1):11, 2018.

[130] Fengjiao Zhang, Yunbin Hu, Torben Schuettfort, Chong-an Di, Xike Gao, Christopher R. McNeill, Lars Thomsen, Stefan C. B. Mannsfeld, Wei Yuan, Henning Sirringhaus, and Daoben Zhu. Critical Role of Alkyl Chain Branching of Organic Semiconductors in Enabling Solution-Processed N-Channel Organic Thin-Film Transistors with Mobility of up to 3.50 cm2 V–1 s–1. *Journal of the American Chemical Society*, 135(6):2338–2349, 2013.

[131] Jae-Min Kim, Seung-Jun Yoo, Chang-Ki Moon, Bomi Sim, Jae-Hyun Lee, Heeseon Lim, Jeong Won Kim, and Jang-Joo Kim. N-type Molecular Doping in Organic Semiconductors: Formation and Dissociation Efficiencies of Charge Transfer Complex. *The Journal of Physical Chemistry C*, page acs.jpcc.6b01175, 2016.

[132] David Kiefer, Alexander Giovannitti, Hengda Sun, Till Biskup, Anna Hofmann, Marten Koopmans, Camila Cendra, Stefan Weber, L. Jan Anton Koster, Eva Olsson, Jonathan Rivnay, Simone Fabiano, Iain McCulloch, and Christian Müller. Enhanced n-Doping Efficiency of a Naphthalenediimide-Based Copolymer through Polar Side Chains for Organic Thermoelectrics. *ACS Energy Letters*, 3(2):278–285, feb 2018.

[133] Alexandra F. Paterson, Saumya Singh, Kealan J. Fallon, Thomas Hodsden, Yang Han, Bob C. Schroeder, Hugo Bronstein, Martin Heeney, Iain McCulloch, and Thomas D. Anthopoulos. Recent Progress in High-Mobility Organic Transistors: A Reality Check. *Advanced Materials*, 30(36):1801079, sep 2018.

[134] M C J M Vissenberg and M Matters. Theory of the field-effect mobility in amorphous organic transistros. *Physical Review B*, 57(20):12964–12967, 1998.

[135] Jihong Kim, Dongyoon Khim, Kang Jun Baeg, Won Tae Park, Seung Hoon Lee, Minji Kang, Yong Young Noh, and Dong Yu Kim. Systematic Study of Widely Applicable N-Doping Strategy for High-Performance Solution-Processed Field-Effect Transistors. *Advanced Functional Materials*, 26(43):7886–7894, 2016.

[136] Selina Olthof, Shafigh Mehraeen, Swagat K. Mohapatra, Stephen Barlow, Veaceslav Coropceanu, Jean-Luc Luc Brédas, Seth R. Marder, Antoine Kahn, Jean-luc Bre, Jean-Luc Luc Brédas, Seth R. Marder, and Antoine Kahn. Solitons in conducting polymers. *Physical Review Letters*, oct 2012.

[137] Paul H. Wöbkenberg, John G. Labram, Jean-Marie Swiecicki, Ksenia Parkhomenko, Dusan Sredojevic, Jean-Paul Gisselbrecht, Dago M. de Leeuw, Donal D. C. Bradley, Jean-Pierre Djukic, and Thomas D. Anthopoulos. Ambipolar organic transistors and near-infrared phototransistors based on a solution-

processable squarilium dye. *Journal of Materials Chemistry*, 20(18):3673–3680, apr 2010.

[138] Sungho Nam, Hyemi Han, Jooyeok Seo, Myeonghun Song, Hwajeong Kim, Thomas D. Anthopoulos, Iain McCulloch, Donal D. C. Bradley, and Youngkyoo Kim. Ambipolar Organic Phototransistors with p-Type/n-Type Conjugated Polymer Bulk Heterojunction Light-Sensing Layers. *Advanced Electronic Materials*, 2(12):1600264, dec 2016.

[139] Raffaella Capelli, Stefano Toffanin, Gianluca Generali, Hakan Usta, Antonio Facchetti, and Michele Muccini. Organic light-emitting transistors with an efficiency that outperforms the equivalent light-emitting diodes. *Nature Materials*, 9(6):496–503, jun 2010.

[140] Jing Zhang, Peiyang Gu, Guankui Long, Rakesh Ganguly, Yongxin Li, Naoki Aratani, Hiroko Yamada, and Qichun Zhang. Switching charge-transfer characteristics from p-type to n-type through molecular "doping" (co-crystallization). *Chem. Sci.*, 00:1–6, 2016.

[141] Mujeeb Ullah Chaudhry, Khalid Muhieddine, Robert Wawrzinek, Jun Li, Shih-Chun Lo, and Ebinazar B. Namdas. Nano-Alignment in Semiconducting Polymer Films: A Path to Achieve High Current Density and Brightness in Organic Light Emitting Transistors. *ACS Photonics*, 5(6):2137–2144, jun 2018.

[142] Jana Zaumseil, Richard H. Friend, and Henning Sirringhaus. Spatial control of the recombination zone in an ambipolar light-emitting organic transistor. *Nature Materials*, 5(1):69–74, jan 2006.

[143] Michael C. Gwinner, Dinesh Kabra, Matthew Roberts, Thomas J.K. K. Brenner, Bodo H. Wallikewitz, Christopher R. McNeill, Richard H. Friend, and Henning Sirringhaus. Highly efficient single-layer polymer ambipolar light-emitting field-effect transistors. *Advanced Materials*, 24(20):2728–2734, may 2012.

[144] Michael C. Gwinner, Yana Vaynzof, Kulbinder K. Banger, Peter K.H. Ho, Richard H. Friend, and Henning Sirringhaus. Solution-processed zinc oxide as high-performance air-stable electron injector in organic Ambipolar light-emitting field-effect transistors. *Advanced Functional Materials*, 20(20):3457–3465, oct 2010.

[145] W. S. Christian Roelofs, Willem H. Adriaans, René A. J. Janssen, Martijn Kemerink, and Dago M. de Leeuw. Light Emission in the Unipolar Regime of Ambipolar Organic Field-Effect Transistors. *Advanced Functional Materials*, 23(33):4133–4139, sep 2013.

[146] Ifor D.W. Samuel and Graham A. Turnbull. Organic semiconductor lasers. *Chemical Reviews*, 107(4):1272–1295, 2007.

[147] Boon Kar Yap, Ruidong Xia, Mariano Campoy-Quiles, Paul N. Stavrinou, and Donal D. C. Bradley. Simultaneous optimization of charge-carrier mobility and optical gain in semiconducting polymer films. *Nature Materials*, 7(5):376–380, may 2008.

[148] A. Sezai Sarac. Polymerization Techniques. In *Nanofibers of Conjugated Polymers*, pages 111–130. may 2016.

[149] William MITCHELL, Mansoor D'LAVARI, Changsheng WANG, and David SPARROWE. CONJUGATED POLYMERS, may 2015.

[150] Takafumi Uemura, Yuri Hirose, Mayumi Uno, Kazuo Takimiya, and Jun Takeya. Very high mobility in solution-processed organic thin-film transistors of highly ordered [1]benzothieno[32-b]benzothiophene derivatives. *Applied Physics Express*, 2(11):111501, nov 2009.

[151] Akichika Kumatani, Chuan Liu, Yun Li, Peter Darmawan, Kazuo Takimiya, Takeo Minari, and Kazuhito Tsukagoshi. Solution-processed, Self-organized Organic Single Crystal Arrays with Controlled Crystal Orientation. *Scientific Reports*, 2(1):393, dec 2012.

[152] Zhichao Zhang, Boyu Peng, Xudong Ji, Ke Pei, and Paddy Kwok Leung Chan. Marangoni-Effect-Assisted Bar-Coating Method for High-Quality Organic Crystals with Compressive and Tensile Strains. *Advanced Functional Materials*, 27(37):1703443, oct 2017.

[153] Mujeeb Ullah, Robert Wawrzinek, Ravi C.R. Nagiri, Shih Chun Lo, and Ebinazar B. Namdas. UV–Deep Blue–Visible Light-Emitting Organic Field Effect Transistors with High Charge Carrier Mobilities. *Advanced Optical Materials*, 5(8):1600973, apr 2017.

Chapter 9

Appendix

Content Reuse Permission Permission to reproduce publish content are listed in this appendix.

JOHN WILEY AND SONS LICENSE TERMS AND CONDITIONS

Sep 25, 2019

This Agreement between Imperial College London -- Julianna Panidi ("You") and John Wiley and Sons ("John Wiley and Sons") consists of your license details and the terms and conditions provided by John Wiley and Sons and Copyright Clearance Center.

License Number	4617051181347
License date	Jun 27, 2019
Licensed Content Publisher	John Wiley and Sons
Licensed Content Publication	Advanced Functional Materials
Licensed Content Title	Introducing a Nonvolatile N-Type Dopant Drastically Improves Electron Transport in Polymer and Small-Molecule Organic Transistors
Licensed Content Author	Julianna Panidi, Jaspreet Kainth, Alexandra F. Paterson, et al
Licensed Content Date	Jun 18, 2019
Licensed Content Volume	0
Licensed Content Issue	0
Licensed Content Pages	10
Type of use	Dissertation/Thesis
Requestor type	Author of this Wiley article
Format	Print and electronic
Portion	Full article
Will you be translating?	No
Title of your thesis / dissertation	High mobility soluble organic semiconductors for microelectronic applications
Expected completion date	Sep 2019
Expected size (number of pages)	170
Requestor Location	Imperial College London Blackett Laboratory Prince Consort Road London, London SW7 2AZ United Kingdom Attn: Imperial College London
Publisher Tax ID	EU826007151

JOHN WILEY AND SONS LICENSE
TERMS AND CONDITIONS
Nov 30, 2019

This Agreement between Imperial College London -- Julianna Panidi ("You") and John Wiley and Sons ("John Wiley and Sons") consists of your license details and the terms and conditions provided by John Wiley and Sons and Copyright Clearance Center.

License Number	4718800817769
License date	Nov 30, 2019
Licensed Content Publisher	John Wiley and Sons
Licensed Content Publication	Advanced Electronic Materials
Licensed Content Title	Polymer Light-Emitting Transistors With Charge-Carrier Mobilities Exceeding 1 cm2 V−1 s−1
Licensed Content Author	Mujeeb Ullah Chaudhry, Julianna Panidi, Sungho Nam, et al
Licensed Content Date	Nov 25, 2019
Licensed Content Volume	0
Licensed Content Issue	0
Licensed Content Pages	9
Type of use	Dissertation/Thesis
Requestor type	Author of this Wiley article
Format	Print and electronic
Portion	Full article
Will you be translating?	No
Title of your thesis / dissertation	High mobility soluble organic semiconductors for microelectronic applications
Expected completion date	Sep 2019
Expected size (number of pages)	170
Requestor Location	Imperial College London Blackett Laboratory Prince Consort Road London, London SW7 2AZ United Kingdom Attn: Imperial College London
Publisher Tax ID	EU826007151
Total	0.00 GBP